Physical Limits to Cellular Sensing of the Environment

by

Michael Vennettilli

B.S., Ursinus College, 2016

Submitted to the Graduate Faculty of

the Dietrich School of Arts and Sciences in partial fulfillment

of the requirements for the degree of

Doctor of Philosophy

University of Pittsburgh

2021

UNIVERSITY OF PITTSBURGH

DIETRICH SCHOOL OF ARTS AND SCIENCES

This dissertation was presented

by

Michael Vennettilli

It was defended on

July 21, 2021

and approved by

Rob D. Coalson, Professor, Departmental of Chemistry

Hanna Salman, Associate Professor, Department of Physics and Astronomy

Xiao-lun Wu, Professor, Department of Physics and Astronomy

Jianhua Xing, Associate Professor, Department of Computational and Systems Biology

Dissertation Director: Andrew Mugler, Assistant Professor, Department of Physics and Astronomy

Physical Limits to Cellular Sensing of the Environment

Michael Vennettilli, PhD

University of Pittsburgh, 2021

Cells must accurately sense various aspects of their environment for survival. In 1977, Berg and Purcell initiated a line of work placing physical limits on cell sensing [6]. The work herein is a continuation of this tradition. In our first project, we studied the effect of critical biochemical feedback on cell sensing. Using a concrete model, we weighed the trade-offs between high susceptibility, long-range correlations and critical slowing down. We found that the critical system could have high steady state mutual information between a ligand and an internal readout molecule if the ligand dynamics are sufficiently slower than the intracellular dynamics. However, the information rate is always minimized at the critical point due to critical slowing down. Our second and third projects involved deriving lower bounds on signal-to-noise ratios for environmental variables, much like the initial work of Berg and Purcell. The novelty is that the sensed quantities are fluid flow direction and temperature. These extend the range of their work, as these are non-chemical cues, however, they are sensed using molecules. Our work on flow sensing was motivated by studies on metastatic cancer cells that showed they could detect the direction of fluid flow. They do so by secreting molecules that are pushed by the flow and return to the surface anisotropically. We compared two different strategies for signal transduction: endocytosis and reversible binding. We found that reversible binding admits a lower relative error than endocytosis. The endocytosis model has an optimal absorption rate. We use experimental data to argue that the endocytosis rate is far from the optimum, supporting the possibility that receptor binding transduces the information. In our third project, we started by computing the relative error in temperature sensing arising from its own fluctuations. We found that it was too low to be limiting. Temperature sensing is indirect, it is transduced from molecular conformations, changing reaction rates, or various mechanical properties. Turning to a biochemical model based on the canonical protein thermometer TlpA, we found that the error arising from the biochemical reactions dominated the system. We discuss the connection to existing

experimental data.

Table of Contents

List of Figures

Preface

I would like to thank everyone who helped me pursue and work towards my PhD. I will begin by thanking my advisor, Dr. Andrew Mugler. He gave me the space to make mistakes, especially early on, and this was invaluable for my growth and education. He showed me how to think critically about our work and the importance of writing a compelling story. He was highly accessible, and I took full advantage of that. Meeting with him always shed light on difficulties that arose in research. He is a shining example and role model for a group leader.

I would like to thank my prinicpal collaborator, Dr. Amir Erez. He proposed the project that became the bulk of my work during my PhD. He gave many insightful comments when we were stuck and drafting and revising manuscripts.

I am grateful for the numerous educators who inspired to go down this path. Dr. Tom Carroll, Gary Christ, Dr. Chris Sadowski, and Dr. Nicholas Scoville deserve particular mention. I spent many hours in their offices asking questions. I wouldn't be where I am today without their support and encouragement.

I am thankful for my fellow group members, both past and present: Dr. Julien Varennes, Dr. Tommy Byrd, Dr. Sean Fancher, Nicholas Hilgert, Dr. Ushasi Roy, Dr. Xiaoling Zhai, Dr. Shivam Gupta, Soutick Saha, Ryan LeFebre, Motasem Elgamel, and Louis Gonzalez. The group meetings had a great, collaborative atmosphere. I benefited from your feedback and advice.

I am truly appreciative of the friends that I've made during my time in graduate school. I will fondly remember our countless game nights, both in person and virtual, and our weekly tea sessions, they broke up the solitude of work and COVID. They also helped me come out of my shell. I am grateful for your constant support, it helped me through the challenges and stresses that graduate school poses. I am also thankful for our thoughtful (or not) conversations and constant criticism of my bad coding practices. To Jesus Rueda-Becerril, Samantha Clark, Honggu Choi, Sneha Das, Zach Davis, Terrence Edmonds, Giuseppe Giuliani, Dawith Lim, Soutick Saha, and Forrest Simmons, my time in graduate school was brightened by

having you in it.

I am thankful for the love and support I received from my family. To my parents, Alberto and Toni, I wouldn't be where I am if you hadn't encouraged my interest in science and learning in general. You taught me the importance of hard work in achieving your goals. Telling me that you were proud of me lifted some of the self-doubt that I felt. To my brothers, Gianfranco and Alessandro, I am grateful for our humorous and cathartic discussions. You gave thoughtful perspectives, and I enjoyed our discussions.

I. Introduction

One of the hallmarks of life is the ability to sense and respond to various aspects of one's surroundings. Cells are able to do so remarkably, despite only having access to limited kinds of stimuli. There is a long tradition initiated by the work of Berg and Purcell of studying the limits that physics imposes on cellular sensing [6]. To give a flavor for this kind of work, we begin this dissertation by presenting their argument to deduce the scaling of a cell's error in concentration sensing. We consider the cell as a perfectly absorbing sphere with radius a, so that any molecule that reaches its surface is absorbed. The cell is sensing some ligand with diffusion coefficient D and is immersed in a background concentration c_0. By dimensional analysis, we can deduce that the mean flux to the surface is $\sim Dac_0$. We assume that cell absorbs the molecules for some time T, and uses the information about the number of molecules to infer the concentration. It is possible to show that the number of molecules that reach the surface in a given time is a Poisson random variable, so its variance is the mean. Using linear error propagation, we find that the error in concentration sensing is

$$\frac{\sigma(c)}{c_0} = \frac{\sigma(n)}{c_0}\frac{1}{d\overline{n}/dc_0} = \frac{\sigma(n)}{\overline{n}} \sim \frac{1}{\sqrt{Dac_0T}}. \tag{1}$$

Berg and Purcell showed that a similar scaling holds for a more realistic picture with receptor binding and unbinding, this work was subsequently extended for the case where binding is not diffusion limited [9, 58]. This example shows how the limited information that the cell has can be used to infer something about its surroundings.

In this dissertation, we will build on this tradition by exploring three main extensions of it. In the first topic, we look at the effect of intracellular feedback on concentration sensing. Signals are often transduced from receptors and result in gene expression, which is subject to feedback. Positive feedback can induce bifurcations, or changes in stability of the long-term behavior, in the gene's output. These bifurcations behave very similarly to thermodynamic critical points, where phase transitions, such as spontaneous thermal magnetization, occur. Critical points exhibit a number of interesting features: they are highly sensitive, have strong

spatial correlations, and exhibit critical slowing down. Some have speculated that it is beneficial for biological systems to operate near criticality [77, 85]. However, each of the benefits has apparent drawbacks. High sensitivity is beneficial when the input is controlled, but random noise can lead to large excursions from the expected response. Long-range correlations allow changes to propagate across the system, but this reduces the number of independent units in the system and the ability to respond to changes with a fine spatial resolution. Critical slowing down allows the system to respond to the time-averaged inputs or stimuli, which should reduce the effects of noise, but this requires the system to have very long response times. These trade-offs don't have a straightforward resolution and therefore require systematic, quantitative investigation. We explore the implications of criticality for biochemical sensing in a simple model with intracellular feedback and intercellular communication.

To this end, we will appeal to some basic ideas in information theory. This framework grew out of Claude Shannon's work to place limits on reliably sending messages in the presence of noise [103]. The key notion that we will use is that of mutual information, which is the average reduction in uncertainty, specifically entropy, of the input after measuring the output [103, 20]. Mutual information may also be viewed as a non-linear measure of correlations. For example, let x and y be the coordinates of points uniformly distributed on the boundary of the unit circle. It is straightforward to show that x and y do not covary. However, measuring x reduces the possible values of y to at most two values. Though the linear correlation $\langle xy\rangle - \langle x\rangle\langle y\rangle$ vanishes, the mutual information does not, so mutual information captures more subtle dependencies. In fact, the mutual information is zero if and only if the input and the output are independent.

In the second topic, we investigate flow sensing in metastasis. Metastasis, the process in which cancer cells leave the primary tumor to inhabit a new site, is the deadliest stage in cancer progression. Cancer cells use a variety of mechanisms to navigate, including the alignment of collagen fibers in the extracellular matrix, pressure or shear forces, and various chemical gradients, such as oxygen or growth factors. Experiments have shown that cancer cells can detect the direction of fluid flow by secreting diffusible molecules that they detect with receptors on their surface [105]. This is particularly relevant for cancer cells navigating towards lymphatic vessels and using the network to access distant parts of the body. The

flow in the experiments was slow, and the cells secreted molecules at a low rate. This raises the question of limits to sensing flow through this mechanism. In this project, we used a combination of stochastic processes and fluid dynamics to derive limits for this kind of sensing and compare with the experiments.

In the third project, we study the limits to cellular temperature sensing. Cells must mount a rapid response to address heat or cold shock [71]. Temperature can be a cue for some cells to initiate virulence [33]. Other cells can thermotax, or move toward a preferred temperature range [69]. Early work on the subject argued that the temperature fluctuations within a cell were too negligible to be limiting [24]. If extrinsic temperature fluctuations do not limit cell behavior, what does? We address this question for protein thermometers. In response to temperature changes, proteins change conformation, and these proteins need to initiate some change in activity, usually via gene expression. The conformation change and gene expression are stochastic processes, and we hypothesize that this noise could dwarf the noise in the temperature itself. Using a model based on the protein thermometer TlpA [56], we find that this is the case: the error is dominated by fluctuations in the measurement apparatus instead of the quantity of interest. Again we compare our findings with experimental data.

II. Multicellular Sensing at a Feedback-Induced Critical Point

This work builds off of previously published work done by our group:

- *Amir Erez, Tommy A. Byrd, Robert M. Vogel, Gregoire Altan-Bonnet, and Andrew Mugler. Universality of biochemical feedback and its application to immune cells. Physical Review E, 99(2):022422, 2019*

- *Tommy A. Byrd, Amir Erez, Robert M. Vogel, Curtis Peterson,* ***Michael Vennettilli****, Gregoire Altan-Bonnet, and Andrew Mugler. Critical slowing down in biochemical networks with feedback. Physical Review E, 100(2):022415, 2019*

- *Amir Erez, Tommy A. Byrd,* ***Michael Vennettilli****, and Andrew Mugler. Cell-to-Cell Information at a Feedback-Induced Bifurcation Point. Physical Review Letters, 125(4):048103, 2020.*

It has been published in Physical Review E:

- ***Michael Vennettilli****, Amir Erez, and Andrew Mugler. Multicellular sensing at a feedback-induced critical point. Physical Review E, 102(5):052411, 2020.*

Feedback in sensory biochemical networks can give rise to bifurcations in cells' behavioral response. These bifurcations share many properties with thermodynamic critical points. Evidence suggests that biological systems may operate near these critical points, but the functional benefit of doing so remains poorly understood. Here we investigate a simple biochemical model with nonlinear feedback and multicellular communication to determine if criticality provides a functional benefit in terms of the ability to gain information about a stochastic chemical signal. We find that when signal fluctuations are slow, the mutual information between the signal and the intracellular readout is maximized at criticality, because the benefit of high signal susceptibility outweighs the detriment of high readout noise. When cells communicate, criticality gives rise to long-range correlations in readout

molecule number among cells. Consequently, we find that communication increases the mutual information between a given cell's readout and the spatial average of the signal across the population. Finally, we find that both with and without communication, the sensory benefits of criticality compete with critical slowing down, such that the information rate, as opposed to the information itself, is minimized at the critical point. Our results reveal the costs and benefits of feedback-induced criticality for multicellular sensing.

A. Introduction

Cells need to reliably sense their environment to survive and coordinate behavior. Many studies have investigated the precision of sensory tasks, such as detecting concentrations of a single molecular species [6, 58, 87], concentrations of multiple molecular species [16, 76], and concentration gradients [26, 53]. Much of those works focused on linear networks in single cells. Yet, it is well known that biological systems use nonlinear feedback to process signals, and there is evidence that communication among multiple cells improves sensory precision [48, 25, 34]. For example, in the developing embryo of the *Drosophila melanogaster* fruit fly, cell nuclei sense their position along a Bicoid (Bcd) protein gradient using Hunchback (Hb) as a genetic readout. Hb has binding sites on its own promoter region leading to positive feedback [113], and it is also thought to be diffusively communicated from nucleus to nucleus in the embryo [48, 29]. In *Vibrio fischeri* bacteria, cells sense the concentration of an autoinducer (AI). The uptake of AI is thought to cooperatively produce more AI via the lux operon, creating a nonlinear positive feedback loop, and AI is communicated diffusively among cells for the purpose of quorum sensing [119]. Here we probe theoretically this interplay between cellular sensing, feedback, and communication.

Positive feedback generically leads to bifurcations in dynamical behavior [111]. This raises the question of what the implications of being near a bifurcation are for biological sensing. In the presence of noise, which is ubiquitous in biochemical networks, these systems behave like thermodynamic critical systems in the large system size limit, exhibiting characteristic features like power law scalings and critical slowing down [31, 15]. In realistic

systems with a finite number of cells and molecules, there are finite-size effects where the divergent quantities, such as susceptibility and correlation length, round off to a finite value within some distance of the critical point and exhibit the expected scaling outside of this distance. Though these quantities don't diverge, they can still have sharp peaks near criticality. Indeed, there is experimental evidence suggesting that some biological systems operate near criticality [77, 63, 85]. On the one hand, critical systems have divergent susceptibilities and correlation lengths, which may be beneficial for sensing. On the other hand, critical systems have large fluctuations and slow dynamics, which may be detrimental for sensing. These expected tradeoffs suggest that the costs and benefits of sensing at criticality need to be explored in a systematic way.

Here we probe the implications of criticality for the sensing of a noisy, spatially uniform chemical concentration by a population of communicating cells. Specifically, we use the rate constants that create a critical point in the infinite system to study finite systems. We focus on a variant of Schlögl's second model [99] that incorporates linear sensing, nonlinear feedback, and communication between neighboring cells. We consider cells on a one-dimensional lattice, but we show that the model is in the mean-field Ising static universality class, and therefore we expect our steady-state results to qualitatively hold for more general geometries. In the case of a single cell, we find that critical feedback maximizes the mutual information when the ligand dynamics are slow due to the high susceptibility of the response to the input. Similarly, with multiple cells, we find that critical feedback couples with cell-cell communication to produce long-range correlations, which maximizes information about the average ligand concentration across the population. However, we find that in both cases, critical feedback results in critical slowing down, such that the information rate is minimized. We discuss the implications of these tradeoffs for several well-studied biological systems.

B. Results

1. The Model and Its Universality Class

We consider a one-dimensional chain of sites with periodic boundary conditions, where each site corresponds to a cell and its immediate environment (Fig. 1). We assume the chemical components within each site are well mixed. Our model generalizes Schlögl's second model for nonlinear biochemical feedback [99] to multiple coupled cells and introduces an extracellular diffusing ligand to be sensed. The number of ligand molecules at site i is denoted by ℓ_i, while the number of readout molecules in cell i is denoted x_i. Specifically, we have the reactions

$$\begin{aligned} &\mathrm{L}_i \underset{\mathrm{k}_\ell^+}{\overset{\mathrm{k}_\ell^-}{\rightleftharpoons}} \varnothing, \quad \mathrm{L}_i \underset{\gamma'}{\overset{\gamma'}{\rightleftharpoons}} \mathrm{L}_{i\pm1}, \quad \mathrm{L}_i \xrightarrow{\mathrm{k}_1^+} \mathrm{X}_i + \mathrm{L}_i, \\ &\mathrm{X}_i \xrightarrow{\mathrm{k}_1^-} \varnothing, \quad 2\,\mathrm{X}_i \underset{\mathrm{k}_2^-}{\overset{\mathrm{k}_2^+}{\rightleftharpoons}} 3\,\mathrm{X}_i, \quad \mathrm{X}_i \underset{\gamma}{\overset{\gamma}{\rightleftharpoons}} \mathrm{X}_{i\pm1}. \end{aligned} \tag{2}$$

The first two reversible reactions describe the ligand diffusively entering or leaving the vicinity of the ith cell or diffusing to that of the neighboring cell. The second pair of reversible reactions describes some process that is maintaining a background concentration of the ligand. These reactions should be viewed as other things going on in the surroundings that produce and consume these molecules. Alternatively, they can be viewed as molecules diffusing into and out of a region where they can interact with each cell. The third reaction describes the production of a readout molecule in response to the ligand. The fourth reaction describes linear degradation of the readout. The fifth reaction subjects the readout to positive and negative nonlinear feedback. The sixth reaction describes exchanging the readout between neighboring cells. The fourth and fifth reactions are often written with additional, mediating bath species, but these are usually assumed to have a fixed concentration, and therefore here we have absorbed them into the rate constants. As long as the initial conditions are positive, these reactions ensure that the molecule numbers are non-negative and finite. When the ligand or readout is low at a site, degradation at the site or diffusion from the site cannot occur, so there must be a production event at the site or diffusion into the site. When the molecule numbers are large, degradation, specifically the $\mathrm{L}_i \longrightarrow \varnothing$ and $3\,\mathrm{X}_i \longrightarrow 2\,\mathrm{X}_i$ reactions, dominate and reduce the molecule numbers.

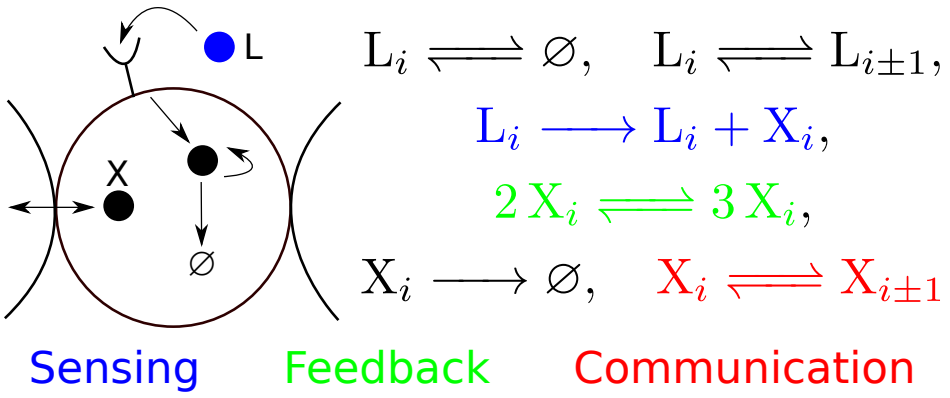

Figure 1: Illustration of the model. Each site on a 1D lattice is a well-mixed cell and its immediate environment. A ligand binds to a receptor and produces a readout molecule that is subject to nonlinear feedback and may be exchanged between cells. The ligand is spatially uniform and has its own fluctuating dynamics.

The nonlinear feedback in Eq. 2 has its own mechanistic interpretation [99], but it also emerges as the Taylor series for a wide range of nonlinear reactions near a pitchfork bifurcation [31, 15]. This was one of the reasons that we chose this model. We are not considering all possible reactions below a given order. For example, this is the case if the feedback reactions were replaced with production via a Hill function in x with Hill coefficient $H > 1$. Eq. 2 is also convenient mathematically, as it can be mapped onto the mean-field Ising model with a translation and multiplicative scaling, as we now show.

In previous work, we mapped the single cell onto the mean-field Ising model by solving for the steady state probability distribution of readout molecule number [31]. This approach breaks down with multiple coupled cells because the steady state distribution is not known analytically. Instead, we extract the mapping from the deterministic dynamics [11]. The rate equations take the form

$$\begin{aligned} \frac{dx_i}{dt} &= k_1^+ \ell_i - k_1^- x_i + k_2^+ x_i^2 - k_2^- x_i^3 + \gamma \nabla^2 x_i, \\ \frac{d\ell_i}{dt} &= k_\ell^+ - k_\ell^- \ell_i + \gamma' \nabla^2 \ell_i \end{aligned} \tag{3}$$

where ∇^2 is the discrete Laplace operator. The key is to perform a change of variables so that this equation of motion is in the normal form of a supercritical pitchfork bifurcation, as the relaxation dynamics to the minima of the Landau free energy of the Ising model are in this form [111, 45]. This is accomplished by finding where the second derivative of the right-hand side with respect to x_i vanishes, and this occurs at $x_c = k_2^+/3k_2^-$. Moreover, x_c controls the typical molecule number in the system, with scaling properties similar to finite-size scaling with the length of the lattice in Ising models. Interpreting x_c as the system size is further justified by the fact that the deterministic approximation is only valid in the large x_c limit and, as a consequence of this, the bifurcation and expected critical scalings, with rounding off, only appear in this same limit. Making the substitution $x_i = x_c(m_i + 1)$, where m_i is an order parameter analogous to the magnetization per unit volume of the Ising model, and rescaling time so that the cubic term has a coefficient of $-1/3$ gives

$$\frac{dm_i}{d\tau} = -\frac{1}{3}m_i^3 - \left[3\frac{k_1^- k_2^-}{(k_2^+)^2} - 1\right] m_i + \left[\frac{2}{3} - 3\frac{k_1^- k_2^-}{(k_2^+)^2} + 9\frac{k_1^+ \ell_i (k_2^-)^2}{(k_2^+)^3}\right] + 3\frac{k_2^- \gamma}{(k_2^+)^2}\nabla^2 m_i. \tag{4}$$

Eq. 4 describes relaxation dynamics to the minima of the Landau free energy for the Ising model, provided that we identify

$$\tau = \frac{(k_2^+)^3 t}{9(k_2^-)^2}, \tag{5}$$

$$\theta = 3\frac{k_1^- k_2^-}{(k_2^+)^2} - 1, \tag{6}$$

$$h_i = \frac{2}{3} - 3\frac{k_1^- k_2^-}{(k_2^+)^2} + 9\frac{k_1^+ \ell_i (k_2^-)^2}{(k_2^+)^3} \tag{7}$$

as the reduced temperature and dimensionless field respectively. The bifurcation occurs when both of these parameters are set to zero [111]. The field h_i biases the distribution to either high or low molecule numbers. This can be understood by the quantitative analogy between the magnetization m_i and the molecule number x_i. For a positive magnetic field, the magnetization will be biased towards positive values, so the molecule number will be biased towards values larger than x_c, and a similar analogy holds for negative fields. Because we are interested in properties of the system near the critical point, we set $h_i = 0$ (using the mean value of the ligand $\overline{\ell} = k_\ell^+/k_\ell^-$ for ℓ_i). When the reduced temperature θ is decreased, the feedback becomes increasingly strong, and the distribution goes from unimodal to bimodal

when it goes from positive to negative [1]. Eq. 4 differs from the standard form of φ^4 theory [45], where the coefficient of the Laplacian term would be 1. Instead this coefficient depends on the exchange rate γ of molecules from cell to cell, which is an independently tunable parameter in the biochemical model. These parameters come from the deterministic dynamics, so they only capture the large x_c limit of the stochastic dynamics. We ignore corrections from small molecule numbers [30] and purely stochastic effects [121].

The fact that this system is in the static universality class of the mean field Ising model may appear at odds with previous work done on Schlögl's second model extended to a spatial context [12, 46, 47]. The reason is that in these previous works, there is a finite occupancy per site and each molecule can only react with neighboring molecules. In our case, each molecule can interact with an arbitrary number of molecules within a single well-mixed site. This makes the mean field nature of the model apparent, and one should think of our model as a system of linearly coupled mean field systems.

2. Defining the Sensory Measure

A typical measure of sensory precision is the signal-to-noise (SNR) ratio in the cell's estimate of the ligand concentration. In Fig. 2A we show the SNR $\overline{x}^2/\sigma_x^2$ for a single cell as a function of θ, computed using Gillespie simulations [44] of Eq. 2. The parameter θ inversely sets the feedback strength, with $\theta \to \infty$ corresponding to no feedback and $\theta = 0$ corresponding to critical feedback. We avoid the $\theta < 0$ case (feedback-induced bifurcation) since the mean and variance of a bimodal distribution are ill-suited measures in this context. We see that the SNR increases with θ, meaning that criticality is worse for the SNR than having no feedback. The reason is that, for $\theta \geq 0$, the mean $\overline{x}$ is independent of θ while the variance σ_x^2 increases as θ decreases and the critical point is approached. Evidently criticality is not beneficial for sensing a mean concentration with low error.

In contrast, we hypothesize that criticality might be beneficial for sensing fluctuations around a mean concentration. This is because critical systems have large susceptibility to

[1] We are considering varying the parameters mathematically to understand the performance of a certain region in the parameter space for a biological system. This is not some dynamical process being applied to the cells. However, it is possible that cells could adjust θ or h through mutation and selection, so they can approach the optima in parameter space.

a biasing field. Indeed, the fluctuating ligand number ℓ_i appears in the effective field h_i (Eq. 7). Therefore, we hypothesize that the critical system may have maximal correlations between the ligand and readout, and therefore serve as an optimal fluctuation detector. To investigate this hypothsis, we consider the mutual information and information rate [103] between the ligand and readout molecule numbers as our sensory measures from here on. The mutual information and information rate inherently capture correlations between two fluctuating variables (see Appendix A.A for a summary of results for Gaussian variables, which we will draw upon below).

3. Single Cell

We start by analyzing the Langevin equations obtained from the Kramers-Moyal expansion for our system in the limit of a single cell. Even for the single cell, the nonlinearity is an obstruction to exact analytic solutions, and therefore we linearize the equation about a deterministic steady state. When θ is negative, the distribution is bimodal; this feature cannot be captured by the linearized equation, so this approximation is only valid for $\theta > 0$. We will use this approach to gain insight and then use simulations for more accurate results. When $\theta > 0$ and $h = 0$, there is only one deterministic fixed point; it occurs at $\overline{x} = x_c$ and is stable. This is another reason for treating x_c as a tuning parameter that sets the system size.

a. Mutual Information

Letting $b(x, \ell) = k_1^+ \ell + k_2^+ x^2$ and $d(x) = k_1^- x + k_2^- x^3$ denote the total birth and death terms for x (Eq. 2), we obtain the linearized system

$$\begin{aligned} \dot{\delta\ell} &= -k_\ell^- \delta\ell + \sqrt{2k_\ell^+}\epsilon, \\ \dot{\delta x} &= -c\delta x + k_1^+ \delta\ell + \sqrt{2d(x_c)}\eta, \end{aligned} \tag{8}$$

where ϵ and η are independent, delta-correlated Gaussian white noise processes that describe the noise in production and degradation (Appendix A.B). The $c = \partial_x[d(x) - b(x, \ell)]_{x_c, \bar{\ell}}$ term arises from linearizing the birth and death propensities with respect to x. This system is

a two-dimensional Ornstein-Uhlenbeck process and may be solved analytically using matrix exponentials and Itô's lemma. This is done in Appendix B and we find that the steady-state mutual information between x and ℓ is

$$I = \frac{1}{2}\log\left(1 + \frac{(k_1^+)^2\bar{\ell}c}{d(x_c)(k_\ell^- + c)^2 + (k_1^+)^2 k_\ell^- \bar{\ell}}\right). \tag{9}$$

We expect the system to track ligand fluctuations best when the ligand dynamics are slow ($k_\ell^-/k_1^- \ll 1$). Writing Eq. 9 in this limit and in terms of the reduced temperature (Eq. 6), we find

$$I = \frac{1}{2}\log\left(1 + \frac{x_c}{\bar{\ell}}\frac{(3\theta+1)^2}{3\theta(3\theta+4)}\right). \tag{10}$$

This result has a finite limit when $\theta \to \infty$ (no feedback) and diverges as $\theta \to 0$ (critical feedback) [2]. This suggests that indeed, the mutual information between ligand and readout is maximized at criticality under these assumptions. Moreover, the role of x_c as the system size is apparent, with the mutual information increasing approximately as $\log(x_c/\bar{l})$.

To understand intuitively why the information is maximized at criticality, we can write Eq. 10 in terms of new variables: the susceptibility $\chi = (\partial m/\partial h)_{h=0}$ and the variance σ_x^2 with ℓ fixed to its mean value. The susceptibility is obtained directly from Eq. 4, which for the single cell in terms of θ and h reads $0 = -m^3/3 - \theta m + h$ at steady state. Differentiating with respect to h and evaluating at $h = 0$ yields $0 = -(m^2)_{h=0}\chi - \theta\chi + 1$, or $\chi = 1/\theta$, where we have recognized that $m = 0$ for $h = 0$ and $\theta > 0$. The variance is $\sigma_x^2 = d(x_c)/c$ (Appendix A.B), or in terms of the reduced temperature, $\sigma_x^2 = x_c(\theta + 4/3)/\theta$. In terms of these variables, Eq. 10 reads

$$I = \frac{1}{2}\log\left(1 + \frac{(\chi/3+1)^2}{\bar{\ell}\sigma_x^2/x_c^2}\right). \tag{11}$$

We see from the expressions for χ and θ that both the susceptibility and noise diverge at the critical point like $1/\theta$. However, we see from Eq. 11 that the information scales monotonically with the square of the susceptibility in the numerator, but only the first

[2]For finite probability spaces, mutual information and entropy are finite. On countably infinite spaces, they diverge if the tails of the distribution are sufficiently heavy. This explains why the mutual information diverges under the linear noise approximation as $\theta \to 0$. This approximation always predicts a Gaussian distribution. As θ decreases through zero, the distribution goes from unimodal to bimodal. At $\theta = 0$, the distribution has a vanishing second derivative at the peak. This only holds for a Gaussian as the variance tends to infinity, this makes the tails of the distribution very heavy.

power of the variance in the denominator. This implies that the benefit of high susceptibility outweighs the detriment of high noise, making criticality optimal for this type of information transmission.

The linear noise approximation breaks down at the critical point, and therefore we use Gillespie simulations [44] to check our results. The simulations also allow us to probe the bimodal regime ($\theta < 0$). The results are shown in Fig. 2B. In the slow ligand limit, $k_\ell^-/k_1^- \ll 1$, shown in the red curve, we see that the divergence at the critical point is rounded off to a global maximum just above the critical point due to the finite size of the system.

The location of the global maximum changes discontinuously as the timescale ratio k_ℓ^-/k_1^- is increased. As soon as k_ℓ^-/k_1^- becomes nonzero, the mutual information vanishes at the critical point in the linear noise approximation (Appendix A.B, Eq. 58), as seen for the yellow curve in Fig. 2B. In the simulations, as k_ℓ^-/k_1^- is increased, the "blip" on the red curve for $\theta < 0$ separates and forms another peak, with a minimum appearing between the two local maxima [3]. The height of the peak decreases until it dips below the asymptotic value at large θ and later disappears entirely, as seen for the purple curve in Fig. 2B. Thus, when the ligand timescales are sufficiently fast, the mutual information is maximized in the absence of feedback. It is possible to estimate where criticality ceases to be highly informative using the linear noise approximation (Appendix A.B, Eq. 58). Under this approximation, the system with feedback cannot outperform the system without feedback if $k_\ell^-/k_1^- \geq (3\sqrt{3}-5)/8 \approx 0.025$. This suggests that a timescale separation of nearly two orders of magnitude is necessary to benefit from feedback.

We can also probe the effect of changing the system sizes $\overline{\ell}$ and x_c. Although we could use simulations, the results depend on a choice of k_ℓ^-/k_1^-, and the peak may not exist if this ratio is too large. We study the $k_\ell^-/k_1^- \to 0$ limit numerically by writing the joint distribution as $P(x|\ell)P(\ell)$, where $P(\ell)$ is a Poisson distribution with mean $\overline{\ell}$ and $P(x|\ell)$ is computed from the master equation assuming that ℓ is constant. We find that, even when the timescale separation is infinitely large, the peak at the critical point can vanish if either of the molecule numbers are sufficiently small. In this case, the mutual information increases

[3] At the present, we do not understand why the blip appears at all. This would require future work.

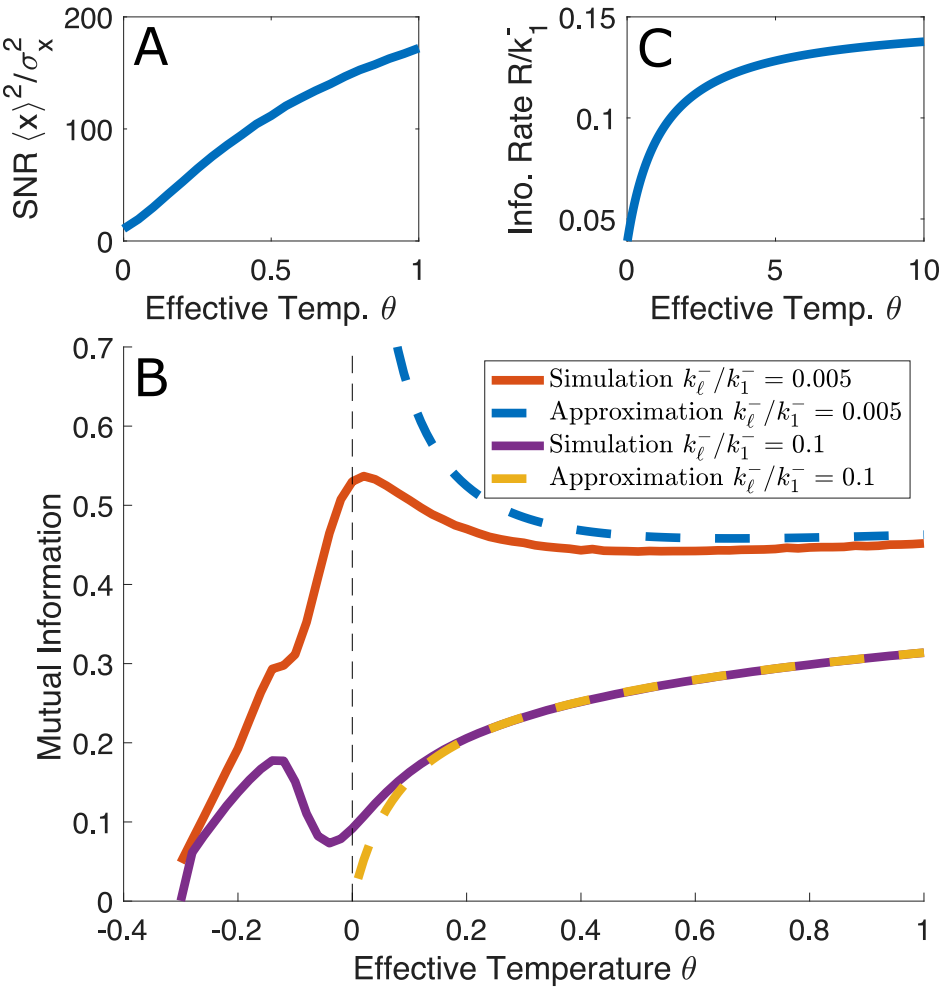

Figure 2: Sensory information for a single cell. (A) Signal-to-noise ratio for the readout in the slow ligand regime with $k_\ell^-/k_1^- = 5 \times 10^{-3}$. (B) Mutual information between ligand and readout. Blue (yellow): Linear noise approximation Eq. 10 (Eq. 58) with $k_\ell^-/k_1^- = 0$ (0.1). Red (purple): Gillespie simulations with $k_\ell^-/k_1^- = 5 \times 10^{-3}$ (0.1). (C) Information rate between ligand and readout using linear noise approximation with $k_\ell^-/k_1^- = 5 \times 10^{-3}$. All curves have $h = 0$, $x_c = 10^3$, and $\bar{\ell} = 500$.

monotonically with θ.

b. Information Rate

Cells respond to their environment and make life-or-death decisions in real time, and do not have the luxury to wait until all possible information has been collected, leading some to argue that the information rate is more relevant than the information itself [112, 72]. The information rate, R, is the asymptotic rate of change of the mutual information between trajectories of the input and output [83]. Concretely, we sample the input and output at discrete times, usually multiples of some $\delta t > 0$, and construct vectors of the samples $\vec{i}_N = \{i(0), i(\delta t), ..., i((N-1)\delta t)\}$ and $\vec{o}_N = \{o(0), o(\delta t), ..., o((N-1)\delta t)\}$. We regard $\vec{i}_N$ and $\vec{o}_N$ as random variables and compute the mutual information between them. Finally, the information rate is computed as

$$R(i,o) = \lim_{\delta t \to 0^+} \left(\lim_{N \to \infty} \frac{I(\vec{i}_N, \vec{o}_N)}{N \delta t} \right). \tag{12}$$

It is possible to compute the information rate between the ligand and readout fluctuations under the linear noise approximation for our system. In Appendix A.C, we show that the result is

$$R = \frac{\pi k_\ell^-}{2} \left(\sqrt{1 + \frac{x_c}{3\bar{\ell}} \frac{k_1^-}{k_\ell^-} \left[\frac{(1+3\theta)^2}{4 + 7\theta + 3\theta^2} \right]} - 1 \right). \tag{13}$$

Eq. 13 vanishes when the ligand degradation rate vanishes. This makes sense as the ligand degradation rate sets the timescale for the ligand dynamics, and the ligand is the signal that the readout is trying to track. Eq. 13 is a monotonically increasing function of the temperature for $\theta \geq 0$ (Fig. 2C). This suggests that the information rate has a global minimum at criticality and is maximized without feedback, at least for $\theta \geq 0$. This reveals an interesting tradeoff: the steady-state mutual information decreases as ligand rates increase and is maximized at criticality when the ligand rates are slow, while the information rate is maximized when the ligand rates are fast and is minimized at criticality. Discretely sampled trajectories are high-dimensional in this problem, which is an obstruction to efficient and accurate simulation via the Gillespie algorithm [72]. Although the instantaneous distribution for the ligand and readout is two-dimensional, the joint distribution for sampling dynamic

trajectories at N points is $2N$-dimensional. However, we still expect the information rate to decrease as θ decreases towards zero, as positive feedback is known to increase response time [2] and critical slowing down will make this more extreme.

4. Multiple Cells with Communication

a. Long-range Correlations

In previous work [31], we established that the single cell had the same static critical exponents as the mean field Ising model. In this section, we will show that the multicellular system inherits the mean field exponent for the the correlation length, $\nu = 1/2$, at least for $\theta > 0$, and therefore exhibits long-range correlations among cells. To find the critical exponent, we compute the spatial correlation function between different cells' readouts using Gillespie simulations [44]. Here, we use the trapezoidal rule to integrate the correlations along both sides of the multicellular ring, clockwise and counterclockwise to the furthest cell on the opposite side of the ring, and then average the two results. The resulting correlation length ξ is plotted as a function of θ in Fig. 3A. When θ is very close to the critical point, finite size x_c effects become important and lead to rounding off. However, we can see the true scaling by moving away from the critical point so that the finite size effects become less limiting. Here we see that $\xi \sim \theta^{-1/2}$, or $\nu = 1/2$, as in the mean field Ising model [45].

Next, we looked at the effect of communication strength γ on the correlation length. We expect that the correlation length, measured in units of the lattice spacing, at $\theta = 0$ should roughly approach the system size $N/2$ in the strong communication limit $\gamma \to \infty$, where N is the number of cells, and the factor of 2 is due to the periodic boundary condition. The result is shown in Fig. 3B for $N = 20$ cells, and we see that the correlation length indeed approaches $N/2$ as γ becomes large.

b. Sensory Information

To compute the sensory information for the multicellular system, we proceed with the Langevin equations as we did with the single cell. The key difference here is that there

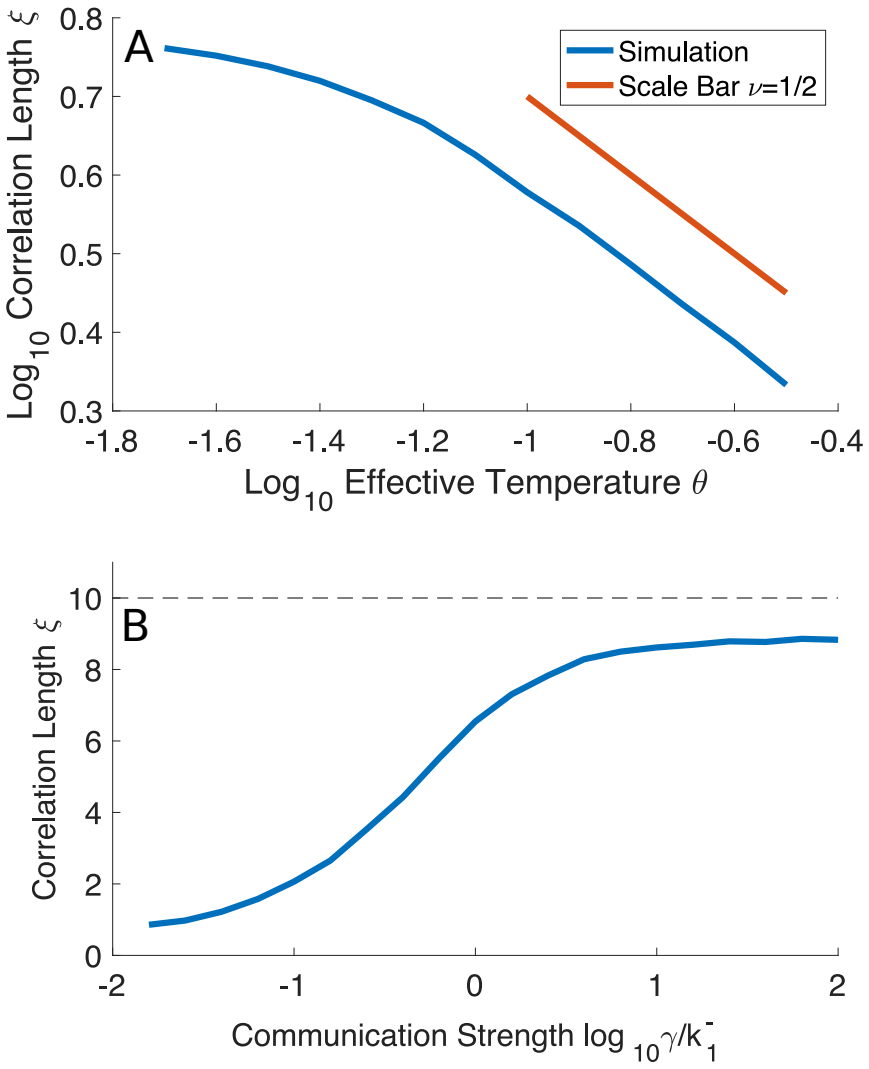

Figure 3: Long-range correlations in the multicellular system. (A) Correlation length ξ, measured in units of the lattice spacing, numerically integrated from simulations using the trapezoidal rule, scales with reduced temperature θ with mean-field exponent $\nu = 1/2$. Rolloff at $\theta = 0$ is due to finite size effects. Here $k_\ell^-/k_1^- = \gamma'/k_1^- = 5 \times 10^{-3}$, $\gamma/k_1^- = 1$, $h_i = 0$, $\overline{\ell} = 150$, $x_c = 300$, and $N = 20$ cells. (B) Critical correlation length increases with communication strength γ, approaching system size $N/2$. Parameters as in A with $\theta = 0$.

are discrete Laplacian terms and noise terms for diffusion left or right for each site. The linearized Langevin equations become

$$\begin{aligned}
\dot{\delta\ell}_i =& -k_\ell^- \delta\ell_i + \gamma'\nabla^2\delta\ell_i + \sqrt{2k_\ell^+}\epsilon_{i,C} \\
&+ \sqrt{\gamma'\bar{\ell}}(\epsilon_{i-1,R} + \epsilon_{i+1,L} - \epsilon_{i,L} - \epsilon_{i,R}), \\
\dot{\delta x}_i =& -c\delta x_i + k_1^+\delta\ell_i + \gamma\nabla^2\delta x_i + \sqrt{2d(x_c)}\eta_{i,C} \\
&+ \sqrt{\gamma x_c}(\eta_{i-1,R} + \eta_{i+1,L} - \eta_{i,L} - \eta_{i,R}),
\end{aligned} \tag{14}$$

where the η's and ϵ's are independent Gaussian white noise processes (Appendix A.D). The terms with subscript L and R describe the noise in hopping to the left and right respectively, while the C terms describe the changes due to the chemical processes. The linearized system is still a multi-dimensional Ornstein-Uhlenbeck process. One can obtain closed form results for the matrix exponentials and covariance matrix by using translational invariance. These calculations are done in Appendix A.D.

With multiple cells, there are several possible measures of sensory information to consider. Because we aim to focus on the actions that an individual cell can take, we take the output to be the readout in a single cell, δx_i. However, there are multiple possibilities for the sensory input: the local ligand fluctuations $\delta\ell_i$, the ligand fluctuations at all cell locations $\vec{\delta\ell}$, or the spatial average of the ligand fluctuations

$$\delta L = \frac{1}{N}\sum_{i=1}^{N}\delta\ell_i. \tag{15}$$

We compute the mutual information between each of these inputs and the output in Appendix A.E. In the slow ligand limit, we find that all of them diverge at criticality as in the single-cell case, and therefore we focus on the effect of tuning the communication rate γ.

We find that the first mutual information $I(\delta x_i, \delta\ell_i)$ decreases as the communication between cells is increased (Appendix A.E.1). This makes intuitive sense because $I(\delta x_i, \delta\ell_i)$ is the information between local ligand fluctuations and local readout. Communication among cells only mixes one cell's readout with the other cells' readouts. The other cells' readouts report on distant ligand fluctuations, which are uncorrelated with the local ligand fluctuations because the ligand molecules at different sites are independent Poisson random variables. Therefore $I(\delta x_i, \delta\ell_i)$ is maximized in the absence of cell-cell communication.

We also find that the second mutual information $I(\delta x_i, \vec{\delta\ell})$ decreases as communication between cells is increased (Appendix A.E.2). For this sensory task, the cell must be able to reliably encode the entire spatial profile $\vec{\delta\ell}$ into a single, fluctuating variable δx_i. On the one hand, we expect cell-cell communication to help in this task because communication transmits information about distant ligand fluctuations sensed by the other cells. On the other hand, as in the previous case, communication obscures the information that the cell directly obtains about its local environment $\delta\ell_i$, which is one of the components of $\vec{\delta\ell}$. Evidently the latter effect dominates. The mutual information is maximized in the absence of communication, where it can sense its immediate environment reliably.

We find that the third mutual information $I(\delta x_i, \delta L)$ increases as the communication between cells is increased (Appendix A.E.3). Like the spatial profile $\vec{\delta\ell}$, the spatial average of the ligand fluctuations δL also contains global information. However, unlike in the previous case, for this sensory measure it is not detrimental that the single cell's readout combines local and global environmental information. This is because here the cell only senses average environmental changes. An increase in its readout is correlated with an increase in the ligand somewhere, and for this task it does not matter where. It is worth pointing out that a cell is most strongly correlated with its immediate neighborhood. As N increases, its neighborhood contributes less strongly to the average, and the mutual information monotonically decreases.

To verify the linear noise approximation, we again use Gillespie simulations to probe the exact behavior of $I(\delta x_i, \delta L)$. The mutual information in the slow ligand regime is shown in Fig. 4. Like in the single cell case, it is largest near the critical point when the communication strength is fixed. For $\theta \geq 0$, the mutual information increases with the communication rate, as expected from the linear noise approximation.

Finally, we again consider the information rate. Because the mutual information involving the spatial average was the only one to benefit from communication, we focus on this case. We compute the cross-spectrum under the linear noise approximation analytically (see Appendix A.F) and integrate over frequency numerically to find the information rate. The result is shown in Fig. 5. We see that the information rate is maximized when communication is strong and feedback is weak. Thus, as with the steady-state information, cell-cell communication improves the rate of information acquisition for this type of measure. How-

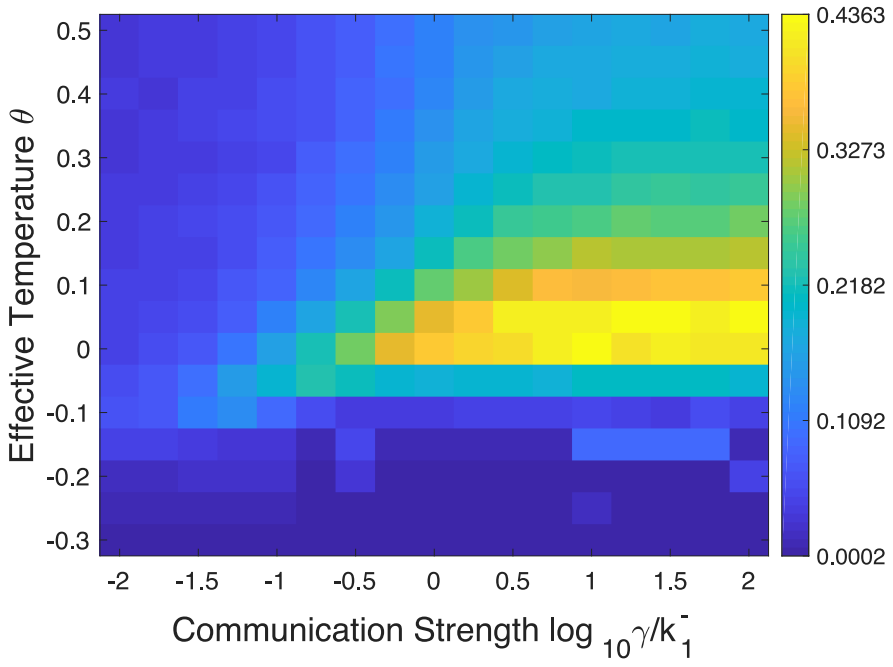

Figure 4: Mutual information between a single cell's readout and the spatial average of the ligand fluctuations. This was obtained from Gillespie simulations with $N = 10$, $h_i = 0$, $x_c = 300$, $\overline{\ell} = 150$, and $k_\ell^-/k_1^- = \gamma'/k_\ell^- = 5 \times 10^{-3}$. This is maximized near criticality as the communication strength increases.

ever, like in the single-cell case, critical slowing down makes the rate suboptimal at criticality, such that the case without feedback has the highest rate. We also find that the rate increases with the ratio of sizes $x_c/\overline{\ell}$, decreases with the number of sites N and the ratio of timescales k_ℓ^-/k_1^-, and increases weakly with the ligand hopping rate γ'. Additionally, there can be a local maximum as $\gamma/k_1^- \to 0$ if k_ℓ^-/k_1^- is large, but this isn't a global maximum, as the large γ/k_1^- behavior can exceed this value.

C. Discussion

We have investigated a minimal biochemical model with communication and intracellular feedback, in order to elucidate the tradeoffs of criticality for multicellular sensing. Criticality arises due to a bifurcation in the biochemical dynamics that places the model in the static universality class of the mean-field Ising model. We have found that the susceptibility and noise both peak at the critical point. If the ligand fluctuations are sufficiently slow, the former effect dominates, and the mutual information is maximized. Otherwise, the information is maximized far from the critical point, where there is no feedback. The introduction of cell-cell communication leads to long-range correlations. We have found that this feature leads to an increase in the information that a single cell gains about the average environment across the population, but not about the local or spatially resolved environment. Finally, we have found that although critical feedback can maximize steady-state information, it minimizes the information rate due to critical slowing down.

How do our results compare to related theoretical work? Previous work has investigated the effect of receptor cooperativity on sensing an average ligand concentration using an Ising-like model [107]. There it was assumed that the ligand binding and unbinding dynamics are fast, and it was found that the signal-to-noise ratio is maximized when the receptors were independent. This result is consistent with our finding that the mutual information is maximized without feedback when the ligand is fast ($k_\ell^- \gtrsim k_1^-$). Other work has investigated the propagation of information in a two-dimensional spin system where one spin evolves via the telegraph process and the others have Glauber dynamics [72]. There it was also found

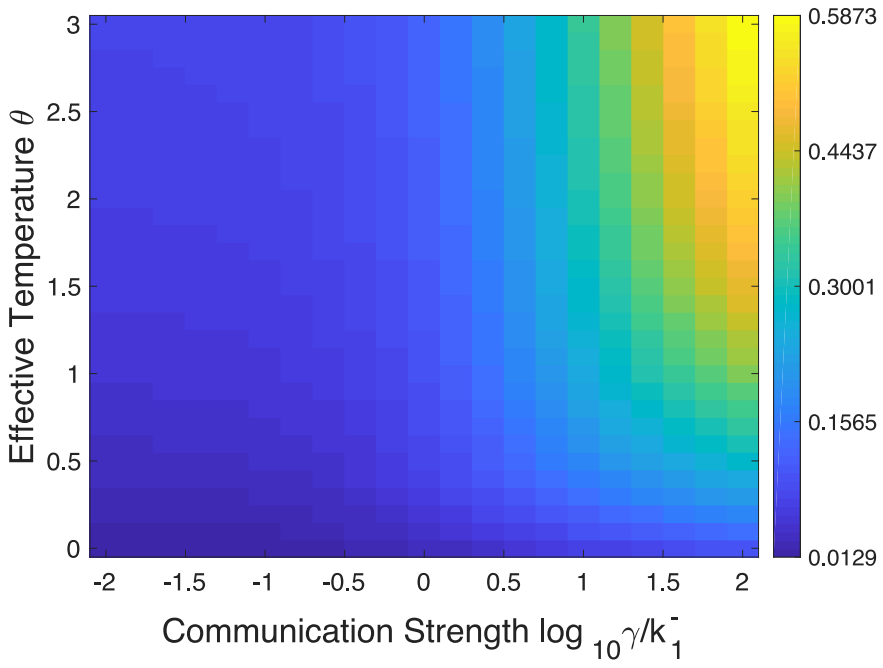

Figure 5: Information rate between a single cell's readout and the spatial average of the ligand fluctuations. This was obtained from the cross-spectrum under the linear noise approximation and numerically integrating. This plot has $N = 10$, $h_i = 0$, $x_c = 300$, $\bar{\ell} = 150$, and $k_\ell^-/k_1^- = \gamma'/k_1^- = 1$. The rate is maximized if we increase the effective temperature and communication strength.

that the mutual information is maximized only when the driving is slow, consistent with our results. It was further found that the information rate is maximized at a finite driving timescale and a finite, supercritical temperature, whereas here we find that the information rate is maximized for an infinitely fast ligand timescale and infinite effective temperature (no feedback). It will be interesting to investigate if this apparent difference stems from the different structure or dimensionality of the two systems.

What are the implications of our results for particular biological systems? Our findings suggest that in systems with communication and feedback, such as the Bicoid-Hunchback system in fruit flies or quorum sensing in bacteria, sensory information is maximized at the critical point so long as input fluctuations are slow and sufficient time is available to combat critical slowing down. In the case of the Bicoid-Hunchback system in particular, previous experimental work has indeed suggested that criticality helps cells respond to small changes in the morphogen profile [63], whereas other work has argued that cells are instead in the bistable regime [67]. The auditory system is also a well-known sensory system that appears to benefit from being near criticality [54]. There is also a form of cell-cell communication, as cells with different characteristic frequencies are coupled to enhance their response to general auditory signals [110]. These features are consistent with our findings, although it is important to note that frequency detection is a different task than the task of detecting fluctuations in a noisy, uniform ligand signal as we consider here.

Is criticality via intracellular feedback beneficial to cellular sensing overall? In light of our findings, it may be that this type of criticality is more detrimental for sensing a uniform concentration than it is beneficial, for several reasons. The type of information that criticality benefits concerns fluctuations about the mean, not the mean concentration itself, and the biological relevance of this task is unclear. Furthermore, we have found that high mutual information is only observed at sufficiently large molecule numbers and when there is a timescale separation of at least two orders of magnitude between the cell and its environment. Finally, the information rate, which better accounts for the fact that we are looking at a dynamical process, is minimized at criticality.

The approach that we have used is very general and can be applied to other systems that admit a Langevin description. There are many other biochemical models whose expansions

near the bifurcation reduce to our model, and different normal forms can describe other classes of models. This fact can be exploited to probe more specific biochemical mechanisms and more general sensory measures. Nonetheless, our model is minimal and neglects features such as extrinsic noise, bursting, and cell-to-cell variability that are known to play an important role in biochemical signaling [41, 82, 102, 52, 19]. In the future it will be important to expand our model to include these more general features.

III. Precision of Flow Sensing by Self-Communicating Cells

This was a collaborative project. I participated in the calculation for the model with endocytosis/ absorption with other group members. I took more of a leadership role examining the effect of non-spherical geometry on our limits to cell sensing. I have omitted or reduced parts of the project where I did not contribute. This work has been published in Physical Review Letters:

- *Sean Fancher,* ***Michael Vennettilli****, Nicholas Hilgert, and Andrew Mugler. Precision of Flow Sensing by Self-Communicating Cells. Physical Review Letters, 124(16):168101, 2020.*

Metastatic cancer cells detect the direction of lymphatic flow by self-communication: they secrete and detect a chemical which, due to the flow, returns to the cell surface anisotropically. The secretion rate is low, meaning detection noise may play an important role, but the sensory precision of this mechanism has not been explored. Here we derive the precision of flow sensing for two ubiquitous detection methods: absorption vs. reversible binding to surface receptors. We find that binding is more precise due to the fact that absorption distorts the signal that the cell aims to detect. Comparing to experiments, our results suggest that the cancer cells operate remarkably close to the physical detection limit. Our prediction that cells should bind the chemical reversibly, not absorb it, is supported by endocytosis data for this ligand-receptor pair.

A. Introduction

Metastasis is the process of cancer cells spreading from the primary tumor to other parts of the body. A major route for spreading is the lymphatic system, a network of vessels that carry fluid to the heart. Particular cancer cells detect the drainage of lymphatic fluid toward the vessels and move in that direction [86]. Experiments have shown that the

detection occurs by self-communication: the cells secrete diffusible molecules (CCL19 and CCL21) that they detect with receptors (CCR7) on their surface [105]. The flow affects the distribution of detected molecules thereby provides information about the flow direction. This flow detection mechanism, termed 'autologous chemotaxis,' has been observed for breast cancer [105], melanoma [105], and glioma cell lines [84], as well as endothelial cells [49], and has been studied using fluid dynamics models [105, 37, 117].

The flow is slow. Lymphatic drainage speeds near tumors are typically $v_0 = 0.1{-}1$ μm/s [18, 21], and the speed decreases further with proximity to the cell surface due to the laminar nature of low-Reynolds-number flow. In contrast, a secreted molecule diffuses with coefficient $D = 130{-}160$ $\mu\text{m}^2/\text{s}$ [37], covering a distance equivalent to the cell radius ($a \approx 10$ μm [105]) in a typical time of a^2/D and giving a "velocity" of $D/a = 13{-}16$ μm/s. The ratio of these velocities $\epsilon \equiv v_0 a/D = 0.006{-}0.08$, called the Péclet number, is small, indicating that diffusion dominates over flow in this process.

Also, the secretion rate is low. Cells secrete $0.7{-}2.3 \times 10^{-15}$ g of CCL19/21 ligand in a 24-hour period (Fig. 3F in [105]), which given the molecular weights of these ligands (11 and 14.6 kDa, respectively [51]), corresponds to a secretion rate of $\nu = 1200{-}5200$ molecules per hour. Yet, cells begin migrating in a matter of hours [105].

The slow flow and low secretion rate raise the question of whether autologous chemotaxis is a physically plausible mechanism for these cells. Is a couple thousand molecules, biased by such a weak flow field, enough for the cells to determine the flow direction? If so, with what precision? Although this mechanism has been modeled at the continuum level, the question of sensory precision has remained unexplored.

At the same time, the question of sensory precision has been heavily explored for other cellular processes, beginning with the early work of Berg and Purcell [6], and extending to more modern works on concentration sensing [9, 118, 28, 5, 58, 64, 10, 34], gradient sensing [26, 27, 53, 81, 114], and related sensory tasks [79, 106, 76, 78]. Yet, the mechanism of autologous chemotaxis has thus far evaded this list, despite its importance to cancer biology and its potential for interesting physics.

Here we combine stochastic techniques from sensory biophysics with perturbation techniques from fluid dynamics to derive the fundamental limit to the precision of flow sensing by

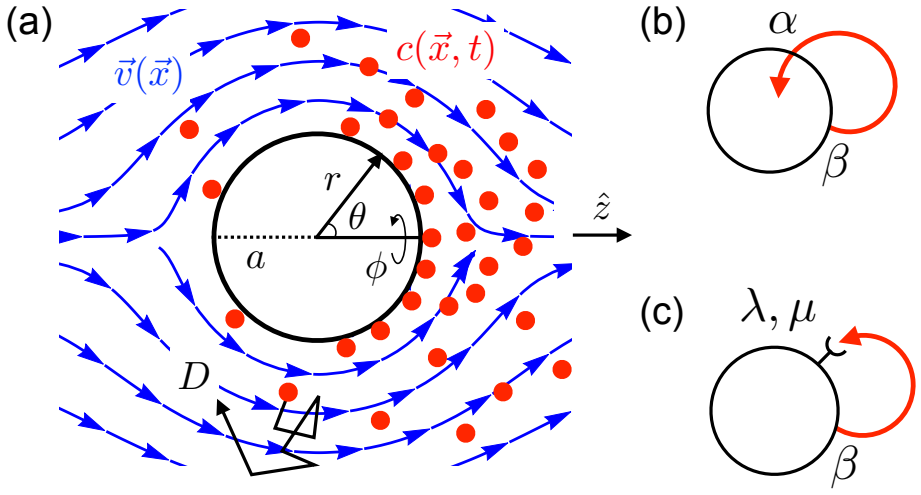

Figure 6: Flow sensing by self-communication. (a) A cell isotropically secretes molecules (red) that diffuse and drift along laminar flow lines (blue). The cell detects the molecules by (b) absorption or (c) reversible binding to receptors.

self-communication. We consider two ubiquitous methods of molecule detection: absorption vs. reversible binding to receptors (Fig. 6). For both, we find a Berg-Purcell-like expression that is ultimately limited by the Péclet number, the secretion rate, and the integration time. Comparing to the experiments, this expression places a stringent limit on the level of precision that is possible for these cells, suggesting that they detect the flow direction near-optimally given the physical constraints. Finally, we predict that reversible binding is more precise than absorption due to the fact that absorption necessarily reduces the anisotropy in the detected signal, a prediction that we test with endocytosis data on the CCL19/21-CCR7 ligand-receptor pair.

B. Results

Consider a spherical cell with radius a that secretes molecules isotropically with rate $\beta \equiv \nu/4\pi a^2$ per unit area, in the presence of a fluid flowing with velocity v_0 (Fig. 6). At low Reynolds number and high environmental permeability, laminar flow lines obeying Stokes' equation [6] form around the cell [Fig. 6(a), blue]. However, in the tumor environment and in experiments, the permeability $\mathcal{K}$ is low ($\kappa \equiv \sqrt{\mathcal{K}}/a \sim 10^{-3}$ [105]), and the flow lines obey the more general Brinkman's equation [13]. For a sphere at steady state they are given by [3]

$$\begin{aligned}\vec{v}(r,\theta,\phi) = v_0 \cos\theta \left[1 - \frac{\zeta}{\rho^3} + \frac{3\kappa}{\rho^2}\left(1+\frac{\kappa}{\rho}\right) e^{-(\rho-1)/\kappa}\right] \hat{r} \\ - v_0 \sin\theta \left[1 + \frac{\zeta}{2\rho^3} - \frac{3}{2\rho}\left(1+\frac{\kappa}{\rho}+\frac{\kappa^2}{\rho^2}\right) e^{-(\rho-1)/\kappa}\right] \hat{\theta}. \end{aligned} \tag{16}$$

Here, $\rho \equiv r/a$ and $\zeta \equiv 1 + 3\kappa + 3\kappa^2$, the flow is in the $\hat{z}$ direction ($\theta = 0$), $\hat{r}$ and $\hat{\theta}$ are the radial and polar unit vectors, and $\vec{v}$ is independent of ϕ by symmetry. In the limit $\kappa \to \infty$, Eq. 16 reduces to Stokes flow; we are interested in the opposite limit. Note that $\vec{v} = 0$ at the cell surface $r = a$.

1. Endocytosis/ Absorption Model

The molecules diffuse with coefficient D and drift along the flow lines [Fig. 6(a), red]. This process creates a stochastically evolving concentration field $c(r,\theta,\phi,t)$ with a mean distribution $\overline{c}(r,\theta,\phi,t)$, where the bar represents the ensemble average over many independent realizations of the system. The mean follows the diffusion-drift equation, which at steady state reads

$$0 = \frac{\partial \overline{c}}{\partial t} = D\nabla^2 \overline{c} - \vec{v} \cdot \vec{\nabla} \overline{c}. \tag{17}$$

We consider two cases for molecule detection at the cell surface: absorption [Fig. 6(b)] or reversible receptor binding [Fig. 6(c)]. In the former, there exists a flux boundary condition at the cell surface,

$$-D \left.\frac{\partial \overline{c}(r,\theta)}{\partial r}\right|_a = \beta - \alpha \overline{c}(a,\theta), \tag{18}$$

where α is the absorption rate per unit area, and $\overline{c}(r,\theta)$ is independent of ϕ and t by symmetry and the system being in steady state, respectively. We also require that the concentration vanish at infinity.

We define the dimensionless concentration $\chi \equiv \overline{c}a^3$ and velocity $\vec{u} \equiv \vec{v}/v_0$. In terms of the dimensionless radial distance ρ and the Péclet number ϵ, Eq. 17 at steady state becomes $0 = \nabla_\rho^2\chi - \epsilon\vec{u}\cdot\vec{\nabla}_\rho\chi$. Because ϵ is small, we use a perturbative solution $\chi = \chi_0 + \epsilon\chi_1$. However, in problems with diffusion and background flow, a single perturbative expansion cannot simultaneously satisfy the boundary conditions at $r = a$ (Eq. 18) and $r \to \infty$ ($\overline{c} \to 0$) due to the particular spatial nonuniformity of $\vec{u}$ [1]. In particular, we found that using a single perturbative expansion and enforcing the boundary condition at $r = a$ gave a non-zero concentration as $r \to \infty$, and this can be negative, depending on θ. The resolution is to split the solution into an inner part $\chi(\rho,\theta)$ that satisfies the boundary condition at the cell surface and holds when ρ is order one, and an outer part $X(s,\theta)$ that satisfies the boundary condition at infinity and holds when $s = \epsilon\rho$ is order one. We match χ and X by requiring them to be equal at each order in ϵ as $\rho \to \infty$ and $s \to 0$, respectively.

To zeroth order, the inner solution satisfies Laplace's equation, $0 = \nabla_\rho^2\chi_0$, the general solution to which consists of spherical harmonics and powers of ρ (Appendix B.A.1). For the outer solution, we write Eq. 17 in terms of s and X, which reads $0 = \nabla_s^2 X - \vec{u}\cdot\vec{\nabla}_s X$. One can define a perturbative expansion for X, but we show (Appendices B.A and B.A.2) that only the leading terms of X and $\vec{u}$ matter. The latter is $\vec{u} = \hat{z}$, corresponding to the uniform flow far from the cell where X applies. The solution to this equation satisfying $X \to 0$ as $s \to \infty$ consists of modified Bessel functions and spherical harmonics.

We find that the matching condition requires all but one term in χ_0 and X to vanish (Appendix B.A.3), yielding

$$\chi_0 = \frac{\gamma}{\rho}, \qquad X = \frac{\epsilon\gamma}{s}e^{-s(1-\cos\theta)/2}, \tag{19}$$

where $\gamma \equiv \tilde{\beta}/(1+\tilde{\alpha})$, and $\tilde{\beta} \equiv \beta a^4/D$ and $\tilde{\alpha} \equiv \alpha a/D$ are dimensionless secretion and absorption rates, respectively. We see that to leading order, the concentration falls off with distance, and far from the cell it is largest in the flow direction ($\theta = 0$).

To obtain the anisotropy near the cell, which is essential for the flow sensing problem, we must go to the next order. χ_1 satisfies $0 = \nabla_\rho^2 \chi_1 - \vec{u} \cdot \vec{\nabla}_\rho \chi_0$, which is the Poisson equation with $\vec{u}$ (Eq. 16) and χ_0 (Eq. 19) providing the source term. This equation can be solved using a Green's function, with coefficients determined by Eq. 18 and matching to X in Eq. 19 (Appendix B.B). The result is

$$\chi_1 = \frac{\gamma}{2} \left\{ \frac{\tilde{\alpha}}{(1+\tilde{\alpha})\rho} - 1 + \frac{\cos\theta}{4} \left[\frac{(1-\tilde{\alpha})w}{(2+\tilde{\alpha})\rho^2} + f(\rho,\kappa) \right] \right\}, \tag{20}$$

where $w \equiv 1 + \kappa^{-1} - \kappa^{-2} e^{1/\kappa} E_1(\kappa^{-1})$ is a monotonic function that limits to 2 ($\kappa \ll 1$) and 1 ($\kappa \gg 1$), $f(\rho,\kappa)$ is an α-independent function (Appendix B.B.2), and $E_1(x) \equiv \int_1^\infty dt\, e^{-tx}/t$. We see that χ_1 acquires a $\cos\theta$ anisotropy largest in the flow direction ($\theta = 0$). We have checked by numerical solution of Eq. 17 that for $\epsilon \leq 0.1$, Eq. 20 is accurate to within 0.4% at the cell surface (see the supplement for the publication [35]).

Information about the anisotropy, and thus the flow direction, comes from the front-back asymmetry in the absorptive flux of molecules αc at the cell surface over a time T, which is captured by weighing each absorption event by its location represented as $\cos\theta$. Normalizing this by the mean number of absorbed molecules, we define the anisotropy measure [26, 114]

$$A \equiv \frac{\int_0^T dt \int a^2 d\Omega\ \alpha c(a,\theta,\phi,t) \cos\theta}{T \int a^2 d\Omega'\ \alpha \bar{c}(a,\theta')}, \tag{21}$$

where $d\Omega = d\phi\ d\theta \sin\theta$, and the cosine extracts the asymmetry between the front ($\theta = 0$) and back ($\theta = \pi$). Using the solution for χ in Eqs. 19 and 20 and the fact that $f(1,\kappa) = w$, the mean evaluates to

$$\overline{A} = \frac{w\epsilon}{8(2+\tilde{\alpha})} \tag{22}$$

to leading order in ϵ (Appendix B.C).

Eq. 22 gives the mean anisotropy but ignores the counting noise due to diffusive molecule arrival. The equivalent expression to Eq. 21 that accounts for discrete molecule arrival is [26] $A = \overline{N}^{-1} \sum_{i=1}^N \cos\theta_i$, where θ_i is the arrival angle of the ith molecule, and $N = \int_0^T dt \int a^2 d\Omega\ \alpha c(a,\theta,\phi,t)$ is the total number of molecules absorbed in time T. The mean of this expression is given by Eq. 22 (Supplement B.C). The variance is calculated by recognizing that molecule arrivals are statistically independent and that N is Poissonian [26]

(which we have checked even with flow using particle-based simulations, see the supplement of the paper [35]). The result is

$$\sigma_A^2 = \frac{1}{\overline{N}} = \frac{1}{\nu T}\left(\frac{1+\tilde{\alpha}}{\tilde{\alpha}}\right) \tag{23}$$

to leading order in ϵ (Supplement B.D). This expression includes (as does Eq. 27 below) a factor of 3 that arises from each directionally independent component of the variance. We see that the variance in the anisotropy scales inversely with the mean number of absorbed molecules.

Combining Eqs. 22 and 23, we obtain a relative error of

$$\frac{\sigma_A^2}{\overline{A}^2} = \frac{64(1+\tilde{\alpha})(2+\tilde{\alpha})^2}{w^2\epsilon^2\nu T\tilde{\alpha}} \gtrsim \frac{282}{\epsilon^2\nu T}. \tag{24}$$

In the second step, we have set w to its maximal value of 2 for $\kappa \ll 1$ (as in the experiments [105]) and recognized that the expression has a minimum at $\tilde{\alpha}^* = (\sqrt{17}-1)/4 \approx 0.78$. The minimum arises from the following tradeoff: strong absorption maximizes the number of detected molecules and therefore reduces noise (Eq. 23); but it also causes molecules to be absorbed immediately after release, preventing them from interacting with the nonzero flow away from the cell surface and therefore reducing the mean (Eq. 22). Eq. 24 sets the fundamental limit to the precision of flow sensing by molecule absorption, dependent only on the Péclet number ϵ and the total number of secreted molecules νT.

2. Summary of Findings for the Reversible Binding Model

We summarize our findings for the case of reversible receptor binding [Fig. 6(c)]. In this model, we track the concentration and the surface density of bound receptors $b(\theta,\phi)$ on the cell's surface. This creates a source and a sink term in the diffusion equation at the surface. For the steady state mean, the inward and outward fluxes due to binding and unbinding cancel, and the steady state diffusion equation and boundary conditions are exactly that of the endocytosis/ binding model with $\alpha = 0$, see Eqs. 17 and 18. In the reversible binding

case, the anisotropy is defined as the average of the cosine over the angular distribution of bound receptors and the integration time T,

$$A \equiv \frac{\int_0^T dt \int a^2 d\Omega \; b(\theta, \phi, t) \cos\theta}{T \int a^2 d\Omega' \; \bar{b}(\theta')}. \tag{25}$$

Because $\bar{b}(\theta)$ is proportional to $\bar{c}(\theta)$, the means of Eqs. 21 and 25 take equivalent forms. Therefore, to leading order in ϵ, the mean of Eq. 25 is simply Eq. 22 with $\alpha = 0$,

$$\overline{A} = \frac{w\epsilon}{16}. \tag{26}$$

For details on the dynamics of b, see the paper [35].

Because binding is reversible, there are correlations between the bound receptor concentrations at different regions of the cell surface. Therefore, we cannot use the Poisson counting technique to calculate the noise as in Appendix B.D. Instead, we include Langevin noise terms in the dynamics to account for these correlations. These terms have zero mean, are uncorrelated with each other, for details, see [43, 35]. To find the variance, we Fourier transform the dynamics in space and time, calculate the power spectrum of A, and recognize that σ_A^2 is given by its low-frequency limit [9, 81, 34, 114]. The result is

$$\sigma_A^2 = \frac{1}{\nu T}\left(\frac{7}{9} + \frac{2}{\tilde{\lambda}}\right) \tag{27}$$

to leading order in ϵ. The rate λ describes the formation of bound receptors and $\tilde{\lambda} \equiv \lambda a/D$ is its non-dimensionalized form [35]. In the absence of any bound receptors in a region, the mean rate of forming bound receptors is $\lambda \bar{c}(a, \theta)$. Combining Eqs. 26 and 27, we obtain the relative error

$$\frac{\sigma_A^2}{\overline{A}^2} = \frac{1792}{9w^2\epsilon^2\nu T}\left(1 + \frac{18}{7\tilde{\lambda}}\right) \gtrsim \frac{50}{\epsilon^2 \nu T}. \tag{28}$$

In the second step, we take $w = 2$ and $\tilde{\lambda} \gg 1$, which is expected in the case where binding is diffusion-limited. Comparing Eqs. 24 and 28, we see that reversible binding achieves $\sqrt{282/50} \approx 2.4$ times lower error than absorption. The reason is that absorption (Eq. 22), but not binding (Eq. 26), reduces the anisotropy. Absorption is an active modifier of the signal created by secretion and flow, whereas reversible binding is a passive monitor.

3. Effect of Non-Spherical Geometry

It is known that cells elongate in the direction of flow while moving. This should change the difference in absorption or binding events between the front and the back. We explored the effect that this had in the simplified case of Stokes' flow, so that we may neglect the effect of porosity ($\mathcal{K} \to \infty$) and use existing algorithms to numerically compute the flow [88]. We solve the laminar limit of the incompressible Navier-Stokes equation

$$\eta \nabla^2 \vec{v} = \nabla p, \tag{29}$$

where η is the dynamic viscosity of the medium and p is the pressure. The velocity $\vec{v}$ vanishes on the surface of the cell and tends toward $v_0 \hat{k} = v_0 \cos\theta \hat{r} - v_0 \sin\theta \hat{\theta}$ as $r \to \infty$. We will assume that the cell is an ellipsoid with azimuthal symmetry. This allows a stream function solution

$$\vec{v} = \nabla \times \left(\frac{\psi(r,\theta)\hat{\phi}}{r \sin\theta} \right), \tag{30}$$

and separation of variables can be used to obtain a series solution for $\psi(r,\theta)$ [88]. It is straightforward to impose the boundary condition at infinity, but the boundary condition at the surface of the cell is more subtle. We truncated the series solution and uniformly sampled the velocity components at the surface of the cell. This gives a system of equations that may be solved for the coefficients in the series expansion, see [88] or Appendix B.E.2.

We solved the convection-diffusion equation for the endocytosis/ absorbing model numerically using the flow lines determined from the procedure above. We used Mathematica's "NeumannValue" function to do this, and we found that we needed the surface of the cell to occur when some coordinate was constant. This meant that we needed to express the convection-diffusion equation in a new coordinate system. The ellipsoidal coordinates that we used are related to the usual cartesian ones via

$$\begin{aligned} x &= r_e q^{-1/3} \sin\theta_e \cos\phi_e, \\ y &= r_e q^{-1/3} \sin\theta_e \sin\phi_e, \\ z &= r_e q^{2/3} \cos\theta_e, \end{aligned} \tag{31}$$

where $q > 0$ is a fixed number, surfaces of constant $r_e > 0$ are ellipsoids, and $\theta_e \in [0, \pi]$ and $\phi_e \in [0, 2\pi]$ are similar, but not the same as, the angles in spherical coordinates. For $q > 1$, the ellipsoid is elongated in the flow direction, while it is compressed for $q < 1$, shown in Fig. 7A. For a given r_e, the volume of the ellipsoid is independent of q, but the surface area of the ellipsoid changes. We account for this by changing the reaction rates by a factor $4\pi a^2/S_q$, where S_a is the area of the ellipsoid at $r_e = a$. This is a non-orthogonal coordinate system for $q \neq 1$, so casting the convection-diffusion equation into these coordinates is subtle. We used methods from differential geometry to compute the Laplace operator and convective term in these coordinates, see [40] and Appendices B.E.3.a and B.E.3.b. We numerically solved the convection diffusion equation with the boundary conditions

$$\overline{c}(r_{e,\max}) = 0, \qquad -D\partial_{r_e}\overline{c}(r_e, \theta_e)|_{r_e=a} = (\beta - \alpha\overline{c}(a, \theta_e))\,\frac{4\pi a^2}{S_a}. \tag{32}$$

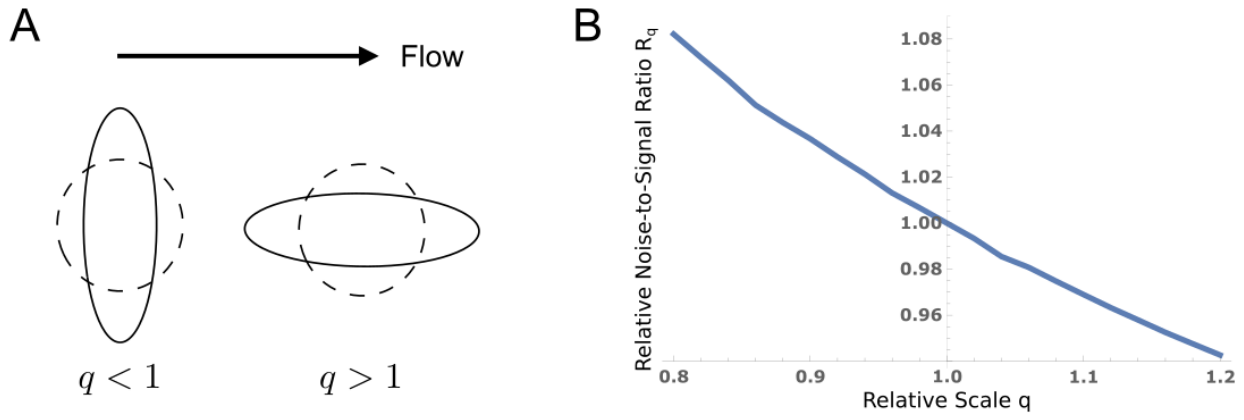

Figure 7: Elongating in the flow direction can reduce sensory error. (A) We consider an ellipsoidal cell, where q determines the elongation or compression while volume is conserved. (B) Sensory error relative to the spherical case (Eq. 233). Here $\tilde{\alpha} = 0.74$, $\tilde{\beta} = 0.04$, and $\epsilon = 0.01$.

The natural generalization of the anisotropy measure to this case is

$$A_e = \frac{1}{\overline{N}} \int_0^T dt \int dS_a \alpha_e c(a, \theta_e, \phi_e, t) \cos\theta, \qquad \overline{N} = T \int dS_a \alpha_e \overline{c}(a, \theta_e) \tag{33}$$

With the solution, we computed the mean anisotropy. The Poisson counting argument can be generalized to this case to show that $\sigma^2_{A_e} = \overline{N}$, see Appendix B.E.4. In Fig. 7B, we show a plot of the noise-to-signal ratio for A_e divided by the noise-to-signal we found numerically for $q = 1$. We see that elongating in the direction of the flow increases the precision of flow sensing. We expect similar results to hold in the cases where the porosity of the medium is reduced and the ligand reversibly binds to the cell surface.

C. Discussion

How do our results compare to the experiments on metastatic cancer cells? The inequality in Eq. 28 provides the fundamental detection limit. We plot this expression as a function of T in Fig. 8 using the maximal experimental values of $\epsilon = 0.08$ and $\nu = 5200/\text{hr}$ [105] to obtain the minimum possible error. We see that low errors are not possible in a few hours; even 10% error would take over 150 hours to achieve. Yet, the cells are observed to migrate over a 15 hour period [105]. In this time frame, it is not possible to achieve less than 30% error (Fig. 8). The situation is likely worse, given that the cells presumably begin migrating well before the 15-hour mark, and given that we have neglected any internal signaling noise. Thus, we see that the sensory performance is severely limited by the experimental parameters and the physics of the detection process. We conclude that these cells operate remarkably close to the fundamental detection limit.

We find that absorption is less precise than reversible binding (Eqs. 24 and 28). A ubiquitous mechanism of ligand absorption is endocytosis, wherein bound receptors are internalized into the cell. Therefore, we predict that the degree of CCR7 endocytosis in response to CCL19/21 binding is low. This prediction can be tested with endocytosis data on this ligand-receptor pair. Specifically, to achieve optimal absorption in Eq. 24 ($\tilde{\alpha}^* \approx 0.78$), absorption would need to occur at a rate of $4\pi a^2 \alpha^* \overline{c}(a) = \nu\tilde{\alpha}^*/(1+\tilde{\alpha}^*) \sim 25\ \text{min}^{-1}$, where we have used the isotropic approximation for $\overline{c}(a)$ (Eq. 19). However, the rate of CCR7 endocytosis in response to CCL19/21 binding is many times slower at about $1\ \text{min}^{-1}$ [14]. Thus, the degree of endocytosis is much lower than required for the absorption mechanism,

as predicted.

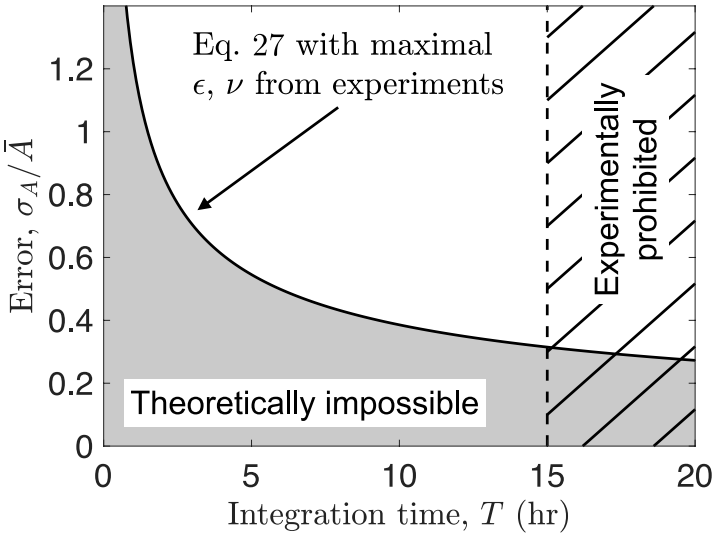

Figure 8: Fundamental limit to the precision of flow sensing. Maximum experimental values $\epsilon = 0.08$ and $\nu = 5200$/hr are used for minimum error (solid line). Cells migrate within 15 hours (dashed line). Lowest possible error is 30%.

We also find that reversible binding is most precise when the parameter $\tilde{\lambda} = Rk_a/4\pi aD$ is large (Eq. 28). Here, R is the number of receptors on the cell surface and k_a is the intrinsic association rate. Writing this parameter as $\tilde{\lambda} = (k_a/4\pi\ell D)(R\ell/a)$, where ℓ is the receptor lengthscale, we see that the first factor is the ratio that determines whether ligand-receptor binding is diffusion-limited ($k_a \gg 4\pi\ell D$) or reaction-limited ($k_a \ll 4\pi\ell D$). With the known values of R and a and a typical receptor lengthscale of $\ell \sim 10$ nm, the second factor evaluates to $10-100$. Therefore, the requirement that $\tilde{\lambda} \gg 1$ is equivalent to the statement that binding is either diffusion-limited or weakly reaction-limited. Given the high sensory performance implied by Fig. 8 and the low degree of endocytosis found above, we thus predict that CCL19/21 binding to CCR7 is either diffusion-limited or weakly reaction-limited. We are not aware of kinetics data that would test this prediction.

Our finding that reversible binding is more precise than absorption is the opposite of what was found for the detection of an externally established concentration gradient [26]. The reason is that in our problem absorption removes molecules at the source, whereas

in that problem molecules are replenished by a source at infinity. Depletion at the source prevents interactions with the flow and therefore weakens the anisotropy. Additionally, our models do not include any additional noise sources from processes internal to the cell such as protein signaling or gene expression. Because any such process would simply add a fixed amount of noise, our finding is unaffected by the inclusion of internal dynamics, and Eq. 28 remains a theoretical minimum to the error in flow sensing.

The severity of the limit in Fig. 8 raises the question of whether metastatic cancer cells benefit from additional sensory mechanisms not accounted for in our modeling. The precision of flow sensing may be affected by geometric properties of the cell such as a nonuniform distribution of receptors or aspherical morphology. We find that receptor clustering has a negligible effect on the anisotropy but that an ellipsoidal cell [88, 40] can decrease its sensory error by elongating in the direction of the flow. Further investigation of the effects of cell geometry would be an interesting topic for future work. Some chemoattractants including CCL21 are known to bind to extracellular matrix fibers and be subsequently released by proteases [89, 98, 97, 66]. This effect has been shown in continuum models of autologous chemotaxis to substantially increase the anisotropy [49, 37], although the impact on the noise is unknown. It is also important to recognize that these cells do not perform flow sensing in isolation. Indeed, studies have shown that their migration is (i) increased in the presence of another cell type (fibroblasts) [104], (ii) decreased at high cell densities [94], and (iii) reversed at even higher cell densities (although reversal is attributed to a separate pressure-sensing mechanism) [94]. The extension of our work to multiple cells remains to be explored. Finally, recent work has highlighted the benefit of on-the-fly sensing [106, 22], where an agent makes (and continually updates) its decision during the integration time, instead of afterward as assumed here. On-the-fly sensing may play an important role for these cells.

We have derived the fundamental limit to flow sensing by self-communication and shown that it strongly constrains the performance of metastatic cancer cells. Our work elucidates the physics behind a fascinating detection process and provides quantitative insights into a critical step in cancer progression.

IV. Precision of Protein Thermometry

This work has been submitted and is currently under review, but a pre-print is available:

- ***Michael Vennettilli**, Soutick Saha, Ushasi Roy, and Andrew Mugler. Precision of protein thermometry. arXiv:2012.02918v2 [physics], 2020.*

Temperature sensing is a ubiquitous cell behavior, but the fundamental limits to the precision of temperature sensing are poorly understood. Unlike in chemical concentration sensing, the precision of temperature sensing is not limited by extrinsic fluctuations in the temperature field itself. Instead, we find that precision is limited by the intrinsic copy number, turnover, and binding kinetics of temperature-sensitive proteins. Developing a model based on the canonical TlpA protein, we find that a cell can estimate temperature to within 2%. We compare this prediction with *in vivo* data on temperature sensing in bacteria.

A. Introduction

Cells routinely make decisions based on the temperature of their surroundings. For example, most cells undergo systemic changes in response to a heat or cold shock [71]. Some cells initiate a phenotypic response such as virulence when the temperature crosses a particular threshold [33]. Some cells thermotax, or move toward a preferred temperature range [69]. These behaviors are possible because molecular conformations, chemical reaction rates, and various mechanical properties of cells can change dramatically as a function of temperature, and cells have developed many different ways to detect such changes [100, 61, 70]. Molecules that participate in the response to temperature changes are called molecular thermometers or thermosensors, and this class includes DNA and various RNA and protein molecules.

Despite detailed knowledge of the molecular mechanisms of temperature sensing in cells, the basic question of what sets the precision of temperature sensing remains largely unex-

plored. Is the precision limited extrinsically by temperature fluctuations in the surrounding fluid, or intrinsically by properties of the cell's molecular components? Similar questions have been heavily investigated for other types of cell sensing, beginning with Berg and Purcell's analysis of chemical concentration sensing [6], and extending to sensing of concentration gradients [26], concentration ramps [79], multiple ligands [76], material stiffness [8], and fluid flow [35], among others. In most of these cases, extrinsic fluctuations have been found to limit sensory precision, suggesting that cells have evolved sensors that are as precise as physically possible. However, the precision of temperature sensing, and the associated question of extrinsic versus intrinsic limits, has been understudied by comparison.

Early work by Dusenbery shed important light on this problem [24]. Using the two-point correlation function for temperature fluctuations in a homogeneous fluid, Dusenbery estimated that extrinsic fluctuations are several orders of magnitude smaller than cells' actual sensitivity thresholds. This finding suggests that cells' temperature sensors are not as precise as physically possible. However, it leaves an important question unanswered: if extrinsic fluctuations do not set the limit on the precision of cellular temperature sensing, then what does?

Here we revisit this problem from a perspective that combines the physics of temperature fluctuations with the molecular mechanisms of thermoreception. Following Dusenbery's lead, we start by using the two-point correlation function to investigate a thermal analog of Berg and Purcell's "perfect instrument" for concentration sensing [6]. This investigation confirms that extrinsic temperature fluctuations are far too small to be limiting in a biological context. We therefore investigate the intrinsic fluctuations imposed by cells' molecular machinery for temperature sensing. We are guided by a prototypical and well studied protein thermometer, namely the TlpA protein in the bacterium *Salmonella typhimurium* [62, 55, 56]. Developing a stochastic model based on the experimentally characterized details of TlpA, we find that intrinsic fluctuations are much larger than extrinsic fluctuations and can in fact be biologically limiting. Specifically, we find that intrinsic fluctuations impose a sensing error of roughly 2%, and we discuss how this limit compares with the observed temperature sensing threshold in bacteria.

B. Results

1. The Perfect Instrument

In their perfect instrument for concentration sensing, Berg and Purcell considered a completely permeable sphere of radius a that could count the number of molecules within its volume at each instant, perform a time average, and use this information to estimate the surrounding concentration [6]. In the case of temperature sensing, the analogous instrument is a permeable sphere of radius a that records the temperature $T(\vec{x},t)$ at each point within its volume at each instant $t \in [0,\tau]$, performs a volume and time average, and then uses the result as the temperature estimate $\hat{T}$ (Fig. 9A). We assume the medium to be homogeneous and in thermal equilibrium, with average temperature $\overline{T}$. The key ingredient is the two-point correlation function for the temperature fluctuations obtained in the regime of linear irreversible thermodynamics [39]

$$\begin{aligned} &\langle (T(\vec{x},t)-\overline{T})(T(\vec{x}\,',t')-\overline{T})\rangle \\ &= \frac{k_B\overline{T}^2}{\rho c_s}\left(\frac{\rho c_s}{4\pi K|t-t'|}\right)^{3/2}\exp\left[-\frac{\rho c_s||\vec{x}-\vec{x}\,'||^2}{4K|t-t'|}\right], \end{aligned} \tag{34}$$

where k_B is Boltzmann's constant and the material properties ρ, c_s, and K are the mass density, specific heat, and thermal conductivity of the medium respectively. The variance in the estimator is computed by integrating the two-point correlation function in Eq. 34 in both space and time. The result has the following short- and long-time limits (see Appendix C.A),

$$\frac{\sigma(\hat{T})}{\overline{T}} = \sqrt{\frac{k_B}{C}} \times \begin{cases} 1 & \tau \to 0 \\ \sqrt{4\tau_D/(5\tau)} & \tau \gg \tau_D, \end{cases} \tag{35}$$

where we have introduced the heat capacity of the medium contained within the instrument $C = 4\pi a^3 \rho c_s/3$ and the timescale for temperature fluctuations to diffuse across the instrument $\tau_D = \rho c_s a^2/K$ [39]. Equation 35 has an intuitive interpretation: the variance falls off with the heat capacity of the instrument (in units of k_B) because if the heat capacity is large, a large fluctuation in thermal energy corresponds to a small fluctuation in temperature. The variance is further decreased in the long-time limit by the number τ/τ_D of

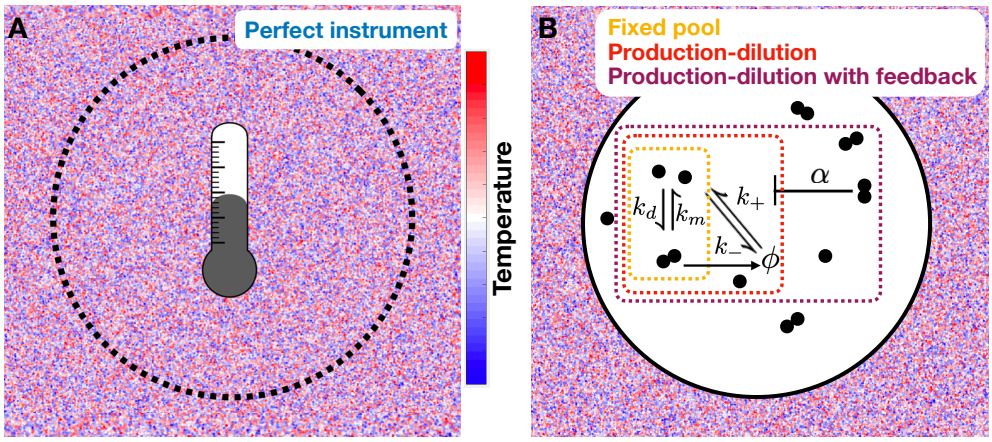

Figure 9: Temperature sensing (A) via an analog of Berg and Purcell's [6] perfect instrument for concentration sensing, and (B) via a protein thermometer. Based on the TlpA protein, monomers reversibly dimerize, monomers are expressed, monomer and dimers are diluted by cell division, and dimers inhibit monomer expression.

independent measurements the instrument can make, where independence is defined by the diffusion time.

For water at room temperature, $\rho \approx 1$ g/cm^3, $c_s \approx 4$ J/(g·K), and $K \approx 0.6$ J/(s·m·K). For a cell radius of $a \approx 1$ μm, the error in an instantaneous measurement, defined as $\tau \to 0$, according to Eq. 35 is $\sigma(\hat{T})/\overline{T} \approx 10^{-6}$. The diffusion time is $\tau_D \approx 6$ μs, after which the error drops further due to time averaging (Fig. 10, blue). Clearly the extrinsic fluctuations in the medium itself are not limiting, as it is unlikely that a cell needs to estimate temperature to less than one part in a million. This finding agrees with the conclusions of Dusenbery, whose approach was more heuristic [24].

2. Biochemical Models

Of course, cells are not perfect thermometers. They detect temperature indirectly through molecular or mechanical properties [100, 61, 70]. Therefore, to investigate the intrinsic limits imposed by the detection mechanism itself, we must develop a model that

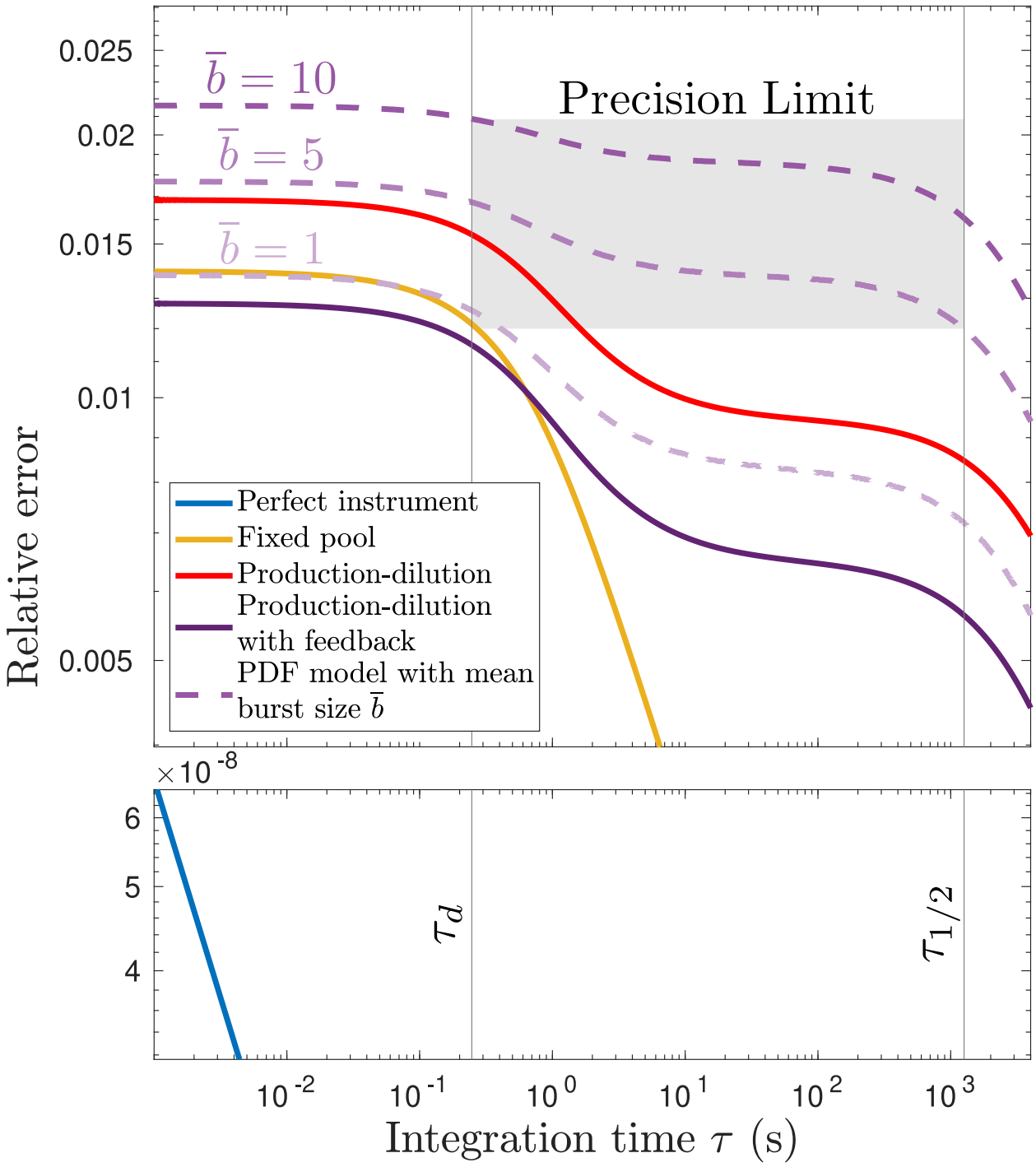

Figure 10: Relative temperature estimation error $\sigma(\hat{T})/\Delta T$ as a function of monomer-number integration time τ. We predict that the error is bounded from below by 2% (gray box). Parameters are estimated from data as described in the text.

accounts for the information actually available to the cell. Here we focus on the molecular mechanism of protein thermometry, in which proteins' conformational states are temperature dependent. Protein thermometers are ubiquitous: for example, temperature-dependent oligomerization, unfolding or misfolding, and methylation of proteins drive, in various combinations, the heat shock response [71], high-temperature response [56, 101], and thermotaxis response [69, 57, 90] in bacteria. In these cases, a temperature-induced conformational change is generally followed by negative feedback. In the high temperature response, the negative feedback is due to transcriptional repression, for example via dimers repressing monomer production as discussed herein; in the heat shock response, it is due to proteases degrading or chaperones conformationally changing the oligomers that form [71]; in *E. coli* thermotaxis, it is due to the methylation of the receptors [57, 90].

For concreteness, we consider the protein TlpA in *S. typhimurium*, which includes these common features but is otherwise relatively simple and experimentally well characterized. A step-increase in temperature results in a sustained increase in TlpA level, suggesting that TlpA responds to absolute temperature [56]. TlpA forms homodimers, with the dimer favored at low temperatures and the monomer favored at high temperatures [62, 56]. The dimer binds to the promoter region of the *tlpA* gene and inhibits its expression [55], resulting in negative feedback. TlpA is a canonical protein thermometer, and its mechanism has been used to engineer other thermal switches [92, 93].

a. The "Fixed Pool" Model

Suppose that two TlpA molecules associate with rate k_d and dissociate with rate k_m [62] (Fig. 9B, yellow). Subject to these reactions alone, the total number of TlpA units $n = m+2d$ is conserved, where m and d are the numbers of monomers and dimers respectively. Therefore we refer to this as the "fixed pool" (FP) model. The mean fraction $f = \overline{m}/n$ of TlpA units in the monomeric state has been measured as a function of temperature at physiological concentrations using circular dichroism spectroscopy [56, 50]. We find that the data are well described by a sigmoid $f(T) = \{1+\exp[-4(T-T_M)/\Delta T]\}^{-1}$ with half-maximal temperature $T_M = 39$ °C and width $\Delta T = 6.3$ °C [the factor of 4 ensures that $f'(T_M) = 1/\Delta T$]. This is a

fit to experimental measurements that is used as an input to our model, not a prediction of it. For details, see Appendix C.B. We assume that the cell infers the temperature from the mean monomer number, which it estimates from the time average $\hat{m}_\tau = \tau^{-1}\int_0^\tau m(t)dt$ [6] (we find similar results if temperature is instead inferred from the dimer number, see Appendix C.D). In the appendix we also consider maximum likelihood estimation [20], which in this case has the least squared error of all possible estimators, and find that it performs similarly to the naive time average considered here, see Appendix C.E.

To convert the error in monomer number estimation to that in temperature estimation, we use linear error propagation [6], $\sigma(\hat{T}) = \sigma(\hat{m}_\tau)/|d\overline{m}/dT| = \sigma(\hat{m}_\tau)/(nf')$, where the second step follows from $\overline{m} = nf$. To find $\sigma(\hat{m}_\tau)$, we perform the second-order Kramers-Moyal expansion and linearize to obtain the fluctuations [59, 43, 60]. The result is

$$\frac{\sigma(\hat{T})}{\Delta T} = \frac{\sigma_{\mathrm{FP}}(m)}{nf'\Delta T} \times \begin{cases} 1 & \tau \to 0 \\ \sqrt{2\tau_d/\tau} & \tau \gg \tau_d, \end{cases} \tag{36}$$

where $\sigma^2_{\mathrm{FP}}(m) = 2nf(1-f)/(2-f)$ is the instantaneous variance in the monomer number and $\tau_d = c(k_d\overline{m})^{-1}$ is the autocorrelation time, with $c = (1-f)/[2(2-f)]$ a numerical factor, see Appendix C.C.3. Equation 36 has an intuitive interpretation: the factor $nf(1-f)$ in $\sigma^2_{\mathrm{FP}}(m)$ is the variance of the binomial distribution, which arises because the molecules switch between the monomer and dimer states. The additional factor $2/(2-f)$ is an increase in the noise due to the fact that dimerization further discretizes the monomer number beyond that of a pure binomial process, as the monomer number can only change by two [96]. Finally, $(k_d\overline{m})^{-1}$, which sets τ_d, is the timescale for a monomer to form a dimer with any other monomer. As in Eq. 35, the variance in the long-time limit of Eq. 36 is reduced by the number τ/τ_d of independent measurements made.

A cell must be able to determine temperature changes to a better precision than the width of its temperature sensitive region ΔT. For this reason, we define relative error with respect to ΔT, not the mean temperature $\overline{T}$, in Eq. 36 and thereafter. This is in contrast to the case of the perfect instrument (Eq. 35), for which there is no cell-defined temperature-sensitive region. It is worth noting that even if $\overline{T}$ were replaced with ΔT in Eq. 35, the

relative error would increase by roughly two orders of magnitude, which is still far less than that of the biochemical models considered in this work.

When $T = T_M$, we have $f = 1/2$ and $f' = 1/\Delta T$, and the instantaneous error in Eq. 36 reduces to $\sigma(\hat{T})/\Delta T = 1/\sqrt{3n}$. We see that the error decreases with the square root of the number of TlpA molecules n, as expected for counting noise.

The TlpA dimer number was experimentally estimated to be $\overline{d} = 684$ at $T = 37$ °C [56], where $f = 0.2$. Because $f = \overline{m}/(\overline{m} + 2\overline{d})$, we have $\overline{m} = 2\overline{d}f/(1-f) = 342$. In the fixed pool model, this implies $n = \overline{m}/f = 1710$, and therefore an instantaneous error of $\sigma(\hat{T})/\Delta T = 1.4\%$ (Fig. 10, yellow). To see how sensing improves with time integration, we need to estimate the dimerization rate k_d. We are unaware of an experimental estimate for the dimerization rate of TlpA. However, TlpA is a coiled-coil, and the dimerization rate of engineered coiled-coils has been measured at $k_d V = 4 \times 10^5$ $(\text{M}{\cdot}\text{s})^{-1}$ [17]. Given the bacterial volume of $V = 1$ μm^3 [108], this results in an autocorrelation time of $\tau_d = 0.3$ s at $f = 1/2$, beyond which the error falls off. The intrinsic noise from molecular detection (Fig. 10, yellow) clearly dominates over the extrinsic noise from temperature fluctuations in the medium (Fig. 10, blue).

b. The "Production-Dilution" Model

The fixed pool model is unrealistic because in cells the protein number is not actually fixed. Instead, proteins are produced via gene expression and lost by active degradation or dilution from cell division. As we are not aware of evidence that TlpA is actively degraded, we consider dilution here. Specifically, we introduce a production rate k^+ for the monomer and a dilution rate k^- for both the monomer and dimer. We call this the "production-dilution" model (Fig. 9B, red). Experiments [56, 36] suggest that neither k^+ nor k^- is strongly temperature dependent (see Appendix C.F), and therefore we assume that the dominant temperature dependence is via f. Because cell division is much slower than monomer binding [75], we consider the limit $k^- \ll k_d \overline{m}$.

Using the same stochastic techniques as above, we find that the mean and variance of

the monomer number become $\overline{m} = fk^+/k^-$ and

$$\sigma^2(m) = \sigma^2_{\rm FP}(m) + \frac{f^2\sigma^2(n)}{(2-f)^2}, \tag{37}$$

where $\sigma^2(n) = (7-3f)k^+/(4k^-)$ is the variance of the (now fluctuating) pool size $n = m+2d$, and $\sigma^2_{\rm FP}(m)$ as given beneath Eq. 36 is here written in terms of the mean pool size $\overline{n} = \overline{m}/f$ (see Appendix C.C.4). The second term in Eq. 37 is always positive, showing that pool fluctuations due to protein turnover increase the noise, as expected. The experimentally estimated monomer $\overline{m} = 342$ at $T = 37\,^\circ$C where $f = 0.2$ [56] implies $k^+/k^- = \overline{m}/f = 1710$. Using $f = 1/2$ and this vale for k^+/k^-, we see that the instantaneous error (Fig. 10, red) is increased from that of the FP model (Fig. 10, yellow). The full τ-dependent expression for $\sigma(\hat{T})/\Delta T$ is calculated using $k^- = \ln(2)/\tau_{1/2} \approx 2$ hr^{-1} from cell division [68], and we see that the relative error has two clear bends at the dimerization and dilution timescales τ_d and $\tau_{1/2}$ respectively (Fig. 10, red).

c. The "Production-Dilution with Feedback" Model

Thus far we have not yet accounted for the fact that TlpA exhibits negative feedback: the TlpA dimer binds to the promoter region of the *tlpA* gene and inhibits its expression [55]. To incorporate this autorepression, we replace the monomer production rate k^+ with the function $k^+/(1+\alpha d)$. We call this the "production-dilution with feedback" (PDF) model (Fig. 9B, purple). The parameter α describes the autorepression strength, and its inverse sets where half-maximal expression occurs. Experiments [56] suggest that α is not strongly temperature dependent (see Appendix C.F), and therefore we continue to assume that the dominant temperature dependence is via f. With autorepression, we find (see Appendix C.C.4.a) that the mean monomer number becomes

$$\overline{m} = \frac{f}{\alpha(1-f)}\left[\sqrt{1+\frac{2\alpha k^+(1-f)}{k^-}} - 1\right], \tag{38}$$

and the variance obeys Eq. 37 with $\sigma^2(n)$ acquiring an α dependence (see Appendix C.C.4.b). We have checked that Eqs. 37 and 38 agree with stochastic simulations [44] (see Appendix C.G). Both Eq. 37 and Eq. 38 decrease monotonically with α, showing that autorepression

reduces both the monomer number variance and its mean. The latter effect dominates, such that relative fluctuations $\sigma(m)/\overline{m}$ increase with autorepression strength. In particular, we find that the relative fluctuations $\sigma(m)/\overline{m}$ scale as $\alpha^{1/4}$ and as $c + s\alpha$ for large and small α respectively, where c and s are independent of α. For $0 < f < 0.77$, the slope s is positive. Because we are generally concerned with values of f near 1/2, we conclude that $\sigma(m)/\overline{m}$ increases monotonically for all α.

The increase in relative fluctuations with autorepression is offset by an increase in temperature sensitivity. To see this, we recognize that the instantaneous relative error can be written $\sigma(\hat{T})/\Delta T = [\sigma(m)/\overline{m}]/[|d\overline{m}/dT|(\Delta T/\overline{m})]$, again by error propagation. The first term in brackets is the relative fluctuations while the second term is the sensitivity: the derivative $d\overline{m}/dT$ scaled by the characteristic quantities $\overline{m}$ and ΔT. Differentiating Eq. 38, the sensitivity evaluates to

$$\frac{d\overline{m}}{dT}\frac{\Delta T}{\overline{m}} = \frac{f'\Delta T}{(1-f)}\left[\frac{1}{f} - \frac{1}{2} - \frac{1}{2\sqrt{1+2\alpha k^+(1-f)/k^-}}\right]. \tag{39}$$

Equation 39 is an increasing function of α, showing that autorepression increases the sensitivity. This result in consistent with the fact that mutations that target the autorepression result in a weakened dependence of monomer number on temperature [56].

The tradeoff between increasing relative fluctuations and increasing sensitivity leads to an optimal autorepression strength $\alpha^* = 1.75k^-/k^+$ that minimizes the error in instantaneous temperature sensing $\sigma(\hat{T})/\Delta T$ at $T = T_M$ (see Appendix C.C.5). We insert the experimental values $\overline{m} = 342$ and $f = 0.2$ [56] with our optimum $\alpha = \alpha^* = 1.75k^-/k^+$ into Eq. 38 to obtain $k^+/k^- = 2521$. Using these values for k^+/k^- and α, $f = 1/2$, and $k^- = 2$ hr^{-1}, we see that the error (Fig. 10, purple solid) is reduced from the case without feedback (Fig. 10, red).

Finally, we account for a ubiquitous source of additional noise in bacterial gene expression, namely bursts. Bursts of protein production can occur at the transcriptional level, due to binding and unbinding at the promoter region [95], and at the translational level, due to multiple proteins being produced from a single transcript [120]. There isn't any detailed information about the kinetics of the promoter binding, so we attempt to include this by

assuming that it is diffusion-limited, though this could be incorrect. In our case the promoter binding timescale is sufficiently fast compared to the protein production timescale that transcriptional bursting can be neglected (see Appendix C.H and [32, 109]) and therefore we focus on translational bursts. Specifically, we perform stochastic simulations [44] of the PDF model in which each production event generates b TlpA proteins instead of one, where b is geometrically distributed with mean $\overline{b}$ [120], and we take $k^+ \to k^+/\overline{b}$ to leave the mean monomer number $\overline{m}$ unchanged. We see in Fig. 10 that the temperature estimation error increases with mean burst size $\overline{b}$, as expected (purple dashed).

Our results provide a quantitative prediction for the precision with which a cell can estimate temperature using a protein thermometer. A temperature-sensitive behavioral response is likely to occur on a timescale slower than monomer binding τ_d but faster than cell division $\tau_{1/2}$. Fig. 10 shows that the estimation error is relatively insensitive to the integration time in this range. In particular, for a typical bacterial protein burst size of $\overline{b} = 5{-}10$ molecules [120], we predict that the cell can estimate temperature to within 2% (Fig. 10, gray box).

d. Comparison with LacZ Reporter Data

How does the predicted bound of 2% precision compare to observed thermosensing thresholds in experimental systems? The transcriptional activity of TlpA has been measured *in vivo* [56] using a Miller assay with a LacZ reporter [74, 42]. Miller units are proportional to the number of TlpA production events and therefore include time integration while excluding noise downstream of TlpA. Measurements at temperatures T_1 and T_2 below and above the transition temperature, respectively, provide an estimate of the thermosensing error $\sigma(\hat{T})/\Delta T$, where $\Delta T = T_2 - T_1$, and $\sigma(\hat{T})$ is evaluated from the measured uncertainties using linear error propagation (see Appendix C.I for details). Using this procedure, we find $\sigma(\hat{T})/\Delta T = 24\%$. This value is larger than 2%, indicating that this protein thermometer obeys the predicted bound. Modeling the LacZ reporter explicitly in the simplified model without bursts, we find a relative error of 6.7%. If we incorporate bursts, the predicted bound becomes 20−30%, which is consistent with the experimental observation of 24% (see Appendix C.J). The intuitive reason for the increase in the bound is as follows. Denoting

the amount of LacZ, also called β-galactosidase, at the end of one cell cycle by β, we find that the sensitivity $|d\overline{\beta}/dT|/(\Delta T/\overline{\beta})$ is independent of the burst size, but the relative fluctuations in the reporter $\sigma(\beta)/\overline{\beta}$ increases as the burst size of TlpA increases. We tune the reaction rates such that the mean amount of TlpA dimers, which were measured in experiments [56], is independent of the TlpA burst size. However, a larger burst size means that LacZ is produced less frequently, so it has larger relative fluctuations.

The excellent agreement between the predicted bound and the experimental observation may be partly fortuitous. First, the data may include purely experimental sources of error associated with the Miller assay, which would increase the observed error. Second, the Miller assay is a population measurement, which would decrease the observed error: it reports $[\sigma(\hat{T})/\Delta T]/\sqrt{N}$, where N is the number of independently responding units within the population of N_{cells}, and the degree to which cells respond in a correlated ($N \to 1$) or uncorrelated ($N \to N_{\text{cells}}$) manner is unclear. Third, the population likely includes natural cell-to-cell variability [38], which would increase the observed error. These unknowns underscore the need for measurements of temperature sensitivity at the single-cell level. We are not aware of any such measurement for a protein thermometer.

C. Discussion

Molecular thermometers drive a variety of cell behaviors, and it is natural to ask how our work could be extended. Many thermosensors, including TlpA, are speculated to cause threshold-like responses, where the cell cares only if the temperature is above a particular threshold, not the value of the temperature itself. For this task, decision theory or optimal stopping [106, 7, 91] may be more appropriate than the time-integrated statistics we investigate here. Furthermore, many thermosensors are used for thermotaxis, the motion of a cell toward an optimal temperature. Here the sensory network is more complicated [57, 90] and the task is also different: the cell cares about the value of both the temperature and its spatial gradient. It would be interesting to integrate our findings into a model of thermotaxis to investigate the physical limits to the precision of that behavior.

Guided by a canonical protein thermometer, we have derived the physical limits to the precision of cellular temperature sensing. Unlike for many other types of cell sensing, the precision of temperature sensing is evidently not limited by the extrinsic noise inherent to the environmental signal itself. Instead, the precision is limited by the biochemical details of the molecular thermometer inside the cell. Specifically, the relative error falls off with the square root of the number of molecules and the number of correlation times, as expected for systems dominated by biochemical noise. Developing a model based on the experimental features and measured parameters of the TlpA protein, we predict a sensitivity threshold of 2%, which we find is consistent with the observed thermosensing threshold in bacteria. Our work advances the understanding of cell sensing and lays the groundwork for further exploration of temperature-sensitive cell behavior.

V. Conclusions and Future Work

In this dissertation, we have used techniques from stochastic processes and information theory to study how well cells can sense aspects of their environment. In the first project, we probed the implications of criticality for biochemical sensing. We found a trade-off between high steady state mutual information and low information rate at criticality. High mutual information requires a large separation of timescales that may be unrealistic. This supports previous findings that criticality can be detrimental for biochemical sensing [107], in contrast to other biological systems, such as propagating signals in biofilms [65], the auditory system [54], or neural avalanches [73], though recent results cast doubt on this last example [80].

In the other two projects, we derived bounds on the amount of information available to the cell about its environment along the tradition initiated by Berg and Purcell [6]. The first of these combined methods from fluid dynamics and stochastic processes to understand limits to cancer cells detecting a flow direction while metastasizing via autologous chemotaxis. We compared two strategies, pure endocytosis and pure reversible binding, for signal transduction and found that reversible binding was superior to endocytosis. This seems counterintuitive, given past work on gradient sensing [26]. However, there is not an externally imposed gradient here. The cells are producing the signal that they are trying to detect, and removing the molecules from the environment reduces the time that they interact with the flow, thus favoring reversible replenishment.

The project regarding temperature sensing built off of a previous attempt at this problem before the chemical pathways for sensing temperature were understood [24]. We used techniques from linear irreversible thermodynamics to conclude that the physical temperature fluctuations were not limiting [39]. Temperature sensing is indirect and is limited by the tools used to sense the temperature, in contrast to most other types of cell sensing. Despite this, we found that the cell has a reasonable amount of information from a protein thermometer like TlpA, consistent with experimental observations.

There are two clear directions for future work. We can build upon the projects regarding criticality and flow sensing, as detailed below.

A. Extension for Criticality and Sensing

Morphogenesis is a highly complex and coordinated process. In the developing *Drosophila melanogaster*, the embryo must grow rapidly and then undergo segmentation. The first step in segmentation involves differentiating the anterior and posterior of the embryo. The key players here are a maternally provided Bicoid concentration gradient that is transduced into a sharp step-like Hunchback profile. After this primary boundary is formed, additional boundaries are formed. There is disagreement on whether criticality or bimodality is helpful for this kind of boundary formation [67, 63].

We can address this question by formulating a model of the Bicoid-Hunchback system, identifying bifurcations in the deterministic dynamics to find the critical point and temperature- and field-like variables, and study the precision of boundary formation as these parameters are varied. There is evidence that only three Bicoid binding sites [23] and two Hunchback binding sites [67] on the *hunchback* promoter are sufficient for proper embryo development. Fluctuations in the Bicoid profile are washed away due to the slow binding to the promoter [29]. This leads us to propose a simple model for the Hunchback dynamics alone

$$\frac{dx_i}{dt} = k_b \frac{b_i^3}{B^3 + b_3^3} + k_x \frac{x_i^2}{H^2 + x_i^2} - \nu x_i + \gamma \nabla^2 x_i, \tag{40}$$

where ∇^2 is the discrete Laplacian. This model exhibits a pitchfork bifurcation, like our work on the Schlögl model. The bifurcation occurs where the second derivative with respect to x_i vanishes: $x_c = H/\sqrt{3}$. We find the effective temperature and field variables

$$\theta = \frac{4\left(8H\nu/\sqrt{3} - 3k_x\right)}{9k_x}, \qquad h_i = \frac{8\left(-4\nu H/\sqrt{3} + 4f(b_i) + k_x\right)}{9k_x}, \tag{41}$$

where we have introduced $f(b)$ as shorthand for the Bicoid-induced production $f(b_i) = k_b b_i^3/(B^3 + b_i^3)$. We see that the Bicoid gradient acts as a non-uniform magnetic field that biases the cells towards high or low Hunchback number, depending on their position along the embryo.

With the mapping established, the next step is to study the effect of tuning θ on the sharpness of the boundary. Based on past work [29], a suitable measure for the sharpness is

$$\Delta = \frac{\overline{x}_I - \overline{x}_{I+1}}{\frac{1}{2}(\sigma(x_I) + \sigma(x_{I+1}))}, \qquad I = \text{argmax}_i(\overline{x}_i - \overline{x}_{i+1}). \tag{42}$$

In words, we would run many trials with the same parameter values, compute the average Hunchback profile, and determine the position where the Hunchback number changes its position the most. We say that the boundary occurs there, and the measure of sharpness is the difference divided by the average of the standard deviation of Hunchback numbers of the cells involved. We can also study the effect of tuning the communication strength γ. Past work [29] found an optimal, low diffusion coefficient. The formalism presented here has imagined the embryo as one-dimensional, and it may be important to extend this to two or three dimensions.

B. Extension for Flow Sensing

Further experiments on autologous chemotaxis revealed that cells can migrate in the opposite direction if the cell density is high enough [94]. This is something that we can study using our methods. We can focus on a single cell nearby other cells. A simple first pass at the problem would be to assume the presence of other cells creates a non-zero background so that $\lim_{r\to\infty} c = c_0$ instead of zero. It is possible to compute the mean anisotropy measure using the same techniques as in our published work, and we find

$$\overline{A} = \frac{\epsilon w}{8(2+\tilde{\alpha})} \frac{\tilde{\beta} - \tilde{\alpha} c_0 a^3}{\tilde{\beta} + c_0 a^3}. \tag{43}$$

For the pure endocytosis/ absorbing model, we see that this does switch sign if c_0 exceeds some critical concentration. The results for the reversible binding model are obtained by taking $\tilde{\alpha} = 0$, and we see that increasing the background concentration decreases the magnitude of the mean but does not change its sign. One remaining problem with this approach is connecting c_0 to experimental cell densities to see if we can postdict the transition seen in experiments.

We can also connect this work to the broader line of work done on collective sensing [114, 34]. We can imagine two schemes for collective flow sensing. In the first, each cell tries to estimate the flow direction through the anisotropy over its own surface. When the cells are far apart, we expect this strategy to reduce to the case of an isolated cell. When they are close together, we expect this strategy to perform poorly, as cells will detect molecules from other cells, and this will behave qualitatively like a background concentration.

Another scheme is one where each cell measures the flux of molecules through its own surface. Each cell tries to move away from the others, via something like contact inhibition of locomotion, and the degree to which they do so is proportional to the flux. This allows a collective anisotropy between different cells' fluxes. We expect a crossover here. When the cells are close together, the population should sense like a cell with larger radius. However, when the separation between cells is large enough, the cells will be effectively non-interacting. This means they will have nearly identical fluxes through their surfaces, and the population will be unable to sense the flow direction.

It is not possible to determine the flow lines analytically for multiple cells, so a numerical approach must be taken. This will require specifying a mesh, which complicates performing particle based simulations in continuous space. There are multiphysics programs, namely COMSOL, that can generate meshes for solving partial differential equations, solve for the flow lines, and find the mean concentration by solving the convection-diffusion equation. This approach will be directly applicable to the endocytosis/ absorbing model and seems to be the most sensible way forward on this end.

Appendix A Supplement for "Multicellular Sensing at a Feedback-Induced Critical Point"

A. Mutual Information for a Multivariate Gaussian

Our goal is to calculate the mutual information between the various combinations of the components of $\vec{\delta\ell}$ and $\vec{\delta x}$. In general, note that we have

$$I(X,Y) = H(X) + H(Y) - H(X,Y), \tag{44}$$

where X and Y are different variables (possibly sets of them) and H is the Shannon entropy (in nats). The linearized stochastic differential equations describe an Ornstein-Uhlenbeck process, and the solution is a Gaussian random variable. If X comes from a D-dimensional Gaussian distribution with covariance matrix $\mathcal{C}$, one may show that the entropy is

$$H(X) = \frac{D}{2}\log(2\pi e) + \frac{1}{2}\log(\det(\mathcal{C})). \tag{45}$$

A key property that is useful in this analysis is the fact that taking a marginal of a multi-dimensional Gaussian yields another Gaussian and does not alter the covariances between the remaining variables.

Suppose that we have some combination of Gaussian variables Z that are partitioned into two sets X and Y, where Z has N components, X has N_x components, and Y has $N_y = N - N_x$ components (any additional variables have been integrated out). Our covariance matrix may be decomposed in the following way

$$\mathcal{C} = \begin{bmatrix} \mathcal{C}_{XX} & \mathcal{C}_{XY} \\ \mathcal{C}_{YX} & \mathcal{C}_{YY} \end{bmatrix}, \tag{46}$$

where $\mathcal{C}_{YX} = \mathcal{C}_{XY}^T$. The entropies of the two subsets are

$$\begin{aligned} H(X) &= \frac{N_x}{2}\log(2\pi e) + \frac{1}{2}\log(\det(\mathcal{C}_{XX})), \\ H(Y) &= \frac{N - N_x}{2}\log(2\pi e) + \frac{1}{2}\log(\det(\mathcal{C}_{YY})). \end{aligned} \tag{47}$$

The joint entropy will cancel off the constants, so the mutual information between X and Y is

$$I(X,Y) = -\frac{1}{2}\log\left(\frac{\det(\mathcal{C})}{\det(\mathcal{C}_{XX})\det(\mathcal{C}_{YY})}\right). \tag{48}$$

B. Mutual Information for a Single Site

Our linearized equations may be written in the form

$$d\vec{Y}_t = \mathbb{A}\vec{Y}_t dt + \mathbb{B}d\vec{W}_t, \tag{49}$$

where $\vec{Y}_t = [\delta x(t), \delta\ell(t)]^T$ describes the molecule numbers, $\vec{W}_t = [W_x(t), W_\ell(t)]^T$ describes the noise in production and degradation, and the matrices are

$$\mathbb{A} = \begin{bmatrix} -c & k_1^+ \\ 0 & -k_\ell^- \end{bmatrix}, \qquad \mathbb{B} = \begin{bmatrix} \sqrt{2d(x_c)} & 0 \\ 0 & \sqrt{2k_\ell^+} \end{bmatrix}. \tag{50}$$

If the initial condition is $\vec{Y}_0$, the general solution (for general matrices and dimensionalities) is

$$\vec{Y}_t = e^{\mathbb{A}t}\vec{Y}_0 + \int_0^t e^{\mathbb{A}(t-s)}\mathbb{B}d\vec{W}_s. \tag{51}$$

This may be proven using the substitution $\vec{Z}_t = e^{-\mathbb{A}t}\vec{Y}_t$ and using Itô's lemma. We are interested when the fluctuations about the steady state mean, so we take $\vec{Y}_0 = 0$.

We need to evaluate the steady state covariances. Since the means are zero, it suffices to compute $\left\langle Y_t^{(i)} Y_t^{(j)} \right\rangle$ as $t \to \infty$. This can be done directly with our solution. Using the Itô isometry, changing the integration variable to $t' = t - s$ and taking the aforementioned limit, we find

$$\left\langle Y^{(i)} Y^{(j)} \right\rangle = \int_0^\infty [e^{\mathbb{A}t}\mathbb{B}\mathbb{B}^T(e^{\mathbb{A}t})^T]_{i,j} dt. \tag{52}$$

for general matrices and dimensionalities. The matrix exponential in our case is

$$e^{\mathbb{A}t} = \begin{bmatrix} e^{-ct} & -k_1^+ \dfrac{e^{-ct} - e^{-k_\ell^- t}}{c - k_\ell^-} \\ 0 & e^{-k_\ell^- t} \end{bmatrix}. \tag{53}$$

The result when $c = k_\ell^-$ may be obtained by using L' Hôpital's rule. The full covariance matrix is

$$\mathcal{C} = \left\langle \vec{Y}\vec{Y}^T \right\rangle = \begin{bmatrix} \dfrac{d(x_c)}{c} + \dfrac{(k_1^+)^2\overline{\ell}}{c(c+k_\ell^-)} & \dfrac{k_1^+\overline{\ell}}{c+k_\ell^-} \\ \dfrac{k_1^+\overline{\ell}}{c+k_\ell^-} & \overline{\ell} \end{bmatrix}. \tag{54}$$

The diagonal terms are the variances, while the off-diagonal terms are the covariance between δx and $\delta\ell$.

Before moving forward, it will be helpful to express things in terms of the "Landau" parameters x_c, h, and θ. Using the definitions in the main text, one can solve for the reaction rates

$$\begin{aligned} k_1^+ &= k_1^- \frac{x_c}{3\overline{\ell}} \frac{1+3\theta+3h}{1+\theta}, \\ k_2^+ &= \frac{k_1^-}{x_c(1+\theta)}, \quad k_2^- = \frac{k_1^-}{3x_c^2(1+\theta)}. \end{aligned} \tag{55}$$

Using these, we may also solve for $d(x_c)$ and c

$$d(x_c) = \frac{k_1^- x_c(4+3\theta)}{3(1+\theta)}, \qquad c = \frac{k_1^-\theta}{1+\theta}. \tag{56}$$

Note that as $\theta \to \infty$, these quantities become what you would expect in the absence of feedback, provided that we replace x_c by the appropriate mean $\overline{x} = k_1^+\overline{\ell}/k_1^-$.

Now we compute the mutual information between the ligand and readout using Eqs. 48, 54 with the result

$$I(\delta x, \delta\ell) = \frac{1}{2}\log\left(1 + \frac{c(k_1^+)^2\overline{\ell}}{d(c+k_\ell^-)^2 + k_\ell^-(k_1^+)^2\overline{\ell}}\right). \tag{57}$$

Casting the rates into expressions of the Landau parameters and setting $h = 0$ gives

$$I(\delta x, \delta\ell) = \frac{1}{2}\log\left(1 + \frac{\theta(3\theta+1)^2}{3(\overline{\ell}/x_c)(3\theta+4)[(k_\ell^-/k_1^-)(\theta+1)+\theta]^2 + (k_\ell^-/k_1^-)(\theta+1)(3\theta+1)^2}\right). \tag{58}$$

This is a complicated expression that vanishes as $\theta \to 0$ unless $k_\ell^-/k_1^- \to 0$. If the ligand timescales are slow, then this simplifies to the expression given in the text.

C. Information Rate for a Single Site

The information rate for Gaussian process where a scalar signal s linearly drives a scalar response x is

$$R = -\frac{1}{4}\int_{-\infty}^{\infty} \log\left(1 - \frac{|S_{s,x}(\omega)|^2}{S_{s,s}(\omega)S_{x,x}(\omega)}\right) d\omega. \tag{59}$$

where S's are elements of the cross-spectrum $\mathbb{S}$, which satisfies

$$\left\langle \hat{\vec{y}}(\omega)\hat{\vec{y}}^{\dagger}(\omega')\right\rangle = 4\pi^2\mathbb{S}(\omega)\delta(\omega-\omega'), \tag{60}$$

where we have combined the signal and response variables into a single vector as before [112, 83]. We are using the convention that the Fourier transform is defined as

$$\hat{\vec{y}}(\omega) = \int_{-\infty}^{\infty} \vec{y}(t)e^{-i\omega t}dt. \tag{61}$$

A vector of independent delta-correlated white noises $\vec{\eta}$ has a constant cross-spectrum

$$\left\langle \hat{\vec{\eta}}(\omega)\hat{\vec{\eta}}^{\dagger}(\omega')\right\rangle = 2\pi\mathbb{I}\delta(\omega-\omega'). \tag{62}$$

We can solve for the cross-spectrum by taking the Fourier transform of Eq. 8. The ligand doesn't depend on the readout, so we can solve for this first. The equation becomes

$$\hat{\delta\ell}(\omega) = \frac{\sqrt{2k_\ell^+}\hat{\epsilon}(\omega)}{k_\ell^- + i\omega}. \tag{63}$$

Using this to find the power spectrum of the ligand fluctuations yields

$$S_{\ell,\ell}(\omega) = \frac{k_\ell^+}{\pi((k_\ell^-)^2+\omega^2)}. \tag{64}$$

Taking the Fourier transform of the second equation and using the result from the first gives

$$\hat{\delta x}(\omega) = \frac{\sqrt{2d}\hat{\eta}(\omega)}{c+i\omega} + \frac{k_1^+}{c+i\omega}\frac{\sqrt{2k_\ell^+}\hat{\epsilon}(\omega)}{k_\ell^- + i\omega} \tag{65}$$

When finding the cross-spectrum between δx and $\delta\ell$, the calculation is the same as the previous case, as the $\hat{\eta}$ term cancels, except we have an additional factor

$$S_{x,\ell}(\omega) = \frac{k_1^+}{c+i\omega}\frac{k_\ell^+}{\pi((k_\ell^-)^2+\omega^2)}. \tag{66}$$

For the power spectrum of δx, the two terms are independent and the result is

$$S_{x,x}(\omega) = \frac{d}{\pi(c^2+\omega^2)} + \frac{(k_1^+)^2}{c^2+\omega^2}\frac{k_\ell^+}{\pi((k_\ell^-)^2+\omega^2)}. \tag{67}$$

Plugging everything in, the information rate integral evaluates to

$$R = \frac{\pi}{2}\left(\sqrt{(k_\ell^-)^2 + \frac{(k_1^+)^2 k_\ell^+}{d}} - k_\ell^-\right). \tag{68}$$

Expressing this in terms of the Landau parameters gives the result in the main text.

D. Covariance Matrix for Multiple Cells

Our system of stochastic differential equations may be expressed in terms of circulant matrices. These matrices have a number of nice properties that will be used in the analysis, so it will be worthwhile to discuss them. A circulant matrix $\mathbb{M}$ is a square matrix such that the next column can be obtained by shifting the entries of the current column down by one and imposing periodicity. Concretely, they take the form

$$\mathbb{M} = \begin{bmatrix} m_0 & m_{N-1} & \dots & m_2 & m_1 \\ m_1 & m_0 & m_{N-1} & & m_2 \\ \vdots & m_1 & m_0 & \ddots & \vdots \\ m_{N-2} & & \ddots & \ddots & m_{N-1} \\ m_{N-1} & m_{N-2} & \dots & m_1 & m_0 \end{bmatrix}. \tag{69}$$

The discrete Laplacian on a ring with N sites is a special case of this with $m_0 = -2$, $m_1 = m_{N-1} = 1$, and zeroes in all other entries. All circulant matrices are simultaneously diagonalizable via a discrete Fourier transform. Since they are simultaneously diagonalizable, they all commute with each other. The set of circulant matrices is closed under matrix addition and multiplication. If a circulant matrix is invertible, its inverse is another circulant matrix. For each $j \in \{0, 1, ..., N-1\}$, there is an eigenvector

$$\vec{v}_j = \frac{1}{\sqrt{N}}\begin{bmatrix} 1 & e^{-2\pi i j/N} & \dots & e^{-2\pi i j(N-1)/N} \end{bmatrix}^T, \tag{70}$$

with eigenvalue

$$\lambda_{\mathbb{M}}(j) = \sum_{k=0}^{N-1} m_k e^{2\pi i j k/N}. \tag{71}$$

It is easy to check that this eigenbasis is orthonormal. For the discrete Laplacian, the eigenvalues are

$$\lambda_{\nabla^2}(j) = -2[1 - \cos(2\pi j/N)]. \tag{72}$$

We will use U to denote the unitary discrete Fourier transform, i.e. the matrix whose columns are the eigenvectors ordered from $j = 0, 1, ..., N-1$.

Now we will solve the system by casting it into the canonical form for an Ornstein-Uhlenbeck process and then using Eq. 51. As before, we introduce a vector $\vec{Y}_t = [\vec{\delta x}(t), \vec{\delta \ell}(t)]^T$ that describes both molecular profiles. We introduce a $6N$-dimensional vector of noises that are ordered as follows

$$d\vec{W}_t = \begin{bmatrix} \text{X chemical noises} \\ \text{X diffuse left noises} \\ \text{X diffuse right noises} \\ \text{L chemical noises} \\ \text{L diffuse left noises} \\ \text{L diffuse right noises} \end{bmatrix}. \tag{73}$$

The matrices $\mathbb{A}$ and $\mathbb{B}$ are best expressed in block form. If $\mathbb{I}_N$ is the N-dimensional identity matrix, we have

$$\mathbb{A} = \begin{bmatrix} -c\mathbb{I}_N + \gamma\nabla^2 & k_1^+ \mathbb{I}_N \\ 0 & -k_\ell^- \mathbb{I}_N + \gamma'\nabla^2 \end{bmatrix}. \tag{74}$$

The $\mathbb{B}$ matrix takes the form

$$\mathbb{B} = \begin{bmatrix} \sqrt{2d(x_c)}\mathbb{I}_N & \sqrt{\gamma x_c} D_L & \sqrt{\gamma x_c} D_R & 0 & 0 & 0 \\ 0 & 0 & 0 & \sqrt{2k_\ell^+}\mathbb{I}_N & \sqrt{\gamma' \bar{\ell}} D_L & \sqrt{\gamma' \bar{\ell}} D_R \end{bmatrix}, \tag{75}$$

where D_L (D_R) is a circulant matrix with $m_0 = -1$, $m_{N-1} = 1$ ($m_1 = 1$), and zero for all of the other entries. These matrices describe the anti-correlations associated with diffusing left and right respectively and they satisfy

$$D_L^T = D_R, \quad D_L D_R = D_R D_L = -\nabla^2. \tag{76}$$

With these definitions, our system of stochastic differential equations is in the standard form and the usual solution applies.

Next, we need to evaluate the matrices and integration that appear in Eq. 52. The product of $\mathbb{B}$ matrices is easy

$$\mathbb{B}\mathbb{B}^T = \begin{bmatrix} 2d(x_c)\mathbb{I}_N - 2\gamma x_c \nabla^2 & 0 \\ 0 & 2k_\ell^+ \mathbb{I}_N - 2\gamma' \bar{\ell} \nabla^2 \end{bmatrix} \tag{77}$$

Computing the matrix exponential is more involved. It is instructive to work with a 2×2 matrix. Consider the family of matrices

$$\mathbb{M}_N = \begin{bmatrix} a\mathbb{I}_N & b\mathbb{I}_N \\ 0 & c\mathbb{I}_N \end{bmatrix}. \tag{78}$$

For $N = 1$, the matrix exponential is

$$e^{\mathbb{M}_1 t} = \begin{bmatrix} e^{at} & b\dfrac{e^{at} - e^{ct}}{a - c} \\ 0 & e^{ct} \end{bmatrix}. \tag{79}$$

Working with the number 1 is similar to working with the identity matrix, both have multiplicative inverses and have commutative multiplication. In fact, a similar solution holds for arbitrary N

$$e^{\mathbb{M}_N t} = \begin{bmatrix} e^{a\mathbb{I}_N t} & b(a\mathbb{I}_N - c\mathbb{I}_N)^{-1}(e^{a\mathbb{I}_N t} - e^{c\mathbb{I}_N t}) \\ 0 & e^{c\mathbb{I}_N t} \end{bmatrix}, \tag{80}$$

here we have written it in a suggestive form. For our problem, it will be convenient to introduce the shorthand

$$\begin{aligned} \alpha &= -c\mathbb{I}_N + \gamma\nabla^2, \\ \beta &= -k_\ell^- \mathbb{I}_N + \gamma'\nabla^2, \\ \alpha' &= 2d(x_c)\mathbb{I}_N - 2\gamma x_c \nabla^2, \\ \beta' &= 2k_\ell^+ \mathbb{I}_N - 2\gamma'\bar{\ell}\nabla^2 = -2\bar{\ell}\beta. \end{aligned} \tag{81}$$

All of these matrices are circulant, so they commute and are diagonalizable. The first two have strictly negative eigenvalues, while the last two have positive eigenvalues, so they are all

invertible. In light of the single cell result in Eq. 53, a natural candidate for the exponential of $\mathbb{A}$ is

$$e^{\mathbb{A}t} = \begin{bmatrix} e^{\alpha t} & -k_1^+(\alpha-\beta)^{-1}(e^{\alpha t}-e^{\beta t}) \\ 0 & e^{\beta t} \end{bmatrix}. \tag{82}$$

The matrix exponential $\mathbb{E}(t) = e^{\mathbb{A}t}$ is the unique solution to the initial value problem

$$\frac{d\mathbb{E}(t)}{dt} = \mathbb{A}\mathbb{E}(t), \quad \mathbb{E}(0) = \mathbb{I}_{2N}. \tag{83}$$

Using the fact that all of the matrices involved commute, one may show that our guess satisfies these equations. All that remains is evaluating the product in the integrand and computing the integral. This is greatly facilitated by the fact that all matrices involved commute and are invertible. The final result for the steady state covariance matrix is

$$\mathcal{C} = \begin{bmatrix} -\frac{1}{2}\alpha^{-1}[\alpha' - 2(k_1^+)^2\overline{\ell}(\alpha+\beta)^{-1}] & -k_1^+\overline{\ell}(\alpha+\beta)^{-1} \\ -k_1^+\overline{\ell}(\alpha+\beta)^{-1} & \overline{\ell}\mathbb{I}_N \end{bmatrix}. \tag{84}$$

Note that $\mathcal{C}_{\vec{\delta x},\vec{\delta \ell}} = \mathcal{C}_{\vec{\delta \ell},\vec{\delta x}} = \mathcal{C}^T_{\vec{\delta x},\vec{\delta \ell}}$, this is a manifestation of translational invariance. With the full covariance matrix, we may compute the steady state mutual information between any pair of combinations of the variables.

E. Mutual Information for Multiple Sites

Now that we are interested in a single cell's readout, we can start reducing the covariance matrix. We only want to track a single cell, say the cell at site 0, so we only need one diagonal entry from $\mathcal{C}_{\vec{\delta x},\vec{\delta x}}$. If $\mathbb{M}$ is a matrix with a constant diagonal, then

$$\mathbb{M}_{0,0} = \frac{1}{N}\sum_{j=0}^{N-1}\lambda_{\mathbb{M}}(j). \tag{85}$$

If we assume that the ligand timescales are slow, we have

$$\sigma_x^2 = -\frac{1}{2N}\sum_{j=0}^{N-1}\left[\frac{\lambda_{\alpha'}(j)}{\lambda_\alpha(j)} - \frac{2(k_1^+)^2\overline{\ell}}{\lambda_\alpha(j)^2}\right], \tag{86}$$

where the eigenvalues are

$$\begin{aligned}\lambda_\alpha(j) &= -c - 2\gamma\left[1 - \cos(2\pi j/N)\right], \\ \lambda_{\alpha'}(j) &= 2d(x_c) + 4\gamma x_c\left[1 - \cos(2\pi j/N)\right].\end{aligned} \tag{87}$$

The first term describes the intrinsic noise, while the second describes the extrinsic noise. We can evaluate the sum approximately in the large N limit by adding and subtracting a $j = N$ term and using the Euler-Maclaurin formula [4]. The formula states that, for a smooth f, we have

$$\begin{aligned}\sum_{j=0}^{n} f(j) = \int_0^n f(t)dt + \frac{f(n) + f(0)}{2} \\ + \sum_{j=1}^{k} \frac{(-1)^{j+1} B_{j+1}}{(j+1)!}[f^{(j)}(n) - f^{(j)}(0)] + R_k,\end{aligned} \tag{88}$$

where the remainder term is

$$R_k = \frac{(-1)^k}{(k+1)!} \int_0^n f^{(k+1)}(t) P_{k+1}(t) dt, \tag{89}$$

the Bernoulli numbers are denoted by the B_k, and $P_k(t) = B_k(t - \lfloor t \rfloor)$ denotes the periodic Bernoulli functions. With the sum extended to N, there is tremendous simplification, as $f^{(k)}(N) = f^{(k)}(0)$. We had to add and subtract the $j = N$ term; the added term gets taken into the integral, while the subtracted term is canceled by the average of the two endpoints. To evaluate the integrals, it is best to work with the angular variables $\phi = 2\pi t/N$, which ranges over $[0, 2\pi]$. The remainder term becomes smaller as N increases; the terms in the Fourier series for the periodic Bernoulli functions have arguments of the form $mN\phi$, where m is a non-zero integer. Neglecting the remainder term, we find

$$\sigma_x^2 = \left(x_c + \frac{d(x_c) - cx_c}{\sqrt{c(c+4\gamma)}}\right) + \frac{(k_1^+)^2 \overline{\ell}(c+2\gamma)}{(c(c+4\gamma))^{3/2}}, \tag{90}$$

where the first pair describes intrinsic noise and the last term describes extrinsic noise. Generally speaking, this continuum approximation will break down on some neighborhood of the critical point. For example, the sum for the variance diverges like θ^{-2} as we approach the critical point, but the result of the integral diverges like $\theta^{-3/2}$. Nonetheless, the two results agree well numerically on all but a small neighborhood of the critical point, and the results still diverge, so we expect it to give reasonably accurate results.

1. Mutual Information with the On-site Ligand

We will start with the on-site mutual information. The variance of each ligand molecules is $\overline{\ell}$, so it suffices to compute the covariance between the ligand and readout. In the slow ligand and continuum limits, this is

$$\left\langle (\delta x_0)(\delta \ell_0) \right\rangle = \frac{k_1^+ \overline{\ell}}{\sqrt{c(c+4\gamma)}}. \tag{91}$$

For a pair of Gaussian variables, the mutual information increases monotonically with the ratio $\langle (\delta x)(\delta y)\rangle^2/\sigma_x^2\sigma_y^2$. When expressed in terms of the Landau parameters and using $\theta > 0$, the derivative with respect to γ is negative. This means that the mutual information decreases with increasing communication strength.

2. Mutual Information with the Spatially Resolved Profile

We will compute the result for the spatially resolved profile. We need to reduce the covariance matrix. We do this by integrating out all but one of the readout molecules. This amounts to working with the reduced covariance matrix

$$\mathcal{C}_{\text{red}} = \begin{bmatrix} \sigma_x^2 & \hat{e}_0^T \mathcal{C}_{\vec{\delta x},\vec{\delta \ell}} \\ \mathcal{C}_{\vec{\delta x},\vec{\delta \ell}} \hat{e}_0 & \overline{\ell}\mathbb{I}_N \end{bmatrix}. \tag{92}$$

The unit vector $\hat{e}_0 = [1, 0, ..., 0]^T$ is used to extract the first row and column from the matrix describing the correlations between x and ℓ. In order to move forward, we use a result about the determinants of block matrices. Suppose that $\mathbb{M}$ takes the form

$$\mathbb{M} = \begin{bmatrix} A & B \\ C & D \end{bmatrix}, \tag{93}$$

where A and D are square matrices of potentially different sizes and D is invertible. Then we have

$$\det(\mathbb{M}) = \det(A - BD^{-1}C)\det(D). \tag{94}$$

It follows that the determinant in the numerator of the mutual information is

$$\det(\mathcal{C}_{\text{red}}) = (\sigma_x^2 - \hat{e}_0^T \mathcal{C}^2_{\vec{\delta x},\vec{\delta \ell}} \hat{e}_0/\overline{\ell})\overline{\ell}^N \tag{95}$$

and the mutual information is

$$I(\delta x_0, \vec{\delta\ell}) = -\frac{1}{2}\log\left(1 - \frac{\hat{e}_0^T \mathcal{C}^2_{\vec{\delta x},\vec{\delta\ell}} \hat{e}_0}{\overline{\ell}\sigma_x^2}\right). \tag{96}$$

The $\mathcal{C}_{\vec{\delta x},\vec{\delta\ell}}$ appearing in the numerator is circulant, as it is the inverse of a circulant matrix, so its square is also circulant. We may apply the formula derived at the beginning of the section in the slow ligand limit to get

$$\hat{e}_0^T \mathcal{C}^2_{\vec{\delta x},\vec{\delta\ell}} \hat{e}_0 = \frac{1}{N}\sum_{j=0}^{N-1}\left(\frac{k_1^+\overline{\ell}}{\lambda_\alpha(j)}\right)^2. \tag{97}$$

This is the sum that we encountered when computing the extrinsic noise multiplied by $\overline{\ell}$. It follows that the mutual information may be written in the form

$$I(\delta x_0, \vec{\delta\ell}) = \frac{1}{2}\log\left(1 + \frac{\sigma^2_{\text{ext}}}{\sigma^2_{\text{int}}}\right). \tag{98}$$

The mutual information increases monotonically with the ratio of contributions to the noise. Expressing it in terms of θ and differentiating with respect to γ, the result is negative, so communication also impairs this information.

3. Mutual Information with the Spatially Averaged Ligand

We finally turn to calculating the mutual information between a single readout and the spatial average of the ligand fluctuations. Since the ligand molecules at each site are identically and independently distributed Poisson variables with mean $\overline{\ell}$, the variance in the spatial average of the ligand is

$$\sigma_L^2 = \frac{\overline{\ell}}{N}. \tag{99}$$

We need to compute the covariance between a single cell and this average. This can be found by averaging the first row or column of the readout-ligand covariance matrix

$$\left\langle (\delta x_0)(\delta L)\right\rangle = \frac{1}{N}\hat{e}_0^T \mathcal{C}_{\vec{\delta x},\vec{\delta\ell}} \vec{1}_N, \tag{100}$$

where $\vec{1}_N$ is a N-dimensional vector whose components are all 1. This is an eigenvector of circulant matrices, so we have

$$U^\dagger \vec{1} = \sqrt{N}\hat{e}_0. \tag{101}$$

Using the unitary discrete Fourier transform to diagonalize the covariance matrix, we find that this picks off the eigenvalue with $j = 0$ that does not depend on diffusion

$$\big\langle (\delta x_0)(\delta L) \big\rangle = \frac{k_1^+ \bar{\ell}}{Nc}. \tag{102}$$

Squaring and dividing by the variance in δL, we see that this is the $j = 0$ term in the extrinsic noise. If we work with the variance as a sum of eigenvalues, the ratio of the squared covariance to the products of the noises tends to one as we approach the critical point, so the mutual information diverges there. If we use the integral approximation to the variance, this ratio can exceed one, leading to a negative argument. This approximation breaks down for small θ, but we can trust it away from a small neighborhood of the critical point. Differentiating the ratio that appears in the mutual information with respect to γ gives a positive answer, so communication helps this mutual information.

F. Information Rate for Multiple Sites

Since the mutual information between a single cell and the spatial average of the ligand fluctuations was the only case that benefited from communication, we will restrict our focus to this case. We will take a different approach than we did for a single site, as the Langevin equations are now a $2N$-dimensional coupled linear system. Using the same convention with Fourier transforms as before, the Wiener-Khinchin theorem states that

$$\mathbb{S}(\omega) = \frac{1}{2\pi} \int_{-\infty}^{\infty} \mathcal{C}(\tau) e^{-i\omega\tau} d\tau, \tag{103}$$

where $\mathcal{C}(\tau)$ is the steady state correlation matrix. To capture the steady state correlations, we initialize the system at $t_0 = -\infty$. Since our variables have zero mean, this takes the form

$$\mathcal{C}(\tau) = \big\langle \vec{Y}_{t+\tau} \vec{Y}_t^T \big\rangle. \tag{104}$$

Since we initialized this at $t_0 = -\infty$, this doesn't depend on the choice of t. When $\tau = 0$, this reduces to the covariance matrix $\mathcal{C}$ that we worked with before. Using the Itô isometry and performing a change of variables to $t' = t - s$, one may show that

$$\mathcal{C}(\tau) = \int_{-\min(0,\tau)}^{\infty} e^{\mathbb{A}(t+\tau)} \mathbb{B}\mathbb{B}^T (e^{\mathbb{A}t})^T dt. \tag{105}$$

When $\tau \geq 0$, we may factor off $e^{\mathbb{A}\tau}$ to the left, and the remaining integral becomes $\mathcal{C}$. For $\tau < 0$, we perform a change of variables to $t' = t + \tau$, then factoring off $e^{-\mathbb{A}^T\tau}$ to the right gives the integral that yields $\mathcal{C}$. In summary, we have

$$\mathcal{C}(\tau) = \begin{cases} e^{\mathbb{A}\tau}\mathcal{C}, & \tau \geq 0, \\ \mathcal{C}(e^{-\mathbb{A}\tau})^T, & \tau < 0. \end{cases} \tag{106}$$

Using this, we find that the cross-spectrum is

$$\mathbb{S}(\omega) = -\frac{\left[(\mathbb{A} - i\omega\mathbb{I}_{2N})^{-1}\mathcal{C} + \mathcal{C}(\mathbb{A}^T + i\omega\mathbb{I}_{2N})^{-1}\right]}{2\pi}. \tag{107}$$

To evaluate this, we need to find the inverse matrix and then plug it in. Since the α, β, and $\mathbb{I}_N$ all commute and are invertible, treating them as if they were scalars leads to the guess

$$(\mathbb{A} - i\omega\mathbb{I}_{2N})^{-1} = \begin{bmatrix} (\alpha - i\omega\mathbb{I}_N)^{-1} & -k_1^+(\alpha - i\omega\mathbb{I}_N)^{-1}(\beta - i\omega\mathbb{I}_N)^{-1} \\ 0 & (\beta - i\omega\mathbb{I}_N)^{-1} \end{bmatrix}, \tag{108}$$

and a direct computation shows that this is the inverse. Using this, we can compute the cross-spectrum

$$\begin{gathered} \mathbb{S}(\omega) = \begin{bmatrix} \mathbb{S}_{\vec{x},\vec{x}}(\omega) & \mathbb{S}_{\vec{x},\vec{\ell}}(\omega) \\ \mathbb{S}^\dagger_{\vec{x},\vec{\ell}}(\omega) & \mathbb{S}_{\vec{\ell},\vec{\ell}}(\omega) \end{bmatrix}, \\ \mathbb{S}_{\vec{x},\vec{x}}(\omega) = -\frac{1}{2\pi}(\alpha^2 + \omega^2\mathbb{I}_N)^{-1}[-\alpha' + 2(k_1^+)^2\overline{\ell}\beta(\beta^2 + \omega^2\mathbb{I}_N)^{-1}], \\ \mathbb{S}_{\vec{x},\vec{\ell}}(\omega) = \frac{1}{\pi}k_1^+\overline{\ell}\beta(\beta^2 + \omega^2\mathbb{I}_N)^{-1}(\alpha - i\omega\mathbb{I}_N)^{-1}, \qquad \mathbb{S}_{\vec{\ell},\vec{\ell}}(\omega) = -\frac{1}{\pi}\overline{\ell}\beta(\beta^2 + \omega^2\mathbb{I}_N)^{-1} \end{gathered} \tag{109}$$

Now we need to compute the relevant terms from these matrices.

First, we compute the power spectrum for the fluctuations in δx_0. Since all of the matrices involved here are circulant, any diagonal element is the average of the eigenvalues

$$S_{\delta x_0,\delta x_0}(\omega) = -\frac{1}{2\pi N}\sum_{j=0}^{N-1}\left[\frac{-\lambda_{\alpha'}(j)}{\lambda_\alpha(j)^2+\omega^2} + \frac{2(k_1^+)^2\overline{\ell}\lambda_\beta(j)}{(\lambda_\alpha(j)^2+\omega^2)(\lambda_\beta(j)^2+\omega^2)}\right], \tag{110}$$

where the eigenvalues of β are

$$\lambda_\beta(j) = -k_\ell^- - 2\gamma'(1-\cos(2\pi j/N)). \tag{111}$$

It is possible to approximate this as an integral and evaluate the integral analytically. However, the result is complicated and appears in an integral as part of a logarithm's argument. We cannot make progress with the final integral, so we will evaluate this numerically.

One may show that the power spectrum in δL is the average of all of the matrix elements in the cross-spectrum $\mathbb{S}_{\vec{\delta\ell},\vec{\delta\ell}}$ by using the definition of δL and Eq. 60. We can write this compactly using the vector of ones

$$S_{\delta L,\delta L}(\omega) = \frac{1}{N^2}\vec{1}_N^T\mathbb{S}_{\vec{\delta\ell},\vec{\delta\ell}}\vec{1}_N. \tag{112}$$

Since $\mathbb{S}_{\vec{\delta\ell},\vec{\delta\ell}}$ is circulant, the vector of ones is an eigenvector of the matrix with $j=0$, so we have

$$S_{\delta L,\delta L}(\omega) = \frac{\overline{\ell}k_\ell^-}{\pi N[(k_\ell^-)^2+\omega^2]}. \tag{113}$$

Finally, we compute the cross-spectrum between δx_0 and δL. This should be the average of the elements in the first row in $\mathbb{S}_{\vec{\delta x},\vec{\delta\ell}}$, which may be obtained via

$$S_{\delta x_0,\delta L}(\omega) = \frac{1}{N}\hat{e}_0^T\mathbb{S}_{\vec{\delta x},\vec{\delta\ell}}\vec{1}_N. \tag{114}$$

The vector of ones is also an eigenvector of this matrix with $j=0$, so

$$S_{\delta x_0,\delta L}(\omega) = \frac{k_1^+k_\ell^-\overline{\ell}}{\pi N[(k_\ell^-)^2+\omega^2][c+i\omega]}. \tag{115}$$

With the power spectra and cross-spectrum, we can numerically integrate Eq. 59. A detailed description of how this depends on all of the parameters is provided in the main text.

Appendix B Supplement for "Precision of Flow Sensing by Self-Communicating Cells"

A. Derivation of the Zeroth-Order Solution

In this section, we derive the lowest order terms in the expansion for the inner and outer solution (Eq. 19). We recall the non-dimensionalized variables and parameters

$$\begin{aligned} \chi = \bar{c}a^3, \qquad \rho = \frac{r}{a}, \qquad \tilde{\beta} = \frac{\beta a^4}{D}, \\ \tilde{\alpha} = \frac{\alpha a}{D}, \qquad \epsilon = \frac{v_0 a}{D}, \qquad \kappa = \frac{\sqrt{\mathcal{K}}}{a}. \end{aligned} \tag{116}$$

It will be convenient to describe the flow profile with the functions

$$\begin{aligned} u_r(\rho) &= 1 - \frac{1+3\kappa+3\kappa^2}{\rho^3} + \frac{3\kappa}{\rho^2}\left(1+\frac{\kappa}{\rho}\right)e^{\frac{1-\rho}{\kappa}}, \\ u_\theta(\rho) &= 1 + \frac{1+3\kappa+3\kappa^2}{2\rho^3} - \frac{3}{2\rho}\left(1+\frac{\kappa}{\rho}+\frac{\kappa^2}{\rho^2}\right)e^{\frac{1-\rho}{\kappa}} \end{aligned} \tag{117}$$

With these, the dimensionless flow profile (Eq. 16) is

$$\vec{u}(\rho,\theta) = \frac{\vec{v}(\rho,\theta)}{v_0} = u_r(\rho)\cos\theta\hat{\rho} - u_\theta(\rho)\sin\theta\hat{\theta}. \tag{118}$$

We solve the drift-diffusion equation (Eq. 17) with these flow lines through the method of matched asymptotic expansions. To do this, we introduce two expansions: an inner and an outer one. The inner one satisfies the boundary condition at the cell surface, while the outer one satisfies the condition at infinity. We obtain the full solution and remaining coefficients by matching the functional forms on a common overlap region: $s = \epsilon\rho \to 0$ for the outer expansion and $\rho \to \infty$ for the inner expansion.

We assume that the inner expansion has the standard form

$$\chi(\rho,\theta,\epsilon) = \sum_{n=0}^{\infty} \epsilon^n \chi_n(\rho,\theta). \tag{119}$$

This is a solution to the problem

$$0 = \nabla_\rho^2\chi(\rho,\theta) - \epsilon\vec{u}(\rho,\theta)\cdot\nabla_\rho\chi(\rho,\theta), \quad -\frac{\partial\chi(\rho,\theta)}{\partial\rho}\Big|_{\rho=1} = \tilde{\beta} - \tilde{\alpha}\chi(1,\theta), \tag{120}$$

where χ's ϵ dependence has been suppressed. Collecting powers of ϵ, the equations for χ_n become

$$0 = \nabla_\rho^2 \chi_n - \vec{u} \cdot \nabla_\rho \chi_{n-1}, \qquad -\frac{\partial \chi_n}{\partial \rho}\Big|_{\rho=1} = \tilde{\beta}\delta_{n,0} - \tilde{\alpha}\chi_n(1). \tag{121}$$

This assumes that the flow is small, which is valid close to the surface of the cell.

For the outer expansion, we introduce the re-scaled distance

$$s = \epsilon\rho. \tag{122}$$

We make the standard choice

$$X(s, \theta, \epsilon) = \sum_{n=0}^{\infty} F_n(\epsilon) X_n(s, \theta), \tag{123}$$

where

$$\lim_{\epsilon \to 0} \frac{F_{n+1}(\epsilon)}{F_n(\epsilon)} = 0. \tag{124}$$

In the derivation of Eq. 20 (next section), we will show that using only the lowest order term $F_0(\epsilon)X_0(s, \theta)$ gives a consistent solution sufficient for our purposes. The full expansion solves the problem

$$0 = \nabla_s^2 X(s, \theta) - \vec{u}\left(\frac{s}{\epsilon}, \theta\right) \cdot \nabla_s X(s, \theta), \quad \lim_{s \to \infty} X_n(s, \theta) = 0. \tag{125}$$

For the outer expansion, we neglect the exponential terms in $\vec{u}$, as these have $-s/\epsilon$ in the exponent, which is smaller than any power of ϵ and cannot be captured by a Taylor series. This means that we work with

$$u_r\left(\frac{s}{\epsilon}\right) \sim 1 - \frac{\zeta\epsilon^3}{s^3}, \qquad u_\theta\left(\frac{s}{\epsilon}\right) \sim 1 + \frac{2\zeta\epsilon^3}{s^3}, \tag{126}$$

where $\zeta = 1 + 3\kappa + 3\kappa^2$. For the lowest order terms (order $0-2$), only the constant terms in the $\vec{u}$ affect the PDE, and the flow is just the flow at infinity, $\hat{z}$.

1. Inner Expansion

For the zero-order term, we have

$$\nabla_\rho^2 \chi_0 = 0, \qquad -\left.\frac{\partial \chi_0}{\partial \rho}\right|_{\rho=1} = \tilde{\beta} - \tilde{\alpha}\chi_0(1). \tag{127}$$

Using azimuthal symmetry, the general solution to the PDE is

$$\chi_0 = \sum_{\ell=0}^{\infty} \left(A_{0,\ell}\rho^\ell + \frac{B_{0,\ell}}{\rho^{\ell+1}} \right) Y_\ell^0(\theta), \tag{128}$$

where $A_{0,\ell}$ and $B_{0,\ell}$ are undetermined coefficients, and Y_ℓ^m are spherical harmonics. We plug this into the boundary condition in Eq. 127. Since the spherical harmonics are linearly independent, we have the system

$$-(\ell A_{0,\ell} - (\ell+1)B_{0,\ell}) = \sqrt{4\pi}\tilde{\beta}\delta_{0,\ell} - \tilde{\alpha}(A_{0,\ell} + B_{0,\ell}), \tag{129}$$

where the factor of $\sqrt{4\pi}$ arises from $Y_0^0 = (4\pi)^{-1/2}$ and factoring off a spherical harmonic from both sides of the equation. We will use this result shortly, as it will simplify substantially after using the matching condition.

2. Outer Expansion

The equation for X_0 follows from Eq. 125,

$$0 = \nabla_s^2 X_0 - \cos\theta \frac{\partial X_0}{\partial s} + \frac{\sin\theta}{s}\frac{\partial X_0}{\partial \theta}, \tag{130}$$

where as discussed we use $\vec{u} = \hat{z}$ and we have written the gradient in spherical coordinates. We can eliminate the θ-dependence and replace it with a $\cos\theta$-dependence using

$$\sin\theta \frac{\partial}{\partial\theta} = -(1-\cos^2\theta)\frac{\partial}{\partial(\cos\theta)}, \tag{131}$$

with which Eq. 130 becomes

$$0 = \nabla_s^2 X_0 - \cos\theta \frac{\partial X_0}{\partial s} - \frac{(1-\cos^2\theta)}{s}\frac{\partial X_0}{\partial(\cos\theta)}. \tag{132}$$

If we make the subsitution $X_0(s,\theta) = G(s,\theta)\exp(s\cos(\theta)/2)$, the equation simplifies because the operator becomes

$$\nabla_s^2 X_0 - \cos\theta\frac{\partial X_0}{\partial s} - \frac{(1-\cos^2\theta)}{s}\frac{\partial X_0}{\partial(\cos\theta)} = e^{\frac{s}{2}\cos\theta}\left[\nabla_s^2 - \frac{1}{4}\right]G(s,\theta). \tag{133}$$

Since the exponential factor never vanishes, the PDE becomes

$$\nabla_s^2 G(s,\theta) - \frac{1}{4}G(s,\theta) = 0. \tag{134}$$

To move forward, we write G as a linear combination of spherical harmonics and use azimuthal symmetry

$$G(s,\theta) = \sum_{\ell=0}^{\infty}\frac{H_\ell(s/2)}{\sqrt{s}}Y_\ell^0(\theta), \tag{135}$$

where the H_ℓ are to be determined. Substitution and isolating the independent spherical harmonics give the ODEs

$$0 = s^{-5/2}\left[\left(\frac{s}{2}\right)^2\frac{d^2H_\ell(\frac{s}{2})}{d(\frac{s}{2})^2} + \frac{s}{2}\frac{dH_\ell(\frac{s}{2})}{d(\frac{s}{2})} - \left(\left(\frac{s}{2}\right)^2 + \left(\ell+\frac{1}{2}\right)^2\right)H_\ell\left(\frac{s}{2}\right)\right]. \tag{136}$$

The term in square brackets must vanish, and this is just the modified Bessel differential equation in $s/2$ of order $\ell + 1/2$. This means that the general solution for H_ℓ is

$$H_\ell(s/2) = C_{0,\ell}K_{\ell+1/2}(s/2) + D_{0,\ell}I_{\ell+1/2}(s/2), \tag{137}$$

where the Is and Ks are modified Bessel functions of the first and second kind, respectively, and $C_{0,\ell}$ and $D_{0,\ell}$ are undetermined coefficients. Substituting this back into X gives

$$X_0(s,\theta) = \frac{e^{\frac{s}{2}\cos\theta}}{\sqrt{s}}\sum_{\ell=0}^{\infty}\left[C_{0,\ell}K_{\ell+1/2}(s/2) + D_{0,\ell}I_{\ell+1/2}(s/2)\right]Y_\ell^0(\theta). \tag{138}$$

Since X_0 must vanish at infinity, we must have $D_{0,\ell} = 0$ for all ℓ so

$$X_0(s,\theta) = \frac{e^{\frac{s}{2}\cos\theta}}{\sqrt{s}}\sum_{\ell=0}^{\infty}C_{0,\ell}K_{\ell+1/2}(s/2)Y_\ell^0(\theta). \tag{139}$$

For positive half-integer orders, the Bessel Ks are exponentially decaying functions with decaying power laws. The exponentially decaying factor is $\exp(-s/2)$, so the combination of the two exponentials is decreasing for all θ values except $\theta = 0$, where the factor is constant.

3. Asymptotic Matching

Now we match the functional forms of the two solutions. We look at the inner expansion first (Eq. 128). Each term in the outer expansion decreases as s increases, so we cannot have the positive powers of ρ in the inner expansion. This implies that $A_{0,\ell} = 0$ for $\ell \geq 1$. Since $\tilde{\alpha} \geq 0$, applying the surface boundary condition in Eq. 129 also gives $B_{0,\ell} = 0$ for $\ell \geq 1$. This means that, to lowest order in ϵ

$$\chi_0 = Y_0^0 \left(A_{0,0} + \frac{B_{0,0}}{\rho} \right). \tag{140}$$

Now we turn to the outer expansion. Note that the modified Bessel functions of the second kind K have the following asymptotics

$$K_{\ell+1/2}(s/2) = \mathcal{O}(s^{-(\ell+1/2)}), \qquad s \to 0. \tag{141}$$

Including the overall factor of $s^{-1/2}$, we see that the ℓ term diverges like $s^{-\ell-1}$. This means that all terms with $\ell > 0$ diverge faster than the inner solution, so the coefficients for these terms must be zero, because they cannot be matched. This means

$$X_0(s,\theta) = \frac{e^{\frac{s}{2}\cos\theta}}{\sqrt{s}} C_{0,0} K_{1/2}(s/2) Y_0^0 = \sqrt{\pi} C_{0,0} \frac{e^{\frac{s}{2}(\cos\theta - 1)}}{s} Y_0^0. \tag{142}$$

and therefore to lowest order in ϵ we have

$$X = F_0(\epsilon) \sqrt{\pi} C_{0,0} \frac{e^{\frac{s}{2}(\cos\theta - 1)}}{s} Y_0^0. \tag{143}$$

So far, we have used matching to argue which terms should vanish. Now we will find the values for the non-zero coefficients. To do this, we recognize that because $s = \epsilon\rho$ in Eq. 143, in order to match this with Eq. 140 in powers of ϵ, we must take

$$F_0(\epsilon) = \epsilon, \qquad A_{0,0} = 0. \tag{144}$$

Using the boundary condition at the surface from Eq. 129 gives

$$B_{0,0} = \sqrt{4\pi} \frac{\tilde{\beta}}{1 + \tilde{\alpha}} = \sqrt{4\pi}\gamma, \tag{145}$$

where we define $\gamma = \tilde{\beta}/(1+\tilde{\alpha})$. Matching Eq. 143 to the ρ^{-1} term in Eq. 140 then gives

$$C_{0,0} = 2\gamma. \tag{146}$$

Using the values determined in this section, Eqs. 140 and 143 become

$$\chi_0 = \frac{\gamma}{\rho}, \qquad X = \frac{\epsilon\gamma}{s} e^{-s(1-\cos\theta)/2}, \tag{147}$$

as in Eq. 19.

B. Derivation of the First-Order Solution

In this section, we will calculate the first-order term in the inner expansion and show that we just need the lowest order term in the outer expansion.

1. Inner Expansion

The first-order term in the inner expansion solves the PDE

$$0 = \nabla_\rho^2 \chi_1 - \vec{u} \cdot \nabla_\rho \chi_0, \qquad -\left.\frac{\partial \chi_1}{\partial \rho}\right|_{\rho=1} = -\tilde{\alpha}\chi_1(1). \tag{148}$$

Using the zero-order solution χ_0 gives

$$\nabla_\rho^2 \chi_1 = \vec{u} \cdot \nabla_\rho \chi_0 = u_r(\rho)\cos(\theta)\left(-\frac{\gamma}{\rho^2}\right) = -\sqrt{\frac{4\pi}{3}}\frac{\gamma}{\rho^2} u_r(\rho) Y_1^0(\theta). \tag{149}$$

The general solution to this is the solution to the homogeneous equation (Laplace's equation) plus an inhomogeneous term arising from the presence of a source (the particular solution). We proceed by using the Green's function for Laplace's equation

$$\nabla_\rho G(\vec{\rho}, \vec{\rho}\,') = \delta^3(\vec{\rho} - \vec{\rho}\,') \Longrightarrow G(\vec{\rho}, \vec{\rho}\,') = -\frac{1}{4\pi|\vec{\rho} - \vec{\rho}\,'|}. \tag{150}$$

The particular solution is the convolution of this with the source term,

$$\chi_1(\vec{\rho}) = \int_{\rho' \geq 1} d^3\rho' G(\vec{\rho}, \vec{\rho}') \left(-\sqrt{\frac{4\pi}{3}}\frac{\gamma}{\rho'^2} u_r(\rho') Y_1^0(\theta')\right). \tag{151}$$

We expand the Green's function in terms of Legendre polynomials P_ℓ

$$\frac{1}{|\vec{\rho}-\vec{\rho}\,'|} = \frac{1}{\rho_>}\sum_{\ell=0}^{\infty}\left(\frac{\rho_<}{\rho_>}\right)^{\ell} P_\ell(\hat{\rho}\cdot\hat{\rho}'), \tag{152}$$

where $\rho_< = \min(\rho,\rho')$ and $\rho_> = \max(\rho,\rho')$. The Legendre polynomials are related to the spherical harmonics via

$$P_\ell(\hat{\rho}\cdot\hat{\rho}') = \frac{4\pi}{2\ell+1}\sum_{m=-\ell}^{\ell} Y_\ell^m(\hat{\rho})Y_\ell^m(\hat{\rho}')^*. \tag{153}$$

By orthogonality, only the term with $\ell = 1$ and $m = 0$ will make a non-vanishing contribution to the convolution. To evaluate the convolution, we use the orthogonality of spherical harmonics to simplify the angular integrals and break the integral over ρ' into regions where $\rho' < \rho$ and $\rho' > \rho$. Specifically, combining Eqs. 150-153 allows the angular portion of the integral to be easily performed,

$$\begin{aligned}\chi_1(\vec{\rho}) &= \int_{\rho'\geq 1} d^3\rho' \left(\sum_{\ell,m}\frac{\rho_<^\ell}{\rho_>^{\ell+1}(2\ell+1)}Y_\ell^m(\hat{\rho})\,Y_\ell^{m*}(\hat{\rho}')\right)\left(\sqrt{\frac{4\pi}{3}}\frac{\gamma}{\rho'^2}u_r(\rho')\,Y_1^0(\theta')\right)\\ &= \frac{\gamma}{3}\sqrt{\frac{4\pi}{3}}Y_1^0(\theta)\left[\int_1^\rho d\rho'\frac{\rho'}{\rho^2}u_r(\rho') + \int_\rho^\infty d\rho'\frac{\rho}{\rho'^2}u_r(\rho')\right].\end{aligned} \tag{154}$$

Inserting the expression for u_r (Eq. 117) with $\zeta = 1+3\kappa+3\kappa^2$ into Eq. 154 then yields

$$\begin{aligned}\chi_1(\vec{\rho}) &= \frac{\gamma}{3}\sqrt{\frac{4\pi}{3}}Y_1^0(\theta)\left[\int_1^\rho d\rho'\frac{\rho'}{\rho^2}\left(1-\frac{\zeta}{\rho'^3}+\frac{3\kappa}{\rho'^2}\left(1+\frac{\kappa}{\rho'}\right)e^{\frac{1-\rho'}{\kappa}}\right)\right.\\ &\qquad\left.+\int_\rho^\infty d\rho'\frac{\rho}{\rho'^2}\left(1-\frac{\zeta}{\rho'^3}+\frac{3\kappa}{\rho'^2}\left(1+\frac{\kappa}{\rho'}\right)e^{\frac{1-\rho'}{\kappa}}\right)\right]\\ &= \frac{\gamma}{3}\sqrt{\frac{4\pi}{3}}Y_1^0(\theta)\left[\frac{3}{2}-\frac{2\zeta+1}{2\rho^2}+\frac{3\zeta}{4\rho^3}+\int_1^\infty d\rho'\frac{3\kappa}{\rho^2\rho'}\left(1+\frac{\kappa}{\rho'}\right)e^{\frac{1-\rho'}{\kappa}}\right.\\ &\qquad\left.+\int_\rho^\infty d\rho'\frac{3\kappa}{\rho'^2}\left(\frac{\rho}{\rho'^2}-\frac{\rho'}{\rho^2}\right)\left(1+\frac{\kappa}{\rho'}\right)e^{\frac{1-\rho'}{\kappa}}\right]\\ &= \frac{\gamma}{2}\sqrt{\frac{4\pi}{3}}Y_1^0(\theta)\left[1-\frac{2\zeta+1}{3\rho^2}+\frac{\zeta}{2\rho^3}+\frac{2\kappa}{\rho^2}e^{\frac{1}{\kappa}}\left(E_1\left(\frac{1}{\kappa}\right)+\kappa E_2\left(\frac{1}{\kappa}\right)\right)\right.\\ &\qquad\left.+\frac{2\kappa}{\rho^2}e^{\frac{1}{\kappa}}\left(E_4\left(\frac{\rho}{\kappa}\right)-E_1\left(\frac{\rho}{\kappa}\right)+\frac{\kappa}{\rho}E_5\left(\frac{\rho}{\kappa}\right)-\frac{\kappa}{\rho}E_2\left(\frac{\rho}{\kappa}\right)\right)\right],\end{aligned} \tag{155}$$

where

$$E_n(x) = \int_1^\infty dt\frac{e^{-tx}}{t^n}. \tag{156}$$

Eq. 155 can be simplified slightly using the recursion relation

$$E_n(x) = \frac{1}{n-1}\left(e^{-x} - xE_{n-1}(x)\right), \tag{157}$$

which is valid for $x > 0$. For integer values of $n > 1$, this relation can be repeated to produce

$$E_n(x) = \frac{1}{(n-1)!}\left[(-x)^{n-1}E_1(x) + e^{-x}\sum_{i=0}^{n-2}\left((n-2-i)!\right)(-x)^i\right]. \tag{158}$$

Applying these relations to the E_n functions seen in Eq. 155 allows for the simplifications

$$\begin{aligned} E_1\left(\frac{1}{\kappa}\right) + \kappa E_2\left(\frac{1}{\kappa}\right) &= E_1\left(\frac{1}{\kappa}\right) + \kappa\left(e^{-\frac{1}{\kappa}} - \frac{1}{\kappa}E_1\left(\frac{1}{\kappa}\right)\right) \\ &= \kappa e^{-\frac{1}{\kappa}}, \end{aligned} \tag{159}$$

and

$$\begin{aligned} E_4\left(\frac{\rho}{\kappa}\right) - E_1\left(\frac{\rho}{\kappa}\right) + \frac{\kappa}{\rho}E_5\left(\frac{\rho}{\kappa}\right) - \frac{\kappa}{\rho}E_2\left(\frac{\rho}{\kappa}\right) &= \frac{1}{6}\left(\left(2 - \frac{\rho}{\kappa} + \frac{\rho^2}{\kappa^2}\right)e^{-\frac{\rho}{\kappa}} - \frac{\rho^3}{\kappa^3}E_1\left(\frac{\rho}{\kappa}\right)\right) \\ &\quad - E_1\left(\frac{\rho}{\kappa}\right) - \frac{\kappa}{\rho}\left(e^{-\frac{\rho}{\kappa}} - \frac{\rho}{\kappa}E_1\left(\frac{\rho}{\kappa}\right)\right) \\ &\quad + \frac{\kappa}{24\rho}\left(\left(6 - \frac{2\rho}{\kappa} + \frac{\rho^2}{\kappa^2} - \frac{\rho^3}{\kappa^3}\right)e^{-\frac{\rho}{\kappa}} + \frac{\rho^4}{\kappa^4}E_1\left(\frac{\rho}{\kappa}\right)\right) \\ &= \frac{\kappa}{8\rho}\left(\frac{\rho^3}{\kappa^3} - \frac{\rho^2}{\kappa^2} + \frac{2\rho}{\kappa} - 6\right)e^{-\frac{\rho}{\kappa}} - \frac{\rho^3}{8\kappa^3}E_1\left(\frac{\rho}{\kappa}\right). \end{aligned} \tag{160}$$

Inserting Eqs. 159 and 160 into Eq. 155 and adding in the general solution to Laplace's equation then yields

$$\begin{aligned} \chi_1 = \frac{\gamma}{2}\sqrt{\frac{4\pi}{3}}Y_1^0\Bigg[&\frac{\kappa^2}{4\rho^3}e^{1/\kappa}\left(\left(\frac{\rho^3}{\kappa^3} - \frac{\rho^2}{\kappa^2} + \frac{2\rho}{\kappa} - 6\right)e^{-\rho/\kappa} - \frac{\rho^4}{\kappa^4}E_1\left(\frac{\rho}{\kappa}\right)\right) \\ &+1 - \frac{2\kappa+1}{\rho^2} + \frac{1+3\kappa+3\kappa^2}{2\rho^3}\Bigg] + \gamma\sum_{\ell\geq 0}\left(A_{1,\ell}\rho^\ell + \frac{B_{1,\ell}}{\rho^{\ell+1}}\right)Y_\ell^0. \end{aligned} \tag{161}$$

It will be convenient to introduce a constant

$$w = 1 + \kappa^{-1} + \kappa^{-2}e^{1/\kappa}E_1(\kappa^{-1}). \tag{162}$$

The boundary condition from Eq. 148 translates to

$$\sqrt{\frac{4\pi}{3}}\frac{w}{8}\delta_{\ell,1} + \ell A_{1,\ell} - (\ell+1)B_{1,\ell} = \tilde{\alpha}\left[\sqrt{\frac{4\pi}{3}}\frac{w}{8}\delta_{\ell,1} + A_{1,\ell} + B_{1,\ell}\right]. \tag{163}$$

2. Asymptotic Matching

We attempt to match the first-order solution for χ to the lowest order solution for X. We will see that this leads to a consistent matching condition, confirming that we may only work with the lowest order term in X.

As before, none of the terms in X diverges at large s, so we need $A_{1,\ell} = 0$ for $\ell \geq 1$. The boundary condition for the surface for χ_1 in Eq. 163 implies that $B_{1,\ell} = 0$ for $\ell \geq 2$. Because $A_{1,1} = 0$, we set $\ell = 1$ in Eq. 163 to find

$$B_{1,1} = \frac{w}{8}\sqrt{\frac{4\pi}{3}}\frac{1-\tilde{\alpha}}{2+\tilde{\alpha}}. \tag{164}$$

We expand X (Eq. 19 with $s = \epsilon\rho$) to first order in ϵ, giving

$$X = \sqrt{4\pi}\frac{\gamma}{\rho}Y_0^0 + \frac{\epsilon\gamma}{2}\left(\sqrt{\frac{4\pi}{3}}Y_1^0 - \sqrt{4\pi}Y_0^0\right), \tag{165}$$

where again we have used $Y_1^0 = \sqrt{4\pi/3}\cos\theta$. Our form for $B_{1,1}$ is fine, since there is no term in X proportional to ρ^{-2} to this order and we are matching the large ρ behavior of χ to X. Since the $\mathcal{O}(\epsilon^0)$ term in X was matched by χ_0, we must match $\epsilon\chi_1$ to the $\mathcal{O}(\epsilon)$ term in X. The Y_1^0 term in X must be matched by the inhomogeneous term in χ_1, as the terms in the homogeneous solution do not have a constant times Y_1^0. Specifically, we need the bracketed term in Eq. 161 to tend to 1 as $\rho \to \infty$. We have no parameters to tune, so if this fails, we will have to go to higher order. However, the limit is one, so this is consistent. We find $A_{1,0}$ from matching to the last term in X,

$$A_{1,0} = -\sqrt{\pi}. \tag{166}$$

Solving for $B_{1,0}$ using the boundary condition at the surface gives

$$B_{1,0} = \frac{\tilde{\alpha}\sqrt{\pi}}{1+\tilde{\alpha}}. \tag{167}$$

These matching conditions are consistently satisfied, confirming that we may only work with the lowest order term in X. Using the values of the coefficients and the spherical harmonics to simplify Eq. 161 gives

$$\chi_1 = \frac{\gamma}{2}\left\{\frac{\tilde{\alpha}}{(1+\tilde{\alpha})\rho} - 1 + \frac{\cos\theta}{4}\left[\frac{(1-\tilde{\alpha})w}{(2+\tilde{\alpha})\rho^2} + f(\rho,\kappa)\right]\right\}, \tag{168}$$

as in Eq. 20, where the auxiliary function is

$$f(\rho,\kappa) = 4 - \frac{4(2\kappa+1)}{\rho^2} + \frac{2(1+3\kappa+3\kappa^2)}{\rho^3} + \frac{\kappa^2 e^{1/\kappa}}{\rho^3}\left[\left(\frac{\rho^3}{\kappa^3} - \frac{\rho^2}{\kappa^2} + \frac{2\rho}{\kappa} - 6\right)e^{-\rho/\kappa} - \frac{\rho^4 E_1(\rho/\kappa)}{\kappa^4}\right]. \tag{169}$$

Note that $f(1,\kappa) = w$.

C. Derivation of Anisotropy Mean

The anisotropy in the absorption case (Eq. 21) is

$$A \equiv \frac{\int_0^T dt \int a^2 d\Omega\ \alpha c(a,\theta,\phi,t)\cos\theta}{T\int a^2 d\Omega'\ \alpha\bar{c}(a,\theta')}. \tag{170}$$

The mean of this expression is

$$\overline{A} = \frac{\int d\Omega\ \bar{c}(a,\theta)\cos\theta}{\int d\Omega'\ \bar{c}(a,\theta')}, \tag{171}$$

where we have canceled the T, α, and a^2. We evaluate these integrals using $\bar{c}(a,\theta) = [\chi_0(1,\theta) + \epsilon\chi_1(1,\theta)]/a^3$, where χ_0 and χ_1 are given by Eqs. 19 and 20, respectively. In the numerator of Eq. 171, the χ_0 term vanishes because $\cos\theta$ integrates to zero. For the same reason, the only non-vanishing part of the χ_1 term is the $\cos\theta$ term in Eq. 20, as the integral of $\cos^2\theta$ is nonzero. Here we also recall that $f(1,\kappa) = w$. In the denominator of Eq. 171, the χ_0 term is nonzero, and therefore we do not need the χ_1 term to leading order. Altogether, Eq. 171 evaluates to

$$\overline{A} = \frac{w\epsilon}{8(2+\tilde{\alpha})}, \tag{172}$$

as in Eq. 22.

The equivalent expression to Eq. 21 that accounts for discrete molecule arrival, as stated in the main text, is

$$A = \frac{1}{\overline{\overline{N}}}\sum_{i=1}^{N}\cos\theta_i, \tag{173}$$

where θ_i is the arrival angle of the ith molecule, and

$$N = \int_0^T dt \int a^2 d\Omega \; \alpha c(a, \theta, \phi, t) \tag{174}$$

is the total number of molecules absorbed in time T. Here we will show that the mean of Eq. 173 also evaluates to Eq. 22. The mean of Eq. 173 is

$$\overline{A} = \frac{1}{\overline{N}} \left\langle \sum_{i=1}^{N} \cos\theta_i \right\rangle, \tag{175}$$

where the overbar and angle brackets are used interchangeably. Because the N absorption events are statistically independent, the angle-bracketed term in Eq. 175 simply amounts to $\overline{N}$ copies of $\langle \cos\theta \rangle$. Thus,

$$\overline{A} = \langle \cos\theta \rangle \, . \tag{176}$$

The averaging is performed over the distribution defined by the mean surface concentration $\overline{c}(a, \theta)$. Explicitly,

$$\overline{A} = \frac{\int d\Omega \; \overline{c}(a, \theta) \cos\theta}{\int d\Omega' \; \overline{c}(a, \theta')}. \tag{177}$$

This expression is equivalent to Eq. 171 and therefore evaluates to Eq. 22.

Note that the definition of A implicitly assumes that the cell "knows" the true direction of the flow to be $\theta = 0$. In reality this is untrue. Instead, the migration direction of the cell is a three-dimensional vector that can be decomposed into three components along the $\hat{x}$, $\hat{y}$, and $\hat{z}$ ($\theta = 0$) directions. However, the means of the components in the $\hat{x}$ and $\hat{y}$ directions involve averages of $\sin\theta\cos\phi$ and $\sin\theta\sin\phi$, which are zero due to the azimuthal symmetry. Therefore, the result in Eq. 22 holds even when accounting for all three components.

D. Derivation of the Anisotropy Variance

To compute the variance of Eq. 173, we use the fact that the number of molecules absorbed in a patch on the cell surface is a Poisson variable (confirmed with simulations detailed in the supplement of the publication [35]). Letting θ_i denote the value of θ at which particle i is absorbed, the second moment of the sum of cosines is

$$\left\langle \left(\sum_{i=1}^{N} \cos\theta_i \right)^2 \right\rangle = \left\langle \sum_{i=1}^{N} \cos^2\theta_i \right\rangle + \left\langle \sum_{i\neq j} \cos\theta_i \cos\theta_j \right\rangle = \langle N \rangle \langle \cos^2\theta \rangle + \langle N(N-1) \rangle \langle \cos\theta \rangle^2 , \tag{178}$$

where again the second step follows from the fact that the absorption events are statistically independent. For a Poisson random variable

$$\langle N \rangle = \sigma_N^2 = \langle N^2 \rangle - \langle N \rangle^2 \Longrightarrow \langle N(N-1) \rangle = \langle N \rangle^2 . \tag{179}$$

Inserting this result into Eq. 178, we see that the last term becomes the square of the mean and will thus cancel when using Eq. 178 to calculate the variance. Additionally, we will need to multiply the variance by a factor of three. The reason is that $\cos^2\theta$ is an even function, and therefore the angular average, to lowest order in ϵ, will be over only the uniform part of the solution (χ_0). It will therefore have the same contributions from the $\hat{x}$ and $\hat{y}$ directions. Altogether, this allows us to write the variance as

$$\sigma_A^2 = \frac{3}{\overline{N}^2} \mathrm{Var} \left(\sum_{i=1}^{N} \cos\theta_i \right) = \frac{3}{\overline{N}^2} \overline{N} \langle \cos^2\theta \rangle = \frac{3}{\overline{N}} \langle \cos^2\theta \rangle . \tag{180}$$

The leading order terms in the averages of both N (Eq. 174) and $\cos^2\theta$ come only from the uniform χ_0 (Eq. 19). Specifically,

$$\overline{N} = \int_0^T dt \int a^2 d\Omega \; \alpha \bar{c}(a,\theta) = a^2 \alpha T \int d\Omega \frac{\gamma}{a^3} = \frac{4\pi\alpha\gamma T}{a} = \frac{\nu T \tilde{\alpha}}{1+\tilde{\alpha}}, \tag{181}$$

and the average of $\cos^2\theta$ over the sphere is

$$\langle \cos^2\theta \rangle = \frac{1}{4\pi} \int d\Omega \; \cos^2\theta = \frac{1}{3}. \tag{182}$$

Together these results produce Eq. 23 in the main text.

E. Effect of Non-Spherical Cell Geometry

Cells polarize and stretch in the direction of motion as they move. In this section, we investigate the effect that stretching has on the ability of the cell to sense the direction of the fluid flow. For simplicity, we incorporate stretching (or compressing) by investigating an ellipsoidal cell. We also ignore the effect of impermeability of the medium and simply use Stokes' flow. For a spherical cell, we find in the main text that the impermeability halves the error (taking w from 1 to 2) but does not change the overall scaling, and we expect the effect to be similar here. We also focus only on the absorbing case, where the deterministic convection-diffusion equation suffices to determine the statistics of the anisotropy measure.

1. Ellipsoidal Coordinate System

We will find it useful to adapt our coordinates to the shape of the cell surface in order to state the boundary condition for the convection-diffusion equation. Therefore, we first introduce a new coordinate system that we will call "ellipsoidal" for simplicity. Our new coordinates are not the same as the standard confocal ellipsoidal coordinates or the prolate or oblate spheroidal coordinates. They are also non-orthogonal, and therefore they give rise to off-diagonal terms in definitions such as the Laplacian, as we derive using differential geometry in a later section below. Nonetheless, they are a continuous deformation of spherical coordinates and are useful for specifying the boundary and visualizing the system.

The ellipsoidal coordinates are related to the cartesian ones via

$$\begin{aligned} x &= r_e q^{-1/3} \sin\theta_e \cos\phi_e, \\ y &= r_e q^{-1/3} \sin\theta_e \sin\phi_e, \\ z &= r_e q^{2/3} \cos\theta_e, \end{aligned} \tag{183}$$

where the angular variables (θ_e, ϕ_e) have the same ranges as the spherical angles (θ, ϕ): $\theta_e \in (0, \pi)$ and $\phi_e \in (0, 2\pi)$. Ellipsoids are surfaces of constant r_e. $q > 0$ is a parameter characterizing the deformation: the z-axis is compressed for $q < 1$, and the z-axis is stretched for $q > 1$, as illustrated in 7A. The ellipsoidal coordinates reduce to spherical coordinates when $q = 1$.

More generally, the relationship between the ellipsoidal and spherical coordinates is obtained by comparing Eq. 183 with the standard spherical-cartesian relations,

$$\begin{aligned} x &= r\sin\theta\cos\phi, \\ y &= r\sin\theta\sin\phi, \\ z &= r\cos\theta, \end{aligned} \tag{184}$$

as follows. First, Eq. 183 implies that $r_e = q^{1/3}\sqrt{x^2+y^2+q^{-2}z^2}$. Inserting Eq. 184 for x, y, and z then yields $r_e = rq^{1/3}\sqrt{1+(q^{-2}-1)\cos^2\theta}$. Second, Eq. 183 implies $\cos\theta_e = z/r_e q^{2/3}$. Inserting Eq. 184 for z and the previous result for r_e gives $\cos\theta_e = q^{-1}\cos\theta/\sqrt{1+(q^{-2}-1)\cos^2\theta}$. Third, by considering the ratio y/x in both Eq. 183 and Eq. 184, one sees that $\tan\phi_e = \tan\phi$, or $\phi_e = \phi$. In summary,

$$\begin{aligned} r_e &= rq^{1/3}\sqrt{1+(q^{-2}-1)\cos^2\theta}, \\ \cos\theta_e &= \frac{q^{-1}\cos\theta}{\sqrt{1+(q^{-2}-1)\cos^2\theta}}, \\ \phi_e &= \phi. \end{aligned} \tag{185}$$

Eq. 185 gives the ellipsoidal coordinates in terms of spherical coordinates. The inverse is

$$\begin{aligned} r &= r_e q^{-1/3}\sqrt{1+(q^2-1)\cos^2\theta_e}, \\ \cos\theta &= \frac{q\cos\theta_e}{\sqrt{1+(q^2-1)\cos^2\theta_e}}, \\ \phi &= \phi_e. \end{aligned} \tag{186}$$

The parametrization in Eq. 183 explicitly conserves the volume of the ellipsoid. To see this fact, we recall that if the x, y, and z semi-axis lengths are A, B, and C respectively, then the volume of the ellipsoid is

$$V = \frac{4\pi}{3}ABC. \tag{187}$$

Taking $A = B = r_e q^{-1/3}$ and $C = r_e q^{2/3}$, we see that the ellipsoid has the same volume as a sphere of radius $r_e > 0$, independent of q. Note that q is the ratio of axis lengths, as $q = C/A$.

Although the volume is conserved, the surface area is not. This means that α and β should change with q in order to keep the total number of receptors on the surface and the rate of secretion constant, respectively. To account for this, we need the area element. A point on the surface of an ellipse in cartesian components is

$$\vec{r} = r_e q^{-1/3} \left\langle \sin\theta_e \cos\phi_e, \sin\theta_e \sin\phi_e, q\cos\theta_e \right\rangle . \tag{188}$$

The area element may be computed as the cross-product

$$dS_{r_e} = ||\partial_{\theta_e}\vec{r} \times \partial_{\phi_e}\vec{r}||d\theta_e d\phi_e = r_e^2 q^{1/3} \sin\theta_e \sqrt{1 + (q^{-2} - 1)\cos^2\theta_e}\; d\theta_e d\phi_e. \tag{189}$$

Letting S_{r_e} denote the integral of dS_{r_e} over the full ranges of the angular variables, we take

$$\alpha_e = \frac{4\pi a^2 \alpha}{S_a}, \qquad \beta_e = \frac{4\pi a^2 \beta}{S_a}. \tag{190}$$

We perform the integral S_a numerically.

2. Flow Lines

Next we find the laminar flow lines around the ellipsoid, where the flow points along the stretched/compressed axis (Fig. 7A). We do so following Ref. [88], which specifies a numerical method for calculating flow lines in the laminar limit of the incompressible Navier-Stokes equations around an object with azimuthal symmetry. We report the solution of Ref. [88] here in spherical coordinates, and then exploit our ellipsoidal coordinates when imposing the boundary conditions.

The flow velocity can be written

$$\vec{v} = \nabla \times \left(\frac{\psi(r,\theta)\hat{\phi}}{r\sin\theta} \right), \tag{191}$$

or in terms of its components,

$$\vec{v}\cdot\hat{r} = \frac{\partial_\theta \psi}{r^2 \sin\theta}, \quad \vec{v}\cdot\hat{\theta} = -\frac{\partial_r \psi}{r\sin\theta}, \quad \vec{v}\cdot\hat{\phi} = 0, \tag{192}$$

where ψ is the so-called stream function, and the last expression reflects the azimuthal symmetry. The general solution for ψ given in Ref. [88] is

$$\psi(r,\theta) = \sum_{n=2}^{\infty} \left(a_n r^{-n+1} + b_n r^{-n+3} + c_n r^n + d_n r^{n+2}\right) C_n^{(-1/2)}(\cos\theta), \tag{193}$$

where the $C_n^{(\mu)}$ are Gegenbauer polynomials.

We solve for the coefficients by imposing the boundary conditions. The flow at spatial infinity should point in the $\hat{z}$ direction

$$\lim_{r\to\infty} \vec{v} = v_0 \hat{z} = v_0(\cos\theta \hat{r} - \sin\theta\hat{\theta}). \tag{194}$$

Considering Eq. 192, we see that this holds if we have the asymptotic relation for large r

$$\psi \sim \frac{v_0 r^2}{2}\sin^2\theta = \frac{v_0 r^2}{2}(1-\cos^2\theta). \tag{195}$$

Aside from the factor $v_0 r^2$, the final expression is exactly $C_2^{(-1/2)}(\cos\theta)$. This can be used to solve for the c_n and d_n coefficients:

$$c_n = v_0\delta_{n,2}, \quad d_n = 0. \tag{196}$$

The general solution now takes the form

$$\psi(r,\theta) = \frac{v_0 r^2}{2}(1-\cos^2\theta) + \sum_{n=2}^{\infty}\left(a_n r^{-n+1} + b_n r^{-n+3}\right) C_n^{(-1/2)}(\cos\theta). \tag{197}$$

The remaining coefficients are determined by requiring the fluid velocity to vanish at the surface of the cell, which implies

$$\frac{\partial\psi}{\partial r} = 0, \qquad \frac{\partial\psi}{\partial(\cos\theta)} = 0 \tag{198}$$

there. The relationship between r and θ on the surface of the cell is given by the first line of Eq. 185 with $r_e = a$,

$$r = \frac{a}{q^{1/3}\sqrt{1+(q^{-2}-1)\cos^2\theta}}. \tag{199}$$

We use Eq. 199 to solve for the coefficients a_n and b_n in Eq. 197 using the following sampling procedure from Ref. [88]. We sample m points uniform randomly in $\cos\theta$ on the surface of the ellipsoid. For each point, we have two equations that result from inserting Eq. 197

into the two boundary conditions (Eq. 198) with r written in terms of $\cos\theta$ according to Eq. 199. This gives $2m$ equations. We truncate the sum in Eq. 197 at $n_{\max} = m + 1$. This gives $2m$ unknowns (the coefficients $\{a_n\}_2^{m+1}$ and $\{b_n\}_2^{m+1}$). The resulting linear system in the coefficients is solved by matrix inversion. Numerically, the matrix may be singular, and therefore we use the singular value decomposition. Once we solve for a_n and b_n, the flow lines follow from Eq. 192.

3. Convection-Diffusion Equation

Given the flow lines $\vec{v}$, we numerically solve the convection-diffusion equation (Eq. 17),

$$0 = D\nabla^2\overline{c} - \vec{v}\cdot\vec{\nabla}\overline{c}. \tag{200}$$

This equation is subject to the secretion/absorption boundary condition at the ellipsoidal cell surface (analogous to Eq. 18),

$$-D\hat{n}\cdot\vec{\nabla}\overline{c}|_{r_e=a} = \beta_e - \alpha_e\overline{c}|_{r_e=a}, \tag{201}$$

where $\hat{n}$ is the outward-pointing unit vector orthogonal to ellipsoid, and α_e and β_e are given in Eq. 190. To solve Eq. 200 subject to the ellipsoidal boundary condition, we derive the forms of the Laplacian $\nabla^2\overline{c}$ and convective term $\vec{v}\cdot\vec{\nabla}\overline{c}$ in ellipsoidal coordinates. Because the coordinates are non-orthogonal, it is most convenient to use the language of differential geometry (see Ref. [40]) to derive these forms.

a. Laplacian in Ellipsoidal Coordinates

Suppose that we change from one set of coordinates $\{x^\mu\}$ to another $\{y^{\mu'}\}$. A vector that transforms covariantly transforms like the chain rule for derivatives

$$V'_{\mu'} = \frac{\partial x^\mu}{\partial y^{\mu'}} V_\mu. \tag{202}$$

In the usual cartesian coordinates, we may write the derivative of a scalar in the direction of $\vec{v}$ as $\nabla_v = V^\mu\partial_\mu$, where the V^μ transform contravariantly

$$V'^{\mu'} = \frac{\partial y^{\mu'}}{\partial x^\mu} V^\mu \tag{203}$$

under a change of coordinates. A tensor is an object with multiple indices, where each index transforms covariantly or contravariantly independently. The basis vectors on a manifold can change from point to point, so one must specify a curve to transport vectors and covectors along to define derivatives. This method of using transport to differentiate is called the covariant derivative, and its components for a general tensor take the form

$$\nabla_\mu T^{\{\alpha\}}_{\{\beta\}} = \partial_\mu T^{\{\alpha\}}_{\{\beta\}} + \sum_{\alpha_i \in \{\alpha\}} \Gamma^{\alpha_i}_{\rho\mu} T^{\{\alpha|\alpha_i\to\rho\}}_{\{\beta\}} - \sum_{\beta_i \in \{\beta\}} \Gamma^{\rho}_{\beta_i\mu} T^{\{\alpha\}}_{\{\beta|\beta_i\to\rho\}}, \tag{204}$$

where $\{\alpha|\alpha_i \to \rho\}$ means that the i-th index has been changed to ρ and summed over, ∂_μ is ordinary differentiation with respect to the coordinates, and the $\Gamma^\rho_{\mu\nu}$ are the Christoffel symbols. The Christoffel symbols are not tensorial and are defined in terms of derivatives of the metric tensor $g_{\mu\nu}$

$$\Gamma^\rho_{\mu\nu} = \frac{g^{\rho\alpha}}{2}\left(\partial_\nu g_{\mu\alpha} + \partial_\mu g_{\nu\alpha} - \partial_\alpha g_{\mu\nu}\right). \tag{205}$$

The metric tensor $g_{\mu\nu}$ is defined in terms of the differential arc length $d\ell$ of curves

$$(d\ell)^2 = g_{\mu\nu} dx^\mu dx^\nu. \tag{206}$$

The metric tensor $g_{\mu\nu}$ may be used to lower indices, converting a contravariant vector to a covariant one. The inverse metric $g^{\mu\nu}$ may raise indices and perform the inverse conversion. When thought of as matrices, the inverse metric may be computed as the inverse of the metric.

We know that the metric in cartesian coordinates $g_{\text{cart},\mu\nu}$ is the identity matrix. It is often easier to compute the matrix of partial derivatives $\partial x^\mu/\partial y^\nu$, where $x^\mu = (x, y, z)$ denotes cartesian coordinates and y^μ denotes any new coordinates. We can use this to compute the metric

$$g_{\text{new},\mu\nu} = \frac{\partial x^{\mu'}}{\partial y^\mu}\frac{\partial x^{\nu'}}{\partial y^\nu} g_{\text{cart},\mu'\nu'}. \tag{207}$$

Letting $y^\mu = (r_e, \theta_e, \phi_e)$ be the ellipsoidal coordinates, the metric tensor in ellipsoidal coordinates is

$$g_{e,\mu\nu} = \begin{bmatrix} q^{\frac{4}{3}}\cos^2\theta_e + q^{-\frac{2}{3}}\sin^2\theta_e & r_e\sin\theta_e\cos\theta_e\left(q^{-\frac{2}{3}} - q^{\frac{4}{3}}\right) & 0 \\ r_e\sin\theta_e\cos\theta_e\left(q^{-\frac{2}{3}} - q^{\frac{4}{3}}\right) & r_e^2\left(q^{\frac{4}{3}}\sin^2\theta_e + q^{-\frac{2}{3}}\cos^2\theta_e\right) & 0 \\ 0 & 0 & q^{-\frac{2}{3}} r_e^2 \sin^2\theta_e \end{bmatrix}. \tag{208}$$

Inverting this gives the inverse metric

$$g_e^{\mu\nu} = \begin{bmatrix} q^{\frac{2}{3}}\sin^2\theta_e + q^{-\frac{4}{3}}\cos^2\theta_e & \frac{1}{r_e}\sin\theta_e\cos\theta_e\left(q^{\frac{2}{3}} - q^{-\frac{4}{3}}\right) & 0 \\ \frac{1}{r_e}\sin\theta_e\cos\theta_e\left(q^{\frac{2}{3}} - q^{-\frac{4}{3}}\right) & \frac{1}{r_e^2}\left(q^{\frac{2}{3}}\cos^2\theta_e + q^{-\frac{4}{3}}\sin^2\theta_e\right) & 0 \\ 0 & 0 & \frac{q^{\frac{2}{3}}}{r_e^2\sin^2\theta_e} \end{bmatrix}. \tag{209}$$

With the metric and inverse metric, we may compute the Christoffel symbols

$$\begin{gathered} \Gamma^1_{e,\mu\nu} = \begin{bmatrix} 0 & 0 & 0 \\ 0 & -r_e & 0 \\ 0 & 0 & -r_e\sin^2\theta_e \end{bmatrix}, \quad \Gamma^2_{e,\mu\nu} = \begin{bmatrix} 0 & \frac{1}{r_e} & 0 \\ \frac{1}{r_e} & 0 & 0 \\ 0 & 0 & -\sin\theta_e\cos\theta_e \end{bmatrix}, \\ \Gamma^3_{e,\mu\nu} = \begin{bmatrix} 0 & 0 & \frac{1}{r_e} \\ 0 & 0 & \frac{\cos\theta_e}{\sin\theta_e} \\ \frac{1}{r_e} & \frac{\cos\theta_e}{\sin\theta_e} & 0 \end{bmatrix}. \end{gathered} \tag{210}$$

We can use this to find the gradient and Laplacian of a scalar in the new coordinates. The gradient describes the components of the covariant derivative, which is just the ordinary derivative, as scalars are invariant under changes of coordinates

$$\nabla_\mu f = \partial_\mu f. \tag{211}$$

The scalar Laplacian is the divergence of the gradient, which is

$$\nabla^2 f = g_e^{\mu\nu}\nabla_\mu\nabla_\nu f = g_e^{\mu\nu}\left(\partial_\mu\partial_\nu f - \Gamma^\rho_{e,\mu\nu}\partial_\rho f\right). \tag{212}$$

Using the expressions derived above, we find

$$\begin{aligned} \nabla^2 f = q^{\frac{2}{3}}\Bigg[&\left(\sin^2\theta_e + q^{-2}\cos^2\theta_e\right)\frac{\partial^2 f}{\partial r_e^2} + \frac{1}{r_e}\left(1 + \cos^2\theta_e + q^{-2}\sin^2\theta_e\right)\frac{\partial f}{\partial r_e} \\ &+ \frac{1}{r_e^2}\left(\cos^2\theta_e + q^{-2}\sin^2\theta_e\right)\frac{\partial^2 f}{\partial\theta_e^2} + \frac{1}{r_e^2}\left(\frac{\cos\theta_e}{\sin\theta_e} - 2\left(1 - q^{-2}\right)\sin\theta_e\cos\theta_e\right)\frac{\partial f}{\partial\theta_e} \\ &+ \frac{1}{r_e^2\sin^2\theta_e}\frac{\partial^2 f}{\partial\phi_e^2} + \frac{2}{r_e}\left(1 - q^{-2}\right)\sin\theta_e\cos\theta_e\frac{\partial^2 f}{\partial r_e\partial\theta_e}\Bigg]. \end{aligned} \tag{213}$$

This is the Laplacian in ellipsoidal coordinates.

b. Convective Term in Ellipsoidal Coordinates

The convective term can be written in contravariant form as

$$\vec{v} \cdot \vec{\nabla} \overline{c} = V^{\mu} \partial_{\mu} \overline{c}. \tag{214}$$

The gradient vector $\partial_{\mu} = (\partial_{r_e}, \partial_{\theta_e}, \partial_{\phi_e})$ is straightforward to write in ellipsoidal coordinates, but for the velocity vector it is easiest to transform to spherical coordinates,

$$\vec{v} \cdot \vec{\nabla} \overline{c} = \frac{\partial y^{\mu}}{\partial x^{\nu}} V^{\nu}_{\text{sph}} \partial_{\mu} \overline{c}, \tag{215}$$

and then write $\partial y^{\mu} / \partial x^{\nu}$ and V^{ν}_{sph} in terms of r_e, θ_e, and ϕ_e. The former is obtained by differentiating Eq. 185, and then inserting Eq. 186 into the results,

$$\frac{\partial y^{\mu}}{\partial x^{\nu}} = \frac{\partial (r_e, \theta_e, \phi_e)}{\partial (r, \theta, \phi)} = \begin{bmatrix} \frac{q^{1/3}}{\sqrt{1+(q^2-1)\cos^2\theta_e}} & r_e q^{-1}(q^2-1)\sin\theta_e \cos\theta_e & 0 \\ 0 & \frac{1}{2} q^{-1}\left[1 + q^2 + (q^2-1)\cos(2\theta_e)\right] & 0 \\ 0 & 0 & 1 \end{bmatrix}. \tag{216}$$

The latter is obtained by writing the curl (Eq. 191) in tensor notation,

$$V^{\alpha} = \epsilon^{\alpha\beta\gamma} \partial_{\beta} \Psi_{\gamma}, \tag{217}$$

where $\vec{\Psi} = \psi \hat{\phi} / r \sin\theta$ and $\epsilon^{\alpha\beta\gamma}$ is the Levi-Civita tensor. For orthogonal coordinate systems, like spherical coordinates, the Levi-Civita tensor may be written in terms of the Levi-Civita symbol $\tilde{\epsilon}$

$$\epsilon^{\alpha\beta\gamma} = \sqrt{\det(g^{\mu\nu})}\, \tilde{\epsilon}^{\alpha\beta\gamma}, \tag{218}$$

where $\tilde{\epsilon}$ is $+1$ for even permutations of $(1, 2, 3)$, -1 for odd permutations, and 0 for repeated indices. The metric in spherical coordinates is well-known (and may be obtained from our ellipsoidal metric by taking $q \to 1$),

$$g^{\mu\nu}_{\text{sph}} = \begin{bmatrix} 1 & 0 & 0 \\ 0 & \frac{1}{r^2} & 0 \\ 0 & 0 & \frac{1}{r^2 \sin^2\theta} \end{bmatrix}, \tag{219}$$

which implies that

$$\sqrt{\det(g^{\mu\nu}_{\text{sph}})} = \frac{1}{r^2 \sin\theta}. \tag{220}$$

However, the basis vectors that are commonly used in differential geometry are not normalized like $\hat{\phi}$. To find the basis vectors, we will start from the usual cartesian basis vectors, which are normalized and take the familiar form, and transform them. We expect $\hat{\phi}$ to be proportional to $\vec{e}^{\,3}_{\text{sph}}$. We need the inverse Jacobian

$$\frac{\partial x^\mu}{\partial y^\nu} = \frac{\partial(x,y,z)}{\partial(r,\theta,\phi)} = \begin{bmatrix} \sin\theta\cos\phi & r\cos\theta\cos\phi & -r\sin\theta\sin\phi \\ \sin\theta\sin\phi & r\cos\theta\sin\phi & r\sin\theta\cos\phi \\ \cos\theta & -r\sin\theta & 0 \end{bmatrix}. \tag{221}$$

We compute $\vec{e}^{\,3}_{\text{sph}}$

$$\begin{aligned} \vec{e}^{\,3}_{\text{sph}} &= g^{3\mu}_{\text{sph}} \frac{\partial x^\nu}{\partial y^\mu} \vec{e}_{\text{car},\nu} = g^{33}_{\text{sph}} \frac{\partial x^\nu}{\partial y^3} \vec{e}_{\text{car},\nu} = \frac{r\sin\theta(-\sin\phi\vec{e}_{\text{car},1} + \cos\phi\vec{e}_{\text{car},2})}{r^2\sin^2\theta}, \\ &= \frac{-\sin\phi\vec{e}_{\text{car},1} + \cos\phi\vec{e}_{\text{car},2}}{r\sin\theta} = \frac{\hat{\phi}}{r\sin\theta}. \end{aligned} \tag{222}$$

We find the covariant components of $\vec{\Psi}$ in spherical coordinates by writing $\vec{\Psi} = \Psi_\mu \vec{e}^{\,\mu}_{\text{sph}}$, which implies

$$\Psi_1 = 0, \quad \Psi_2 = 0, \quad \Psi_3 = \psi. \tag{223}$$

Using this to evaluate Eq. 217 gives

$$V^1_{\text{sph}} = \frac{\partial_\theta \psi}{r^2\sin\theta}, \quad V^2_{\text{sph}} = -\frac{\partial_r \psi}{r^2\sin\theta}, \quad V^3_{\text{sph}} = 0. \tag{224}$$

Note that these are not the same as the components of $\vec{v}$ along the unit vectors in spherical coordinates (Eq. 192). They are slightly different because they are the components along the covariant basis vectors in spherical coordinates.

Thus, the convective term in ellipsoidal coordinates is given by Eq. 215, with $\partial y^\mu/\partial x^\nu$ given by Eq. 216 and V^ν_{sph} given by Eq. 224. In Eq. 224, ψ is given by Eq. 197, and r and θ are converted to ellipsoidal coordinates via Eq. 186.

4. Relative Error

Finally, after obtaining the concentration $\overline{c}$ from Eq. 200, we calculate the mean and variance of the anisotropy measure. The anisotropy measure is defined analogously to Eq. 21, as

$$A_e = \frac{1}{\overline{N}} \int_0^T dt \int dS_a \alpha_e c(a, \theta_e, \phi_e, t) \cos\theta, \tag{225}$$

where

$$\overline{N} = T \int dS_a \alpha_e \overline{c}(a, \theta_e) \tag{226}$$

is the mean number of absorbed molecules in time T. The mean of Eq. 225 is

$$\overline{A}_e = \frac{T}{\overline{N}} \int dS_a \alpha_e \overline{c}(a, \theta_e) \cos\theta. \tag{227}$$

Eqs. 226 and 227 are evaluated numerically using $\overline{c}$, where we write $\cos\theta$ in terms of $\cos\theta_e$ according to Eq. 186.

The variance of Eq. 225 is $1/\overline{N}$, just as in Eq. 23. To prove this fact, we use a generalization of the argument in Section V above. Specifically, Eq. 178 still holds for the statistics in the $\hat{z}$ direction, and Eq. 179 still holds for the Poissonian N in general. However, the variance of A_e is no longer the variance in the $\hat{z}$ direction multiplied by a factor of three (Eq. 180) because the ellipsoid breaks the spherical symmetry. Instead, we must write the components from the $\hat{x}$, $\hat{y}$, and $\hat{z}$ directions explicitly,

$$\sigma^2_{A_e} = \frac{1}{\overline{N}^2} \left[\mathrm{Var}\left(\sum_{i=1}^{N} \sin\theta_i \cos\phi_i \right) + \mathrm{Var}\left(\sum_{i=1}^{N} \sin\theta_i \cos\phi_i \right) + \mathrm{Var}\left(\sum_{i=1}^{N} \cos\theta_i \right) \right]. \tag{228}$$

Nonetheless, we can still write the analogs of Eq. 178 explicitly for the $\hat{x}$, $\hat{y}$, and $\hat{z}$ directions,

$$\left\langle \left(\sum_{i=1}^{N} \sin\theta_i \cos\phi_i \right)^2 \right\rangle = \left\langle \sum_{i=1}^{N} \sin^2\theta_i \cos^2\phi_i \right\rangle + \left\langle \sum_{i\neq j} \sin\theta_i \cos\phi_i \sin\theta_j \cos\phi_j \right\rangle$$
$$= \langle N \rangle \langle \sin^2\theta \cos^2\phi \rangle + \langle N(N-1) \rangle \langle \sin\theta \cos\phi \rangle^2 , \tag{229}$$

$$\left\langle \left(\sum_{i=1}^{N} \sin\theta_i \sin\phi_i \right)^2 \right\rangle = \left\langle \sum_{i=1}^{N} \sin^2\theta_i \sin^2\phi_i \right\rangle + \left\langle \sum_{i\neq j} \sin\theta_i \sin\phi_i \sin\theta_j \sin\phi_j \right\rangle$$
$$= \langle N \rangle \langle \sin^2\theta \sin^2\phi \rangle + \langle N(N-1) \rangle \langle \sin\theta \sin\phi \rangle^2 , \tag{230}$$

$$\left\langle \left(\sum_{i=1}^{N} \cos\theta_i \right)^2 \right\rangle = \left\langle \sum_{i=1}^{N} \cos^2\theta_i \right\rangle + \left\langle \sum_{i\neq j} \cos\theta_i \cos\theta_j \right\rangle$$
$$= \langle N \rangle \langle \cos^2\theta \rangle + \langle N(N-1) \rangle \langle \cos\theta \rangle^2 . \tag{231}$$

Due to Eq. 179, the final terms in Eqs. 229-231 are still the squares of the means. Therefore, Eq. 228 becomes

$$\sigma_{A_e}^2 = \frac{1}{\overline{N}^2} \left[\overline{N} \langle \sin^2\theta \cos^2\phi \rangle + \overline{N} \langle \sin^2\theta \sin^2\phi \rangle + \overline{N} \langle \cos^2\theta \rangle \right] = \frac{1}{\overline{N}}, \tag{232}$$

as we sought to prove.

5. Results

For a given value of the ellipsoidal scale factor q, we compute the flow lines according to section B using $m = 50$ points, and we solve the convection-diffusion equation for $\overline{c}$ according to section C. The ellipsoidal boundary condition in Eq. 201 is implemented in Mathematica using the "NeumannValue" function. We also use an ellipsoid at $r_e = r_{e,\max}$ for the outer boundary, where we impose $\overline{c}|_{r_e = r_{e,\max}} = 0$. We compute the error $\sigma_{A_e}/\overline{A}_e$, relative to the spherical case $\sigma_A/\overline{A}$, as

$$R_q = \frac{\sigma_{A_e}/\overline{A}_e}{\sigma_A/\overline{A}}, \tag{233}$$

where $\sigma_A/\overline{A}$ is also computed numerically.

Fig. 7B shows the ratio R_q over the range where q deviates from 1 by as much as 20%. We see that elongating in the flow direction ($q > 1$) decreases the sensory error, whereas compressing in the flow direction ($q < 1$) increases the sensory error. Going beyond this

range in q requires prohibitively large computational runtime, as more than $m = 50$ terms are required in the flow lines for numerical accuracy, which significantly increases the runtime of the numerical routine for solving the convection-diffusion equation. Nonetheless, we can extrapolate out to $q = 2$, which corresponds to a cell that is twice as long as it is wide, for a rough idea of the effect. Treating the result in Fig. 7B as a line (although it is slightly concave up) indicates that elongation to this extent would reduce the sensory error by about 30%. Thus, we conclude that elongation in the flow direction can lead to a moderate improvement in the precision of flow sensing.

Appendix C Supplement for "Precision of Protein Thermometry"

A. Derivation of Error for the Perfect Instrument

Fox [39] considered local fluctuations in the temperature $T(x,t)$ of a homogeneous medium near equilibrium with a uniform, time-independent mean

$$\langle T(\vec{x},t)\rangle = \overline{T}. \tag{234}$$

This was done in the context of linear, irreversible thermodynamics, and the correlation function for fluctuations in this regime is (Eq. 34)

$$\langle \Delta T(\vec{x},t)\Delta T(\vec{y},t')\rangle = \frac{k_B\overline{T}^2}{\rho c_s}\left(\frac{\rho c_s}{4\pi K|t-t'|}\right)^{3/2}\exp\left[-\frac{\rho c_s||\vec{x}-\vec{y}||^2}{4K|t-t'|}\right], \tag{235}$$

where k_B is Boltzmann constant, ρ is the mass density of the medium, c_s is the specific heat, and K is the thermal conductivity. We generalize the perfect instrument of Berg and Purcell to sense temperature as follows. We assume that the detector is a completely permeable sphere of radius a that can record the fluctuating temperature at each point within its volume at each instant. It then performs an average over its volume and some time interval of length τ, yielding the estimate

$$\hat{T} = V^{-1}\tau^{-1}\int_V d^3\vec{x}\int_0^\tau T(\vec{x},t)dt. \tag{236}$$

Since it is linear in the temperature, we note that

$$\langle\hat{T}\rangle = \overline{T}. \tag{237}$$

The fluctuations are given by the double integral of the correlation function in space and time

$$\sigma^2(\hat{T}) = V^{-2}\tau^{-2}\int_V d^3\vec{x}d^3\vec{y}\int_0^\tau\langle\Delta T(\vec{x},t)\Delta T(\vec{y},t')\rangle dtdt'. \tag{238}$$

1. Short-Time Limit

In the short-time limit, $\tau \to 0$, the average is purely spatial

$$\hat{T} \sim V^{-1} \int_V T(\vec{x}, t) d^3\vec{x} \tag{239}$$

and the correlation function is a delta function

$$\langle \Delta T(\vec{x}, t) \Delta T(\vec{y}, t) \rangle = \frac{k_B \overline{T}^2}{\rho c_s} \delta(\vec{x} - \vec{y}). \tag{240}$$

With this, the variance in our estimator is

$$\sigma^2(\hat{T}) \sim \frac{k_B \overline{T}^2}{\rho c_s V^2} \int_V \delta(\vec{x} - \vec{y}) d^3\vec{x} d^3\vec{y} = \frac{3 k_B \overline{T}^2}{4\pi \rho c_s a^3}. \tag{241}$$

The noise-to-signal ratio is

$$\frac{\sigma(\hat{T})}{\overline{T}} \sim \sqrt{\frac{3 k_B}{4\pi \rho c_s a^3}}, \tag{242}$$

as in Eq. 35 (top case).

2. Long-Time Limit

We will start by performing the time integrals first. We perform a change of variables from (t, t') to (Δ, t'), with $\Delta = t - t'$, and switch the order of integration so that we integrate over t' first. We can do the time integrals analytically, which yields

$$\begin{aligned} \sigma^2(\hat{T}) = \frac{k_B \overline{T}^2}{V^2} \int_V \Bigg[& -\frac{e^{-c_s \rho ||\vec{x} - \vec{y}||^2 / 4K\tau} \sqrt{\rho c_s}}{2(\pi K \tau)^{3/2}} \\ & + \frac{(c_s \rho ||\vec{x} - \vec{y}||^2 + 2K\tau)}{4\pi K^2 ||\vec{x} - \vec{y}|| \tau^2} \text{erfc}\left(||\vec{x} - \vec{y}|| \sqrt{\frac{\rho c_s}{4K\tau}} \right) \Bigg] d^3\vec{x} d^3\vec{y}. \end{aligned} \tag{243}$$

In the long-time limit, the term that goes as τ^{-1} decays the slowest and dominates the expression. We may also set the complementary error function to one, as the argument is small. This simplifies the expression to

$$\sigma^2(\hat{T}) \sim \frac{k_B \overline{T}^2}{2\pi K \tau V^2} \int_V \frac{d^3\vec{x} d^3\vec{y}}{||\vec{x} - \vec{y}||}. \tag{244}$$

One can evaluate this integral by expanding it in terms of spherical harmonics or recognizing that it is related to the volume averaged potential inside of a uniformly charged sphere. Either way, the integral comes out to

$$V^{-2} \int_V \frac{d^3\vec{x} d^3\vec{y}}{||\vec{x} - \vec{y}||} = \frac{6}{5a}. \tag{245}$$

Putting everything together, we find

$$\frac{\sigma(\hat{T})}{\overline{T}} \sim \sqrt{\frac{3k_B}{5\pi K a \tau}}, \tag{246}$$

as in Eq. 35 (bottom case).

B. Fit to the Circular Dichroism Data

In their experiment, Hurme et al. used circular dichroism to infer the fraction of TlpA units in the monomeric state as a function of temperature *in vitro* [56]. The resulting curves are dependent on the supplied concentration of subunits, and they considered two concentrations: 0.12 μM and 3.61 μM. From a blotting analysis, they estimated the *in vivo* concentration as 0.36 μM at 28 °C and 0.6 μM at 37 °C. Both of these are closer to the 0.12 μM value used *in vitro*, so we use this case. We fit the fraction of TlpA units in the monomeric state as a function of temperature with a sigmoid

$$f(T) = \frac{1}{1 + \exp(-4(T - T_M)/\Delta T)} \tag{247}$$

using the method of least squares to determine the parameters. We find $T_M = 39$ °C and $\Delta T = 6.3$ °C. The fit is shown in Fig. 11.

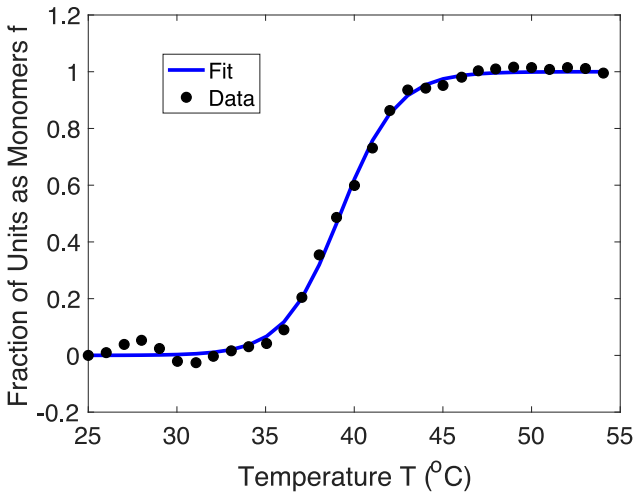

Figure 11: Fraction of TlpA units in the monomer state as a function of temperature. The black dots are the experimental data (open circles in Fig. 5C of Ref. [56], while the blue line is the sigmoidal fit (Eq. 247) with half-maximal temperature $T_M = 39$ °C and width $\Delta T = 6.3$ °C.

C. Derivation of Results for Biochemical Models

1. Properties of the Ornstein-Uhlenbeck Process

The Ornstein-Uhlenbeck process is important because it appears as the linearization of any Markovian chemical master equation. The stochastic differential equation takes the form

$$d\vec{X}_t = \mathcal{J}(\vec{X}_t - \vec{\mu})dt + d\vec{N}_t, \tag{248}$$

where $\vec{X}_t$ is n dimensional, the Jacobian matrix $\mathcal{J}$ and the mean $\vec{\mu}$ are constant in time, and $\vec{N}_t$ is a vector of n correlated and scaled Wiener processes where the mean is zero and the covariances are given by

$$\langle \vec{N}_t \vec{N}_s^T \rangle = \min(s,t)\Sigma, \tag{249}$$

for Σ symmetric and positive-definite. The general solution is

$$\vec{X}_t = \vec{\mu} + e^{\mathcal{J}t}(\vec{X}_0 - \vec{\mu}) + \int_0^t e^{\mathcal{J}(t-s)} d\vec{N}_s. \tag{250}$$

The steady state mean is $\vec{\mu}$, and the steady state covariance matrix is computed through

$$\mathcal{C} = \lim_{t\to\infty} \left\langle (\vec{X}_t - \vec{\mu})(\vec{X}_t - \vec{\mu})^T \right\rangle. \tag{251}$$

In order for this limit to exist, $\mathcal{J}$ must have eigenvalues with negative real parts, and we assume this to be the case, as this also implies that the deterministic system is stable. The Itô isometry [60] can be used to simplify this to an integral

$$\mathcal{C} = \int_0^\infty e^{\mathcal{J}t}\Sigma e^{\mathcal{J}^T t} dt. \tag{252}$$

By using integration by parts, we find the Lyapunov equation

$$\mathcal{J}\mathcal{C} + \mathcal{C}\mathcal{J}^T + \Sigma = 0. \tag{253}$$

This is easier to solve in practice, since it is linear in the components of $\mathcal{C}$.

Now we compute the cross-correlation matrix. We start in steady state, so we assume that $\vec{X}_0$ is gaussian distributed with mean $\vec{\mu}$ and covariances given by the steady state covariance matrix $\mathcal{C}$. The cross-correlation matrix is defined through

$$\mathcal{C}(\tau) = \left\langle (\vec{X}_{t+\tau} - \vec{\mu})(\vec{X}_t - \vec{\mu})^T \right\rangle, \tag{254}$$

where stationarity removes the t-dependence. Progress can be made by using the Itô isometry again and proceeding by cases depending on the sign of τ. This yields the result

$$\mathcal{C}(\tau) = \begin{cases} e^{\mathcal{J}\tau}\mathcal{C}, & \tau > 0, \\ \mathcal{C}e^{-\mathcal{J}^T\tau}, & \tau < 0. \end{cases} \tag{255}$$

Now let's put this all together. If $\vec{X}$ is a stationary stochastic process, the covariances of the time average $\mathcal{C}_{\text{TA}}$ over the window $[0, \tau]$ are related to the cross-correlations $\mathcal{C}(t)$ via

$$\mathcal{C}_{\text{TA}}(\tau) = \tau^{-2} \int_0^\tau \int_0^\tau \mathcal{C}(t - t') dt dt'. \tag{256}$$

As before, we change to the pair of variables (Δ, t'), with $\Delta = t - t'$, and switch the order of integration so that t' is integrated first. This leads to

$$\mathcal{C}_{\text{TA}}(\tau) = \tau^{-2} \left[\int_0^\tau (\tau - \Delta)\mathcal{C}(\Delta) d\Delta + \int_{-\tau}^0 (\tau + \Delta)\mathcal{C}(\Delta) d\Delta \right]. \tag{257}$$

Using the specific form of our cross-correlation matrix and integrating by parts gives

$$\mathcal{C}_{\mathrm{TA}}(\tau) = \tau^{-2}\left[-\tau\mathcal{J}^{-1}\mathcal{C} + \mathcal{J}^{-2}\left[e^{\mathcal{J}\tau} - \mathbb{I}\right]\mathcal{C} - \tau\mathcal{C}(\mathcal{J}^T)^{-1} + \mathcal{C}(\mathcal{J}^T)^{-2}\left[e^{\mathcal{J}^T\tau} - \mathbb{I}\right]\right], \quad (258)$$

the inverse of $\mathcal{J}$ exists since the eigenvalues have negative real parts and we have used the shorthand $\mathcal{J}^{-2} = (\mathcal{J}^{-1})^2$. We can simplify things a bit further by using Eq. 253 to yield

$$\mathcal{C}_{\mathrm{TA}}(\tau) = \tau^{-2}\left[\tau\mathcal{J}^{-1}\Sigma(\mathcal{J}^T)^{-1} + \mathcal{J}^{-2}\left[e^{\mathcal{J}\tau} - \mathbb{I}\right]\mathcal{C} + \mathcal{C}(\mathcal{J}^T)^{-2}\left[e^{\mathcal{J}^T\tau} - \mathbb{I}\right]\right]. \quad (259)$$

The first term is what we would find in the zero-frequency limit of the power spectrum.

2. Reactions and General Setting

In our model, we have a monomer that can reversibly form a dimer. The monomer is actively produced, but the dimer represses the production of the monomer, and both are lost via dilution, leading to the reactions

$$2\,\mathrm{M} \underset{k_m}{\overset{k_d}{\rightleftharpoons}} \mathrm{D}, \quad \mathrm{M} \underset{g(d_t)}{\overset{k^-}{\rightleftharpoons}} \varnothing, \quad \mathrm{D} \xrightarrow{k^-} \varnothing, \text{ with } g(d_t) = \frac{k^+}{1+\alpha d_t}. \quad (260)$$

One can write the Kramers-Moyal expansion for the stochastic reactions. Doing so out to second-order derivatives yields a Fokker-Planck equation, which corresponds to the following stochastic differential equations test

$$\begin{aligned} dd_t &= [k_d m_t^2 - (k_m + k^-)d_t]dt + \sqrt{k_d m_t^2 + k_m d_t}dW_t^{(1)} + \sqrt{k^- d_t}dW_t^{(2)}, \\ dm_t &= \left[\frac{k^+}{1+\alpha d_t} + 2k_m d_t - k^- m_t - 2k_d m_t^2\right]dt \\ &\qquad - 2\sqrt{k_d m_t^2 + k_m d_t}dW_t^{(1)} + \sqrt{\frac{k^+}{1+\alpha d_t} + k^- m_t}dW_t^{(3)}, \end{aligned} \quad (261)$$

where $W_t^{(1)}$, $W_t^{(2)}$, $W_t^{(3)}$ are standard, independent Wiener processes with variance t.

From the deterministic equations, it is easy to see that there is a unique positive steady state. The fraction of TlpA molecules in the monomer state

$$f = \frac{\overline{m}}{\overline{m} + 2\overline{d}}, \quad (262)$$

has been well characterized experimentally, where the bars denote the deterministic steady state or mean values. We can use this to solve for the dimer number in terms of the monomer number and fraction

$$\overline{d} = \frac{\overline{m}}{2}\left(\frac{1-f}{f}\right). \tag{263}$$

Using the steady state condition from the dimer's equation of motion gives

$$\frac{k_m + k^-}{k_d} = \frac{\overline{m}^2}{\overline{d}}. \tag{264}$$

We can use Eq. 263 to eliminate the dimer, which gives

$$k_m = \frac{2\overline{m}fk_d}{1-f} - k^-. \tag{265}$$

We will make this substitution when solving the rate equations for $\overline{m}$.

3. Derivation for the "Fixed Pool" Model

For the fixed pool, we take k^+ and k^- to zero. This makes $m_t + 2d_t = n$ a conserved quantity that we call the pool size. We can eliminate the dimer from the dynamics

$$dm_t = [k_m(n-m_t) - 2k_d m_t^2]dt - 2\sqrt{k_d m_t^2 + k_m\left(\frac{n-m_t}{2}\right)}dW_t^{(1)}. \tag{266}$$

We start by finding the steady state mean. We do so by identifying the m value that causes the deterministic term to vanish. Using Eq. 265, this gives $\overline{m} = nf$, as expected. To convert noise in molecules to noise in a temperature estimate, we also need a linearization factor $d\overline{m}/dT$, which is just nf'.

Now we will linearize the system to find the fluctuations. In doing so, we will also confirm that the fixed point is linearly stable. Letting $\delta m_t = m_t - \overline{m}$ and expanding the equation to first-order in δm in the deterministic term and zeroth-order in the noise term, we find

$$d(\delta m_t) = -2k_d n\frac{f(2-f)}{1-f}\delta m_t dt - 2\sqrt{2k_d f^2 n^2}dW_t^{(1)} \tag{267}$$

The coefficient of the linearized deterministic term is negative, so the fixed point is deterministically stable. We see that the Jacobian and noise covariance matrix are

$$\mathcal{J} = -2k_d n\frac{f(2-f)}{1-f}, \quad \Sigma = 8k_d f^2 n^2. \tag{268}$$

With these, we can find the variance in the time average or the maximum likelihood estimate of the mean, as the Lyapunov equation is trivial to solve for scalars. The steady state variance may be computed from Eq. 253

$$\sigma^2(m) = \frac{2(1-f)fn}{2-f}. \tag{269}$$

The variance in the time averaged monomer number may be computed from Eq. 259 by using $\mathcal{C} = \sigma^2(m)$ and the expressions for $\mathcal{J}$ and Σ in Eq. 268. From Eq. 255, we see that the correlation timescale is $\tau_d = -1/\mathcal{J}$. This completes the derivation of Eq. 36.

4. Derivation for "Production-Dilution" Model, without and with Feedback

a. Deterministic Analysis

The deterministic equations for the system are

$$\begin{aligned} \dot{d} &= k_d m^2 - (k_m + k^-)d, \\ \dot{m} &= \frac{k^+}{1+\alpha d} + 2k_m d - k^- m - 2k_d m^2. \end{aligned} \tag{270}$$

The mean dimer number can be found from its equation of motion: $\overline{d} = k_d \overline{m}^2/(k_m + k^-)$. Using the dimer steady state equation and Eq. 263, we find that the monomer steady state value satisfies

$$0 = \frac{k^+}{1+\alpha\overline{m}(1-f)/(2f)} - \frac{k^-\overline{m}}{f}. \tag{271}$$

The production term decreases from k^+ to 0 monotonically for $\overline{m} > 0$, while the loss term increases monotonically from 0 to infinity, so there is exactly one stable, positive fixed point. We find that the positive root is

$$\overline{m} = \frac{f}{\alpha(1-f)}\left[\sqrt{1 + \frac{2(1-f)\alpha k^+}{k^-}} - 1\right], \tag{272}$$

as in Eq. 38. It will be helpful to compute the mean monomer number in the absence of autorepression. This is done by taking $\alpha \to 0$, where we find

$$m_0 := \lim_{\alpha\to 0} \overline{m} = \frac{fk^+}{k^-}. \tag{273}$$

as given above Eq. 37. We can treat m_0 as a free parameter and solve for f in terms of α, m_0, and $\overline{m}$

$$f = \frac{\overline{m}^2}{\overline{m}^2 + 2\alpha^{-1}(m_0 - \overline{m})}. \tag{274}$$

This will be useful in simplifying expressions later on.

We show that the fixed point is stable. The Jacobian at the fixed point is

$$\mathcal{J} = \begin{bmatrix} -k_m - k^- & 2k_d\overline{m} \\ 2k_m - \dfrac{\alpha k^+}{(1+\alpha\overline{d})^2} & -k^- - 4k_d\overline{m} \end{bmatrix}. \tag{275}$$

The eigenvalues of this matrix both have negative real parts if the trace is negative and the determinant is positive. Since $\overline{m} > 0$, it is trivial to see that this has a negative trace. Using Eqs. 263 and 265, it follows that the determinant is positive, so we conclude that this fixed point is stable.

b. Stochastic Analysis

Linearizing the noise term, we can read off the form of $\vec{N}_t$

$$\begin{bmatrix} N_t^{(1)} \\ N_t^{(2)} \end{bmatrix} = \begin{bmatrix} \sqrt{k_d\overline{m}^2 + k_m\overline{d}}W_t^{(1)} + \sqrt{k^-\overline{d}}W_t^{(2)} \\ -2\sqrt{k_d\overline{m}^2 + k_m\overline{d}}W_t^{(1)} + \sqrt{\dfrac{k^+}{1+\alpha\overline{d}} + k^-\overline{m}}W_t^{(3)} \end{bmatrix}. \tag{276}$$

We just need to identify the matrix Σ, which may be readily computed from the previous expression and simplified using the steady state equations and the expression for dimer from Eq. 263

$$\begin{aligned} \Sigma &= \begin{bmatrix} k_d\overline{m}^2 + k_m\overline{d} + k^-\overline{d} & -2\left(k_d\overline{m}^2 + k_m\overline{d}\right) \\ -2\left(k_d\overline{m}^2 + k_m\overline{d}\right) & 4\left(k_d\overline{m}^2 + k_m\overline{d}\right) + \dfrac{k^+}{1+\alpha\overline{d}} + k^-\overline{m} \end{bmatrix} \\ &= \begin{bmatrix} 2k_d\overline{m}^2 & -2\left(2k_d\overline{m}^2 - k^-\dfrac{\overline{m}(1-f)}{2f}\right) \\ -2\left(2k_d\overline{m}^2 - k^-\dfrac{\overline{m}(1-f)}{2f}\right) & 8k_d\overline{m}^2 + k^-\dfrac{\overline{m}(5f-1)}{2f} \end{bmatrix}. \end{aligned} \tag{277}$$

With this, our system of SDEs is in the canonical form for an OU process. The covariance matrix may be determined from Eq. 253. Using Eq. 274 to eliminate the fraction, we find that,

$$\begin{aligned}
\mathcal{C}_{1,1} &= \frac{(\overline{m}-m_0)\,k_d\,(-2\alpha\overline{m}^4\,(\alpha\overline{m}-2)+m_0\overline{m}^2\,(\alpha\overline{m}\,(3\alpha\overline{m}-16)+14))}{\alpha\mathcal{D}} \\
&+ \frac{(\overline{m}-m_0)\,k_d\,(4m_0^2\overline{m}\,(3\alpha\overline{m}-7)+14m_0^3)}{\alpha\mathcal{D}} \\
&- \frac{k^-m_0\,(\overline{m}-m_0)^{\,2}\,(\overline{m}\,(\alpha\overline{m}-4)+4m_0)}{\alpha\overline{m}\mathcal{D}}, \\
\mathcal{C}_{1,2} &= \mathcal{C}_{2,1} = \frac{\overline{m}\,(\overline{m}-m_0)^{\,2}\,(\overline{m}k_d\,(4\overline{m}\,(\alpha\overline{m}-2)+9m_0)+k^-\,(\overline{m}\,(\alpha\overline{m}-2)+2m_0))}{\mathcal{D}}, \\
\mathcal{C}_{2,2} &= -\frac{\overline{m}^2k_d\,(16\overline{m}^3\,(\alpha\overline{m}-2)+m_0\overline{m}^2\,(\alpha\overline{m}\,(2\alpha\overline{m}-47)+128))}{2\mathcal{D}} \\
&- \frac{\overline{m}^2k_d\,(m_0^2\overline{m}\,(31\alpha\overline{m}-160)+64m_0^3)}{2\mathcal{D}} \\
&- \frac{k^-\overline{m}^2\,(\overline{m}-m_0)\,(\alpha\overline{m}-2)\,(\alpha\overline{m}\,(\overline{m}\,(\alpha\overline{m}-2)+m_0\,(10-\alpha\overline{m}))+m_0)}{\alpha m_0\mathcal{D}} \\
&+ \frac{k^-m_0\,(\overline{m}-m_0)\,(\overline{m}^2\,(\alpha\overline{m}\,(18\alpha\overline{m}-59)-16)+m_0\overline{m}\,(29\alpha\overline{m}+20)-8m_0^2)}{2\alpha\overline{m}\mathcal{D}}, \\
\mathcal{D} &= \left(2\overline{m}^2\,(\alpha\overline{m}-2)-3m_0\overline{m}\,(\alpha\overline{m}-4)-8m_0^2\right) \\
&\qquad \times \left(\overline{m}k_d\,(\overline{m}\,(\alpha\overline{m}-4)+4m_0)+k^-\,(m_0-\overline{m})\right)
\end{aligned} \tag{278}$$

As before, the variance in the time averaged monomer number may be computed from Eq. 259 by using this covariance matrix with the expressions for $\mathcal{J}$ and Σ in Eqs. 275 and 277 respectively. The variance in the pool size may be computed from these results according to

$$\sigma^2(n) = \mathrm{cov}(2d+m, 2d+m) = 4\mathcal{C}_{1,1} + 4\mathcal{C}_{1,2} + \mathcal{C}_{2,2}, \tag{279}$$

where "cov" denotes the covariance.

We now describe how to arrive at Eq. 37. In the limit that protein loss is much slower than dimerization $k^- \ll k_d\overline{m}$, we find that the variance $\sigma^2(m) = \mathcal{C}_{2,2}$ and $\sigma^2(n)$ simplify to

$$\begin{aligned}
\sigma^2_{\mathrm{PDF}}(m) &= -\frac{2\alpha^2m_0\overline{m}^5+\alpha\,(16\overline{m}-31m_0)\,(\overline{m}-m_0)\,\overline{m}^3-32\,(\overline{m}-2m_0)\,(\overline{m}-m_0)^{\,2}\overline{m}}{2\,(\alpha\overline{m}^2\,(2\overline{m}-3m_0)-4\,(\overline{m}-2m_0)\,(\overline{m}-m_0))\,(\overline{m}\,(\alpha\overline{m}-4)+4m_0)}, \\
\sigma^2_{\mathrm{PDF}}(n) &= -\frac{m_0\,(\overline{m}\,(\alpha\overline{m}-4)+4m_0)\,(\overline{m}\,(2\alpha\overline{m}-7)+7m_0)}{2\alpha\overline{m}\,(\alpha\overline{m}^2\,(2\overline{m}-3m_0)-4\,(\overline{m}-2m_0)\,(\overline{m}-m_0))}.
\end{aligned} \tag{280}$$

In the limit of no feedback, $\alpha \to 0$, the expressions simplify further to

$$\sigma^2_{\mathrm{PD}}(m) = \frac{f\,(5f^2 - 17f + 16)\,k^+}{4(f-2)^2 k^-}, \quad \sigma^2_{\mathrm{PD}}(n) = \frac{(7-3f)k^+}{4k^-}. \tag{281}$$

We compute $\sigma^2_{\mathrm{FP}}(m)$ according to Eq. 269 but take $n = \overline{m}/f$, where the expression for $\overline{m}$ is taken from Eq. 272. Eq. 37 in the main text may be verified by computing $(\sigma^2_{\mathrm{PDF/PD}}(m) - \sigma^2_{\mathrm{FP}}(m))/\sigma^2_{\mathrm{PDF/PD}}(n)$, which simplifies to $f^2/(2-f)^2$ for both nonzero α (PDF) and zero α (PD).

5. Optimal Autorepression

The autorepression strength α has competing effects such that there is an optimal strength that minimizes the relative error. When the timescale separation is large, $k^- \ll k_d\overline{m}$, we find that the relative error $\sigma(m)/|d\overline{m}/dT| = \mathcal{C}^{1/2}_{2,2}/|d\overline{m}/dT|$ only depends on α, f, and the ratio k^+/k^-. To find the optimal α, we set $f = 1/2$, find where the derivative of the relative error with respect to α vanishes, and check that the second derivative with respect to α at that point is positive. There is exactly one positive α value where the derivative vanishes, and it occurs at

$$\alpha = \alpha^* = \frac{1.75}{k^+/k^-}, \tag{282}$$

as stated in the main text. The second derivative at this point is $0.0105 \times (k^+/k^-)^{3/2}$, so this is a local minimum. We find that the relative error is $\mathcal{O}(\alpha^{1/4})$ as $\alpha \to \infty$ in both cases, so this is the global minimum. Using the ratio $k^+/k^- = 2521$ estimated from experiments, this leads to $\alpha^* = 6.9 \times 10^{-4}$.

D. Monomer Readout vs. Dimer Readout

Here we compare the temperature estimation error inferred from the monomer number (as in the main text) and from the dimer number. We see in Fig. 12 that qualitatively the error has a similar dependence on the integration time in the two cases, and quantitatively the two only differ by a factor of order unity (ranging from approximately two to three depending on the integration time).

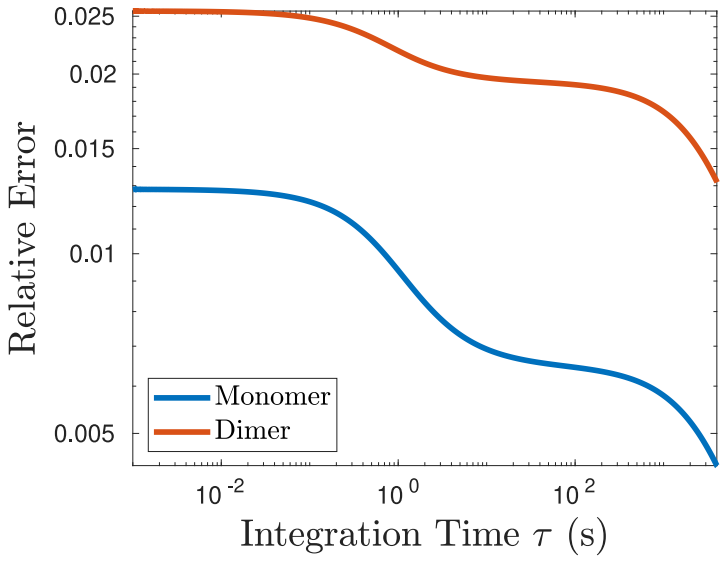

Figure 12: Comparing the relative error in temperature sensing inferred from the monomer number vs. from the dimer number. Parameters are as in the main text: $f = 1/2$, $\alpha = 6.94 \times 10^{-4}$, $k_d = 7.1 \times 10^{-4}$ s^{-1}, $k^- = 5.5 \times 10^{-4}$ s^{-1}, and $k^+/k^- = 2521$.

E. Maximum Likelihood Estimation

1. Trajectory Probability

We want to incorporate all of the available information to derive the limits to cellular performance. This requires the probability of observing a specified trajectory. Suppose that we have a stochastic differential equation with additive noise

$$d\vec{X}_t = \vec{F}(\vec{X}_t, t)dt + d\vec{N}_t, \tag{283}$$

where $\vec{X}_t$ is n-dimensional, and $\vec{N}$ is an n-dimensional scaled Wiener process where the mean is zero and the covariances are given by

$$\langle \vec{N}_t \vec{N}_s^T \rangle = \min(s, t)\Sigma, \tag{284}$$

for Σ symmetric and positive definite. We define the current at time t to be

$$\vec{J}(\vec{X}_t, t) = \vec{F}(\vec{X}_t, t)dt + d\vec{N}_t. \tag{285}$$

We can formally write the probability density of observing a trajectory by discretely sampling it at M points in time separated by time Δt and computing

$$P(\{\vec{X}_t\}_{t>0}|\vec{X}_0) = \lim_{M\to\infty} \left\langle \prod_{j=1}^{M} \delta(\vec{X}_j - \vec{X}_{j-1} - \vec{J}_{j-1}) \right\rangle_J, \tag{286}$$

where we used the Itô discretization, take $\Delta t \to 0$ such that $M\Delta t = \tau$ is constant, and use a subscript j to indicate evaluation at $j\Delta t$ and $\vec{X}_{j\Delta t}$. Since we specify the trajectory we are interested in, $\vec{J}_j$ is a gaussian random variable that is linearly related to the scaled Wiener processes via

$$\Delta\vec{N}_j = \vec{J}_j - \vec{F}_j\Delta t. \tag{287}$$

The increments of the Wiener process at different times are independent, while at the same time their covariance is

$$\left\langle \Delta\vec{N}_j \Delta\vec{N}_j^T \right\rangle = (\Delta t)\Sigma. \tag{288}$$

It follows that the jump distribution at one instant is

$$P(\vec{J}_j) = P(\Delta\vec{N}_j) \left| \det\left(\frac{\partial(\Delta\vec{N}_j)}{\partial\vec{J}_j} \right) \right| = \frac{\exp\left(-\frac{1}{2\Delta t} \langle \vec{J}_j - \vec{F}_j\Delta t, \Sigma^{-1}(\vec{J}_j - \vec{F}_j\Delta t)\rangle \right)}{\sqrt{(2\pi)^n \det(\Sigma)}}. \tag{289}$$

Since the process is Markovian, we may evaluate the average of the product of deltas term-by-term

$$P(\{\vec{X}_t\}_{t>0}|\vec{X}_0) = \lim_{M\to\infty} \prod_{j=1}^{M} \left\langle \delta(\vec{X}_j - \vec{X}_{j-1} - \vec{J}_{j-1}) \right\rangle_J. \tag{290}$$

Using the delta functions leads to the result

$$P(\{\vec{X}_t\}_{t>0}|\vec{X}_0) = \lim_{M\to\infty} \prod_{j=1}^{M} \frac{\exp\left(-\frac{1}{2\Delta t} \langle \vec{X}_j - \vec{X}_{j-1} - \vec{F}_j\Delta t, \Sigma^{-1}(\vec{X}_j - \vec{X}_{j-1} - \vec{F}_j\Delta t)\rangle \right)}{\sqrt{(2\pi)^n \det(\Sigma)}}. \tag{291}$$

This is the well-known Onsager-Machlup functional. To get the probability of the full trajectory, we need to weight this by the probability of a given initial condition

$$P(\{\vec{X}_t\}_{t\geq 0}) = P(\vec{X}_0) \lim_{M\to\infty} \prod_{j=1}^{M} \frac{\exp\left(-\frac{1}{2\Delta t} \langle \vec{X}_j - \vec{X}_{j-1} - \vec{F}_j\Delta t, \Sigma^{-1}(\vec{X}_j - \vec{X}_{j-1} - \vec{F}_j\Delta t)\rangle \right)}{\sqrt{(2\pi)^n \det(\Sigma)}}. \tag{292}$$

2. The Maximum Likelihood Estimate

For the case of an Ornstein-Uhlenbeck process, we have

$$\vec{F_j} = \mathcal{J}(\vec{X_j} - \vec{\mu}). \tag{293}$$

and the steady state distribution

$$P(\vec{X_0}) = \frac{\exp\left(-\frac{1}{2}\left\langle \vec{X_0} - \vec{\mu}, \mathcal{C}^{-1}(\vec{X_0} - \vec{\mu})\right\rangle\right)}{\sqrt{(2\pi)^n \det(\mathcal{C})}}. \tag{294}$$

We can re-write our functional as

$$\begin{aligned} P(\vec{X}_{t\geq 0}) \sim & \frac{\exp\left(-\frac{1}{2}\left\langle \vec{X_0} - \vec{\mu}, \mathcal{C}^{-1}(\vec{X_0} - \vec{\mu})\right\rangle\right)}{\sqrt{(2\pi)^n \det(\mathcal{C})}} \\ & \times \prod_{j=1}^{M} \frac{\exp\left(-\frac{1}{2\Delta t}\langle \vec{X_j} - \vec{X}_{j-1} - \vec{F_j}\Delta t, \Sigma^{-1}(\vec{X_j} - \vec{X}_{j-1} - \vec{F_j}\Delta t)\rangle\right)}{\sqrt{(2\pi)^n \det(\Sigma)}}, \end{aligned} \tag{295}$$

where we are working with the expression at finite M and then taking the $M \to \infty$ limit. Generally, the maximum likelihood estimate is computed via

$$\hat{\vec{\theta}} = \text{argmax}_{\vec{\theta}} P(\vec{x}|\vec{\theta}), \tag{296}$$

where $\vec{x}$ is the data and $\vec{\theta}$ are the parameters influencing the distribution [20]. Since the logarithm is monotone, this maximization is often computed by taking the logarithm and differentiating. This gives

$$\nabla_{\vec{\mu}} \log P \sim -\mathcal{C}^{-1}(\vec{\mu} - \vec{X_0}) - \mathcal{J}^T \Sigma^{-1} \sum_{j=1}^{M} (\vec{X_j} - \vec{X}_{j-1} + \mathcal{J}(\vec{\mu} - \vec{X}_{j-1})\Delta t). \tag{297}$$

Let's simplify this expression. The difference of X terms form a telescoping sum that simplifies to

$$\sum_{j=1}^{M} (\vec{X_j} - \vec{X}_{j-1}) = \vec{X}_\tau - \vec{X_0}, \tag{298}$$

using the fact that $M\Delta t = \tau$. The μ term from the dynamics simplifies

$$\sum_{j=1}^{M} \mathcal{J}\vec{\mu}\Delta t = \mathcal{J}\vec{\mu}\tau. \tag{299}$$

The last term from the dynamics is the definition of an Itô integral

$$-\sum_{j=1}^{M} \mathcal{J}\vec{X}_{j-1}\Delta t = -\mathcal{J}\int_0^\tau \vec{X}_t dt. \tag{300}$$

This leads to the simplified expression

$$\nabla_{\vec{\mu}} \log P = -\mathcal{C}^{-1}(\vec{\mu} - \vec{X}_0) - \mathcal{J}^T\Sigma^{-1}\left[\vec{X}_\tau - \vec{X}_0 + \mathcal{J}\vec{\mu}\tau - \mathcal{J}\int_0^\tau \vec{X}_t dt\right]. \tag{301}$$

Our maximum likelihood estimate is determined by finding the $\vec{\mu}$ that causes the gradient to vanish, and this is

$$\hat{\vec{\mu}} = \left(\mathcal{C}^{-1} + \mathcal{J}^T\Sigma^{-1}\mathcal{J}\tau\right)^{-1}\left[\left(\mathcal{C}^{-1} + \mathcal{J}^T\Sigma^{-1}\right)\vec{X}_0 - \mathcal{J}^T\Sigma^{-1}\vec{X}_\tau + \mathcal{J}^T\Sigma^{-1}\mathcal{J}\int_0^\tau \vec{X}_t dt\right]. \tag{302}$$

Note that this is an unbiased estimator, as the mean of $\vec{X}_t$ is $\vec{\mu}$ for all t for our given initial condition. Furthermore, since it is a linear combination of gaussian random variables, it is also a gaussian random variable. In the long time limit, the time average term dominates. This can be written as the uniform time average plus corrections that vanish at long times. It is straightforward, albeit tediuous, to compute the covariance matrix. After a lot of cancellation, we find

$$\mathcal{C}_{\vec{\mu},\vec{\mu}} = \left\langle (\hat{\vec{\mu}} - \vec{\mu})(\hat{\vec{\mu}} - \vec{\mu})^T \right\rangle = \left(\mathcal{C}^{-1} + \mathcal{J}^T\Sigma^{-1}\mathcal{J}\tau\right)^{-1}, \tag{303}$$

This also has the same short- and long-time asymptotics as the naive time average.

3. Cramer-Rao Bound

The Cramer-Rao bound specifies the best that an estimate can possibly do [20]. The multivariate Cramer-Rao bound states that, for an unbiased estimator,

$$\mathcal{C}_{\vec{\theta},\vec{\theta}} \geq \mathcal{I}(\vec{\theta})^{-1}, \tag{304}$$

where $\mathcal{I}(\vec{\theta})$ is the Fisher information

$$\mathcal{I}_{i,j}(\vec{\theta}) := \left\langle \left(\frac{\partial \log P(\vec{x}|\vec{\theta})}{\partial \theta_i} \right) \left(\frac{\partial \log P(\vec{x}|\vec{\theta})}{\partial \theta_j} \right) \right\rangle = - \left\langle \frac{\partial^2 \log P(\vec{x}|\vec{\theta})}{\partial \theta_i \partial \theta_j} \right\rangle, \tag{305}$$

where the last step assumes differentiability and uses integration by parts. Here $A \geq B$ means that $A - B$ is a positive semi-definite matrix. Note that any positive semi-definite matrix M has $\vec{v}^T M \vec{v} \geq 0$ for any real vector $\vec{v}$. Taking $\vec{v}$ to be any standard unit vector gives the inequality

$$\left[\mathcal{C}_{\vec{\theta},\vec{\theta}} \right]_{i,i} \geq \left[\mathcal{I}(\vec{\theta})^{-1} \right]_{i,i}. \tag{306}$$

The variances of the estimates are bounded below by the diagonal elements of the inverse Fisher matrix. When the matrix "inequality" is saturated, the variances of the estimates are minimized.

Focusing on a particular component of the mean, we have

$$\frac{\partial \log P}{\partial \mu_i} = - \sum_k \mathcal{C}^{-1}_{i,k} \mu_k - \sum_k (\mathcal{J}^T \Sigma^{-1} \mathcal{J})_{i,k} \mu_k \tau + f_i(\vec{X}), \tag{307}$$

where $f_i(\vec{X})$ contains the $\vec{\mu}$-independent terms. Taking another derivative with respect to μ_j gives

$$\frac{\partial^2 \log P}{\partial \mu_i \partial \mu_j} = -\mathcal{C}^{-1}_{i,j} - (\mathcal{J}^T \Sigma^{-1} \mathcal{J})_{i,j} \tau. \tag{308}$$

This is a constant, so it is minus the Fisher information, see Eq. 305. We see that the inverse Fisher information matrix is equal to the covariance matrix $\mathcal{C}_{\vec{\mu},\vec{\mu}}$, so maximum likelihood estimation attains the minimum possible error.

4. Comparison of Time Averaging and Maximum Likelihood

Using the expressions derived above, we can compute the relative error using the maximum likelihood approach and compare it to the time average. This is shown in Fig. S3, where the parameter values are those used in the main text, and we see that the two curves are almost identical. Although maximum likelihood is optimal, it assumes that the cell "knows" the matrices $\mathcal{J}$ and Σ, but this result shows that the cell can come very close to the fundamental limit using naive time averaging.

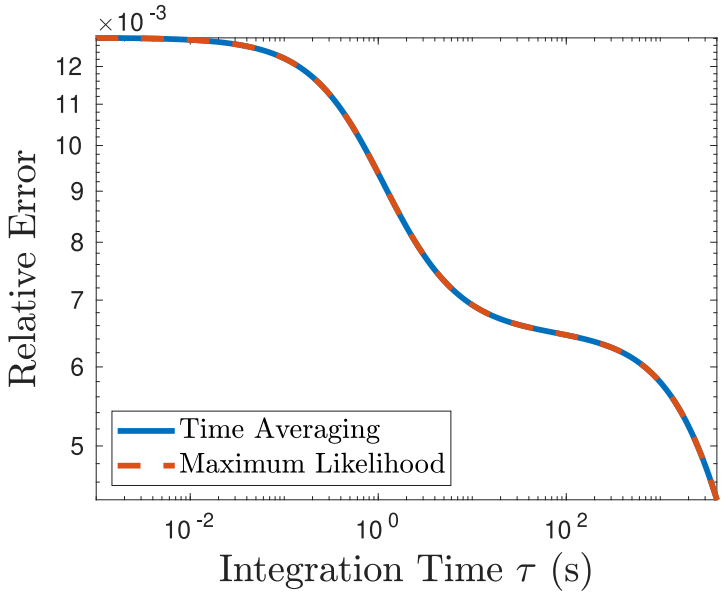

Figure 13: Comparison of the relative error in temperature sensing through maximum likelihood (red) and time averaging (blue). Parameter values match those used in the main text: $f = 1/2$, $\alpha = 6.94 \times 10^{-4}$, $k_d = 7.1 \times 10^{-4}$ s^{-1}, $k^- = 5.5 \times 10^{-4}$ s^{-1}, and $k^+/k^- = 2521$.

F. Temperature Dependence of the Production and Dilution Rates and the Feedback Strength

In the main text, we account for the temperature dependence of the binding rates k_d and k_m via the experimentally characterized monomer fraction $f(T)$. We assume that the re-

maining parameters k^+, k^-, and α are temperature independent, but in principle they could depend on temperature. Therefore, we investigate the temperature dependence of these parameters here. We will argue that dk^+/dT and $d\alpha/dT$ may neglected based on experimental evidence and that dk^-/dT as estimated from experiments is negligible quantitatively compared to df/dT.

We will begin by considering the experimental results regarding k^+ and α. Hurme et al. performed a Miller assay on mutants where the region of gene coding for TlpA was removed and replaced with a reporter, while the promoter was unchanged [56]. This assay reports the number of times that a gene has been expressed within a period of time, and it was not found to vary significantly with temperature in the mutants. Since k^+ is the production rate in the absence of autorepression (achieved here since the cells don't contain TlpA), we take this to mean that we may safely neglect its temperature dependence. This same evidence raises the possibility that the structure of the promoter does not radically change with temperature, which suggests that we may regard α as relatively insensitive to temperature. However, making a statement about α requires the dimer to be present. Hurme et al. also did further experiments without excising the coding region of the gene. The approach was to induce modifications to the TlpA binding site on the promoter similar to what would be seen upon induction to high temperature while leaving the temperature and the fraction f constant. They tested the effects of DNA supercoiling via H-NS mutants and topoisomerase I and found that supercoiling did not contribute to derepression. They also applied ethanol stress, which is known to activate heat shock genes, and found that this did not lead to derepression of *tlpA*. We take this evidence to suggest that the interaction of the promoter with a given TlpA dimer is relatively insensitive to temperature and ignore the temperature sensitivity of α.

We now consider the temperature dependence of k^-, which is set by the cell division time. Fehlhaber and Krüger measured the temperature dependence of the division time in *Salmonella enteritidis* [36]. We fit their data over the range 22-42 °C to a quadratic function using the least squares method, shown in Fig. 14. Using the fit at $T = 39$°C with $k^- = \log(2)/\tau_{1/2}$, we find $(k^-)^{-1}dk^-/dT = -\tau_{1/2}^{-1}d\tau_{1/2}/dT = -0.044$ $(°\mathrm{C})^{-1}$. To see how this sensitivity compares to that of the fraction f in determining the temperature dependence of

the monomer number $\overline{m}$, we recall the expression for $\overline{m}$ in Eq. 272. Its scaled derivative is

$$\frac{1}{\overline{m}}\frac{d\overline{m}}{dT} = \left[1 - \frac{f(1+\chi)}{2}\right]\frac{1}{f(1-f)}\frac{df}{dT} + \left[\frac{-1-\chi}{2}\right]\frac{1}{k^-}\frac{dk^-}{dT}. \tag{309}$$

where the response-like variable $\chi = \sqrt{k^-/[2(1-f)\alpha k^+ + k^-]}$ is positive and less than one.

Now we can compare the magnitudes of the terms containing the temperature sensitivity due to k^- and that due to f. In the PD model ($\alpha \to 0$) at $f = 1/2$, the term for f in Eq. 309 is 0.31 $(°\mathrm{C})^{-1}$, while the term for k^- is 0.044 $(°\mathrm{C})^{-1}$. In the PDF model, for the parameters used in the main text ($f = 1/2$, $\alpha = 6.94 \times 10^{-4}$, s^{-1}, and $k^+/k^- = 2521$), the term for f is 0.37 $(°\mathrm{C})^{-1}$, while the term for k^- is 0.035 $(°\mathrm{C})^{-1}$. In both cases, the term for f is an order of magnitude larger than that for k^-. Therefore we neglect the temperature dependence of k^-.

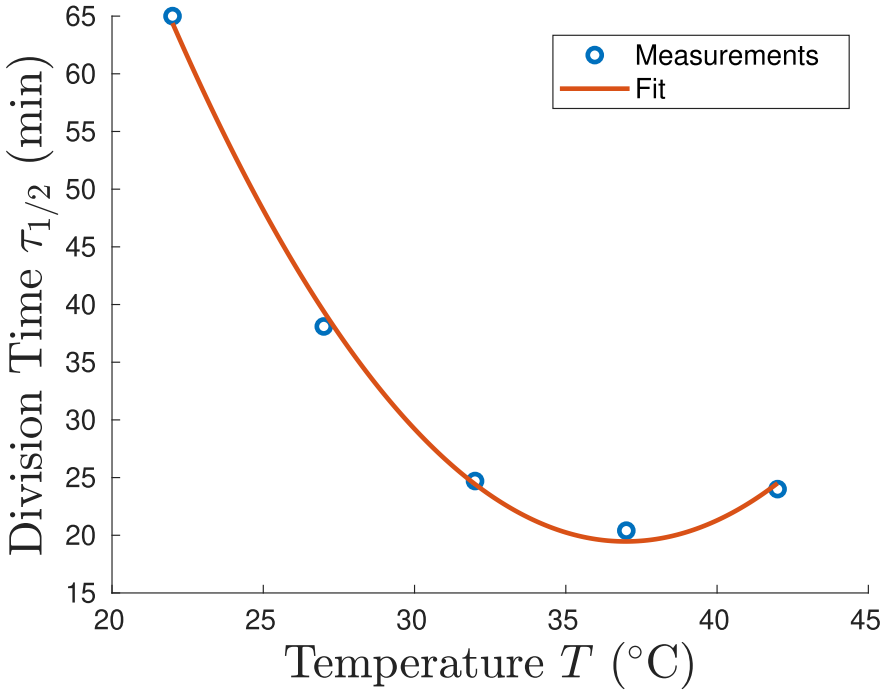

Figure 14: Plot of division time $\tau_{1/2}$ against temperature using data from Ref. [36]. The blue points are the measured average values and the red line is the quadratic fit with least square error.

G. Checking the Linear Noise Approximation Using Simulations

Employing the Gillespie algorithm [44], we check whether the linear noise approximation assumed above holds for the "Production-Dilution with Feedback" model. For the simulation, we use the parameters in the main text: $f = 1/2$, $\alpha = 6.94 \times 10^{-4}$, $k_d = 7.1 \times 10^{-4}$ s^{-1}, $k^- = 5.5 \times 10^{-4}$ s^{-1}, and $k^+/k^- = 2521$. Fig. 15 (blue) shows the distribution of monomer numbers (left) and time-averaged monomer numbers over one generation, 20 minutes (right), obtained for 10^6 simulated trajectories. Both fit well with the linear noise approximation (dashed black) which peaks around the mean $\overline{m}$ as given in Eq. 38. We have used the numerical values for this mean $\overline{m}$ and the variance as calculated using Eq. 278 and Eq. 259 respectively to generate the plots shown in the left and right panels of Fig. 15. The theoretically predicted distribution for the time-average has a larger discrepancy with the data than in the case with the instantaneous monomer number. Our theory predicts that the variances for panels A and B are 850.3 and 166.2 respectively, while the data have respective variances of 829.5 and 151.3. We see that the theory predicts a variance that is biased high in both cases. The difference between the predicted variances and the simulated variances are comparable in the two cases, but the discrepancy is relatively larger in the time-averaged case, where the variances are much smaller.

H. Timescale of Transcriptional Bursts

When the TlpA dimer is bound to the promoter region for *tlpA*, the gene is not transcribed. If the dimer is unbound, the gene is transcribed and TlpA monomers are produced at rate k^+. We introduce k_{on} and k_{off}, which are the rate constants for a single dimer molecule to bind and unbind from the promoter region respectively. It is straightforward to show that, for a given dimer number d, the steady state probability that the gene is off is $(1 + k_{\text{on}}d/k_{\text{off}})^{-1}$. For consistency with our deterministic results, we take $k_{\text{on}}/k_{\text{off}} = \alpha$. Therefore, it suffices to estimate either the binding or the unbinding rate. We will estimate the binding rate under the assumption that it is diffusion-limited. In this case, the binding

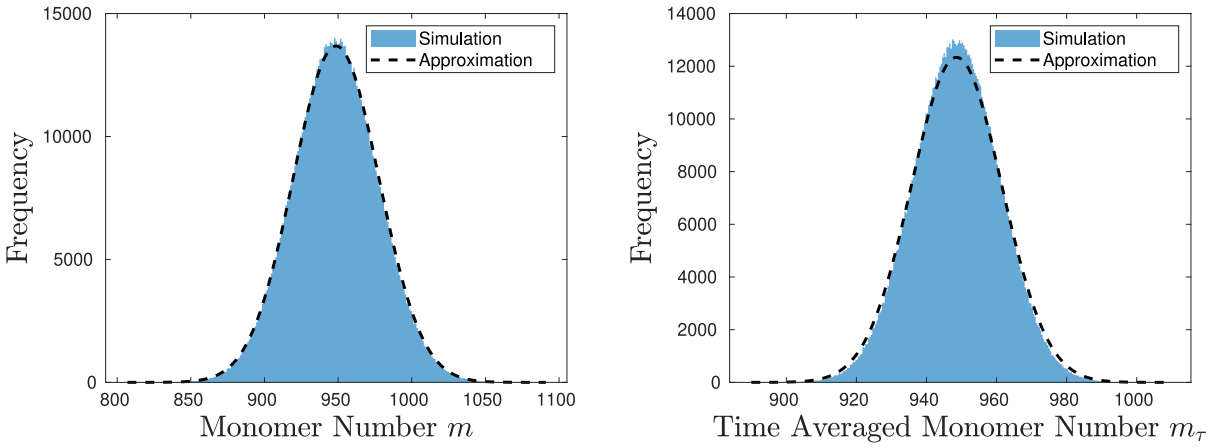

Figure 15: Illustration of the validity of the Gaussian approximation via numerical simulation. The distributions for monomer number (left) and time averaged monomer number (right) over 20 minutes were computed via Gillespie simulations (blue histograms) and the linear noise approximation (black dashed curves).

rate takes the form

$$k_{\text{on}} = \frac{4\pi DR}{V}, \tag{310}$$

where D is the relative diffusion coefficient between the promoter and a TlpA dimer, R is the contact radius at which the binding reaction occurs, and $V = 1\ \mu\text{m}^3$ is the cell volume [108].

First, we discuss estimating R. We treat the dimer as a sphere whose radius is estimated from its mass and typical values of partial specific volume for proteins [32]. The promoter can be enclosed by a sphere whose diameter is the length of the promoter. We assume that the dimer binds to the promoter when it reaches this sphere. This leads to the estimate

$$R = R_d + \frac{L}{2}, \tag{311}$$

where R_d is the estimated radius of a TlpA dimer and L is the length of the promoter.

Now we turn to estimating the relative diffusion coefficient. Since the promoter region is tethered to the rest of the DNA, we assume that its fluctuations in position are small

compared to the excursions of a given dimer molecule. This means that we may approximate the relative diffusion coefficient by the diffusion coefficient of a dimer molecule. We then use the Einstein fluctuation relation to connect the diffusion coefficient to the drag coefficient of the dimer and Stokes' law to connect the drag coefficient to its size. This leads to

$$D = \frac{k_B T}{6\pi\eta R_d}, \tag{312}$$

where η is the dynamic viscosity of cytosol.

Putting everything together, we find

$$k_{\text{on}} = \frac{2}{3}\frac{k_B T}{\eta V}\left[1 + \frac{L}{2R_d}\right]. \tag{313}$$

Koski et al. [62] state that the mass of a TlpA monomer is 43 kDa, so the dimer has a mass of 86 kDa. This leads to an estimate of $R_d \approx 2.9$ nm [32]. Typical transcription factor binding sites are typically ~ 10 base pairs long [109], and each base pair is around 0.34 nm, so this leads to $L \approx 3.4$ nm. The dynamic viscosity of cytosol may be approximated by that of water, which is 6.6×10^{-4} kg/(m $\cdot$ s) at 39 °C. This leads to the estimates $k_{\text{on}} = 6.9$ s^{-1} and $k_{\text{off}} = k_{\text{on}}/\alpha = 9.9{\times}10^3$ s^{-1}. Using the parameters in the main text ($f = 1/2$, $\alpha = 6.94{\times}10^{-4}$, $k_d = 7.1 \times 10^{-4}$ s^{-1}, $k^- = 5.5 \times 10^{-4}$ s^{-1}, and $k^+/k^- = 2521$), the typical rate of the receptor switching on is $k_{\text{on}}\overline{d} = 3.3 \times 10^3$ s^{-1}. In contrast, the dilution rate is $k^- = 5.5 \times 10^{-4}$ s^{-1}, and the dimerization rate is $2k_d\overline{m} = 1.3$ s^{-1}. There is a very clear separation of timescales here. The monomer and dimer will effectively respond to the average promoter state. Therefore, we expect the effect of promoter fluctuations on the variance of the monomer and dimer to be negligible, and this is consistent with what we have observed in simulations (data not shown).

I. Estimate of Thermosensing Precision from Miller Assay Experiments

We look at the error in temperature sensing inferred from Hurme's measurements of the Miller units at different temperatures [56]. In the Miller assay, a promoter is added after the gene of interest. Whenever the target gene is transcribed, the reporter is as well. After some time, optical measurements are taken to quantify gene activity. The result is proportional to the number of times the reporter mRNA has been translated normalized by the cell density [74, 42].

The data were taken at two different temperatures T_1 and T_2. We are interested in the activity at intermediate temperatures $T_1 < T < T_2$. Let us say that the measured values of the activity A at T_1 and T_2 are $\overline{A}_1 \pm \sigma_{A,1}$ and $\overline{A}_2 \pm \sigma_{A,2}$ respectively. We use linear interpolation to estimate the mean and standard deviation

$$\overline{A}(T) = \left(\frac{\overline{A}_2 - \overline{A}_1}{T_2 - T_1}\right)(T - T_1) + \overline{A}_1, \tag{314}$$

$$\sigma_A(T) = \left(\frac{\sigma_{A,2} - \sigma_{A,1}}{T_2 - T_1}\right)(T - T_1) + \sigma_{A,1}. \tag{315}$$

We assume that the error is given by linear error propagation. Specifically, the units are measured and Eq. 314 is inverted to solve for temperature $\hat{T} = f(A)$. Linear error propagation at the transition temperature gives the fluctuations in the temperature estimate

$$\sigma(\hat{T}) = \frac{\sigma_A(T_M)}{|d\overline{A}/dT|} = \sigma_A(T_M)\frac{|T_2 - T_1|}{|\overline{A}_2 - \overline{A}_1|}, \tag{316}$$

which leads to a relative error

$$\frac{\sigma(\hat{T})}{|T_2 - T_1|} = \frac{\sigma(\hat{T})}{\Delta T} = \frac{\sigma_A(T_M)}{|\overline{A}_2 - \overline{A}_1|}. \tag{317}$$

For *S. typhimurium* molecule A is TlpA, and the experiments were done at $T_1 = 37°C$ and $T_2 = 43°C$ and found $\overline{A}_1 = 68$, $\sigma_{A,1} = 16$, $\overline{A}_2 = 294$, $\sigma_{A,2} = 116$, $T_M = 39°C$ [56]. This leads to a relative error of 24%, as stated in the main text.

J. Including the Miller Assay Reporter in the Theory

1. Theoretical Calculation

As mentioned above, the Miller units are proportional to the number of reporter molecules produced per cell. Therefore, we add the production of a reporter molecule β to our model. This is produced whenever the monomer would be produced. Since we care about the number produced per cell per generation (around $\tau = 20$ minutes), we neglect the effect of degradation or dilution on β and start with $\beta_0 = 0$. We now compute the error in temperature sensing due to the reporter copy number.

We perform the second-order Kramers-Moyal expansion and then apply the linear noise approximation to the monomer production rate to find

$$d\beta_t = \frac{k^+}{1+\alpha d_t}dt + \sqrt{\frac{k^+}{1+\alpha d_t}}dW_t^+ \approx \left[\frac{k^+}{1+\alpha\overline{d}} - \frac{\alpha k^+ \delta d_t}{(1+\alpha\overline{d})^2}\right]dt + \sqrt{\frac{k^+}{1+\alpha\overline{d}}}dW_t^+, \quad (318)$$

where W_t^+ is a Wiener process with variance t. This can be solved by integrating

$$\beta_\tau - \frac{k^+\tau}{1+\alpha\overline{d}} = -\frac{\alpha k^+}{(1+\alpha\overline{d})^2}\int_0^\tau \delta d_{t'}dt' + \sqrt{\frac{k^+}{1+\alpha\overline{d}}}\int_0^\tau dW_{t'}^+. \quad (319)$$

Since both of the terms on the right have zero mean, we see that

$$\overline{\beta}_\tau = \frac{k^+\tau}{1+\alpha\overline{d}}. \quad (320)$$

Differentiating with respect to temperature gives

$$\left|\frac{d\overline{\beta}_\tau}{dT}\right| = \frac{\alpha k^+\tau}{(1+\alpha\overline{d})^2}\left|\frac{d\overline{d}}{dT}\right|. \quad (321)$$

We evaluate this by using Eqs. 247, 263, 272, and 309.

Now we need to solve for the fluctuations. Some care is required here, since the noise in β is coupled to the noise in the monomer. This follows from decomposing the production-degradation noise in Eq. 261 as

$$\sqrt{\frac{k^+}{1+\alpha d_t} + k^- m_t}dW_t^{(3)} = \sqrt{\frac{k^+}{1+\alpha d_t}}dW_t^+ - \sqrt{k^- m_t}dW_t^-, \quad (322)$$

where W_t^+ and W_t^- are independent Wiener processes with variance t. Squaring Eq. 319 and taking the expectation value gives

$$\begin{aligned}\sigma^2(\beta_\tau) = \frac{(\alpha k^+)^2}{(1+\alpha\overline{d})^4}\int_0^\tau \mathcal{C}_{1,1}(t_1-t_2)dt_1dt_2 + \frac{k^+}{1+\alpha\overline{d}}\int_0^\tau \left\langle dW_{t_1}^+ dW_{t_2}^+\right\rangle \\ - \frac{2\alpha(k^+)^{3/2}}{(1+\alpha\overline{d})^{5/2}}\int_0^\tau \left\langle dW_{t_1}^+ \delta d_{t_2}\right\rangle dt_2.\end{aligned} \tag{323}$$

By multiplying and dividing the first term by τ^2, it can be written in terms of time averaged covariances from Eq. 259. The second term is straightforward to evaluate from the Itô isometry [60]. Carrying both of these steps out gives

$$\sigma^2(\beta_\tau) = \frac{(\alpha k^+\tau)^2}{(1+\alpha\overline{d})^4}[\mathcal{C}_{\mathrm{TA}}(\tau)]_{1,1} + \frac{k^+\tau}{1+\alpha\overline{d}} - \frac{2\alpha(k^+)^{3/2}}{(1+\alpha\overline{d})^{5/2}}\int_0^\tau \left\langle dW_{t_1}^+ \delta d_{t_2}\right\rangle dt_2. \tag{324}$$

We can evaluate the remaining term using the analytic solution for the Ornstein-Uhlenbeck process from Eq. 250. After linearizing Eq. 261 around the steady state mean, we have $\vec{\mu} = 0$, so there are two terms in δd_t. The first is the exponential decay of the initial conditions. Since the initial conditions are uncorrelated with the stochastic driving term, this vanishes. The second term, arising from the stochasticity and damping, will make a non-vanishing contribution. It will be convenient to express the noise terms for each reaction as a vector $\vec{W}_t = (W_t^{(1)}, W_t^{(2)}, W_t^+, W_t^-)$. This can be related to $\vec{N}$ in Eq. 276 by introducing a matrix

$$\mathcal{B} = \begin{bmatrix} \sqrt{k_d\overline{m}^2 + k_m\overline{d}} & \sqrt{k^-\overline{d}} & 0 & 0 \\ -2\sqrt{k_d\overline{m}^2 + k_m\overline{d}} & 0 & \sqrt{\dfrac{k^+}{1+\alpha\overline{d}}} & -\sqrt{k^-\overline{m}} \end{bmatrix} \tag{325}$$

so that $\vec{N}_t = \mathcal{B}\vec{W}_t$. We have

$$\int_0^\tau \left\langle dW_{t_1}^+ \delta d_{t_2}\right\rangle dt_2 = \int_0^\tau \left\langle dW_{t_1}^+ dt_2 \int_0^{t_2} [e^{\mathcal{J}(t_2-t_3)}\mathcal{B}d\vec{W}_{t_3}]_1 \right\rangle. \tag{326}$$

Carrying out the matrix multiplication and using the Itô isometry again gives

$$\int_0^\tau \left\langle dW_{t_1}^+ \delta d_{t_2}\right\rangle dt_2 = \sqrt{\frac{k^+}{1+\alpha\overline{d}}}\int_0^\tau dt' \int_0^{t'} [e^{\mathcal{J}(t'-t'')}]_{1,2}dt'', \tag{327}$$

where $\mathcal{J}$ is the Jacobian from Eq. 275. Again, we perform the change of variables $(t', t'') \mapsto (\Delta, t'')$, with $\Delta = t' - t''$. Switching the order of integration, integrating over t'' first, and then performing integration by parts for Δ gives

$$\int_0^\tau \left\langle dW_{t_1}^+ \delta d_{t_2} \right\rangle dt_2 = \sqrt{\frac{k^+}{1+\alpha\overline{d}}} \left[-\tau \mathcal{J}^{-1} + \mathcal{J}^{-2} \left[e^{\mathcal{J}\tau} - \mathbb{I} \right] \right]_{1,2}. \tag{328}$$

Combining this with the previous two parts from Eq. 324 to find

$$\sigma^2(\beta_\tau) = \frac{(\alpha k^+ \tau)^2}{(1+\alpha\overline{d})^4} [\mathcal{C}_{\mathrm{TA}}(\tau)]_{1,1} + \frac{k^+\tau}{1+\alpha\overline{d}} - \frac{2\alpha(k^+)^2}{(1+\alpha\overline{d})^3} \left[-\tau \mathcal{J}^{-1} + \mathcal{J}^{-2} \left[e^{\mathcal{J}\tau} - \mathbb{I} \right] \right]_{1,2}. \tag{329}$$

The relative error for temperature sensing in this strategy is $\sigma(\beta_\tau)/(\Delta T |d\overline{\beta}_\tau/dT|)$. For the other parameters, we use the values in the main text: $f = 1/2$, $\alpha = 6.94 \times 10^{-4}$, $k_d = 7.1 \times 10^{-4}$ s^{-1}, $k^- = 5.5 \times 10^{-4}$ s^{-1}, and $k^+/k^- = 2521$. This leads to a relative error of 6.7%.

2. Including Translational Bursts

The transcripts for TlpA and the reporter could have different burst sizes, whose respective means we denote by $\overline{b}_T$ and $\overline{b}_\beta$. The terms in the deterministic rate equations take the form (propensity)×(mean change). When adding bursts to TlpA, the mean change in molecule number per reaction changes $1 \mapsto \overline{b}_T$. To preserve the mean amount of TlpA, and our consistency with experimental measurements, we map $k^+ \mapsto k^+/\overline{b}_T$. Note that this does not generally preserve the amount of β in each cell, as the mean production of β transforms as

$$\frac{k^+}{1+\alpha\overline{d}} \mapsto \frac{k^+ \overline{b}_\beta/\overline{b}_T}{1+\alpha\overline{d}}. \tag{330}$$

Intuitively, the mean burst size of β has been measured and is held fixed, but varying $\overline{b}_T$ tunes the frequency of bursts. We take $\overline{b}_\beta = 7.8$, which is the measured value for the reporter beta-galactosidase [120], and consider multiple values for the mean burst size of TlpA that are typical for bacteria: $\overline{b}_T = 1, 5, 7.8$ and 10. To find the variance in the amount of β, we use Gillespie simulations [44] where each production event produces b_T monomers and b_β reporter molecules, where b_T and b_β are independent geometric random variables with respective means $\overline{b}_T$ and $\overline{b}_\beta$. The derivative is computed using the deterministic result of the

previous section, but caution must be exercised when modifying k^+, since $\overline{d}$ does not change with the $\bar{b}_T$, but $\overline{\beta}_\tau$ does. Modifying Eq. 321, the result is

$$\left|\frac{d\overline{\beta}_\tau}{dT}\right| = \frac{\alpha k^+ \tau(\bar{b}_\beta/\bar{b}_T)}{(1+\alpha\overline{d})^2}\left|\frac{d\overline{d}}{dT}\right|, \tag{331}$$

where $\overline{d}$ is computed according to Eqs. 263 and 272 without changing or mapping k^+, as the mapping leaves the production term in $\dot{\overline{m}}$ unchanged. We use the values in the main text: $f = 1/2$, $\alpha = 6.94 \times 10^{-4}$, $k_d = 7.1 \times 10^{-4}$ s^{-1}, $k^- = 5.5 \times 10^{-4}$ s^{-1}, and $k^+/k^- = 2521$. We found that the relative error increased with $\bar{b}_T$, as the mean $\overline{\beta}_\tau$ decreased. Over the physiologically relevant range of $5 \leq \bar{b}_T \leq 10$, we found that the relative error increased from 23% to 32%. Because the range $5 \leq \bar{b}_T \leq 10$ is approximate, we round this error range to one significant digit, 20% to 30%, as stated in the main text.

Bibliography

[1] A. Acrivos and T. D. Taylor. Heat and Mass Transfer from Single Spheres in Stokes Flow. *Physics of Fluids*, 5(4):387–394, 1962.

[2] Uri Alon. *An Introduction to Systems Biology: Design Principles of Biological Circuits*. CRC Press, 2006.

[3] B. Barman. Flow of a Newtonian fluid past an impervious sphere embedded in a porous medium. *Indian Journal of Pure & Applied Mathematics*, 27(12):1249–1256, 1996.

[4] Carl M. Bender and Steven A. Orszag. *Advanced Mathematical Methods for Scientists and Engineers I: Asymptotic Methods and Perturbation Theory*. Springer Science & Business Media, 1999.

[5] Alexander M. Berezhkovskii and Attila Szabo. Effect of ligand diffusion on occupancy fluctuations of cell-surface receptors. *Journal of Chemical Physics*, 139(12):121910, 2013.

[6] Howard C. Berg and Edward M. Purcell. Physics of Chemoreception. *Biophysical Journal*, 20(2):193–219, 1977.

[7] James O. Berger. *Statistical Decision Theory and Bayesian Analysis*. Springer Science & Business Media, 1985.

[8] Farzan Beroz, Louise M. Jawerth, Stefan Muenster, David A. Weitz, Chase P. Broedersz, and Ned S. Wingreen. Physical limits to biomechanical sensing in disordered fibre networks. *Nature Communications*, 8:16096, 2017.

[9] W. Bialek and S. Setayeshgar. Physical limits to biochemical signaling. *Proceedings of the National Academy of Sciences of the United States of America*, 102(29):10040–10045, 2005.

[10] Brendan A. Bicknell, Peter Dayan, and Geoffrey J. Goodhill. The limits of chemosensation vary across dimensions. *Nature Communications*, 6:7468, 2015.

[11] Indrani Bose and Sayantari Ghosh. Bifurcation and criticality. *Journal of Statistical Mechanics-Theory and Experiment*, page 043403, 2019.

[12] Me Brachet and E. Tirapegui. On the Critical-Behavior of the Schlogl Model. *Physics Letters A*, 81(4):211–214, 1981.

[13] H. C. Brinkman. A calculation of the viscous force exerted by a flowing fluid on a dense swarm of particles. *Flow, Turbulence and Combustion*, 1(1):27, 1949.

[14] Melissa A. Byers, Psachal A. Calloway, Laurie Shannon, Heather D. Cunningham, Sarah Smith, Fang Li, Brian C. Fassold, and Charlotte M. Vines. Arrestin 3 mediates endocytosis of CCR7 following ligation of CCL19 but not CCL21. *Journal of Immunology*, 181(7):4723–4732, 2008.

[15] Tommy A. Byrd, Amir Erez, Robert M. Vogel, Curtis Peterson, Michael Vennettilli, Gregoire Altan-Bonnet, and Andrew Mugler. Critical slowing down in biochemical networks with feedback. *Physical Review E*, 100(2):022415, 2019.

[16] Martin Carballo-Pacheco, Jonathan Desponds, Tatyana Gavrilchenko, Andreas Mayer, Roshan Prizak, Gautam Reddy, Ilya Nemenman, and Thierry Mora. Receptor crosstalk improves concentration sensing of multiple ligands. *Physical Review E*, 99(2):022423, 2019.

[17] H. M. Chao, D. L. Bautista, J. Litowski, R. T. Irvin, and R. S. Hodges. Use of a heterodimeric coiled-coil system for biosensor application and affinity purification. *Journal of Chromatography B-Analytical Technologies in the Biomedical and Life Sciences*, 715(1):307–329, 1998.

[18] S. R. Chary and R. K. Jain. Direct Measurement of Interstitial Convection and Diffusion of Albumin in Normal and Neoplastic Tissues by Fluorescence Photobleaching. *Proceedings of the National Academy of Sciences of the United States of America*, 86(14):5385–5389, 1989.

[19] Jesse W. Cotari, Guillaume Voisinne, Orly Even Dar, Volkan Karabacak, and Gregoire Altan-Bonnet. Cell-to-Cell Variability Analysis Dissects the Plasticity of Signaling of Common gamma Chain Cytokines in T Cells. *Science Signaling*, 6(266):ra17, 2013.

[20] Thomas M. Cover and Joy A. Thomas. *Elements of Information Theory*. John Wiley & Sons, 2012.

[21] H. Dafni, T. Israely, Z. M. Bhujwalla, L. E. Benjamin, and M. Neeman. Overexpression of vascular endothelial growth factor 165 drives peritumor interstitial convection and induces lymphatic drain: Magnetic resonance imaging, confocal microscopy, and histological tracking of triple-labeled albumin. *Cancer Research*, 62(22):6731–6739, 2002.

[22] Jonathan Desponds, Massimo Vergassola, and Aleksandra M Walczak. A mechanism for hunchback promoters to readout morphogenetic positional information in less than a minute. *eLife*, 9:e49758, 2020.

[23] Wolfgang Driever and Christiane Nüsslein-Volhard. The bicoid protein is a positive regulator of hunchback transcription in the early Drosophila embryo. *Nature*, 337(6203):138–143, 1989.

[24] David B. Dusenbery. Limits of Thermal Sensation. *Journal of Theoretical Biology*, 131(3):263–271, 1988.

[25] David Ellison, Andrew Mugler, Matthew D. Brennan, Sung Hoon Lee, Robert J. Huebner, Eliah R. Shamir, Laura A. Woo, Joseph Kim, Patrick Amar, Ilya Nemenman, Andrew J. Ewald, and Andre Levchenko. Cell-cell communication enhances the capacity of cell ensembles to sense shallow gradients during morphogenesis. *Proceedings of the National Academy of Sciences of the United States of America*, 113(6):E679–E688, 2016.

[26] Robert G. Endres and Ned S. Wingreen. Accuracy of direct gradient sensing by single cells. *Proceedings of the National Academy of Sciences of the United States of America*, 105(41):15749–15754, 2008.

[27] Robert G. Endres and Ned S. Wingreen. Accuracy of direct gradient sensing by cell-surface receptors. *Progress in Biophysics & Molecular Biology*, 100(1-3):33–39, 2009.

[28] Robert G. Endres and Ned S. Wingreen. Maximum Likelihood and the Single Receptor. *Physical Review Letters*, 103(15):158101, 2009.

[29] Thorsten Erdmann, Martin Howard, and Pieter Rein ten Wolde. Role of Spatial Averaging in the Precision of Gene Expression Patterns. *Physical Review Letters*, 103(25):258101, 2009.

[30] Amir Erez, Tommy A. Byrd, Michael Vennettilli, and Andrew Mugler. Cell-to-Cell Information at a Feedback-Induced Bifurcation Point. *Physical Review Letters*, 125(4):048103, 2020.

[31] Amir Erez, Tommy A. Byrd, Robert M. Vogel, Gregoire Altan-Bonnet, and Andrew Mugler. Universality of biochemical feedback and its application to immune cells. *Physical Review E*, 99(2):022422, 2019.

[32] Harold P. Erickson. Size and Shape of Protein Molecules at the Nanometer Level Determined by Sedimentation, Gel Filtration, and Electron Microscopy. *Biological Procedures Online*, 11(1):32–51, 2009.

[33] M. Falconi, B. Colonna, G. Prosseda, G. Micheli, and C. O. Gualerzi. Thermoregulation of Shigella and Escherichia coli EIEC pathogenicity. A temperature-dependent structural transition of DNA modulates accessibility of virF promoter to transcriptional repressor H-NS. *Embo Journal*, 17(23):7033–7043, 1998.

[34] Sean Fancher and Andrew Mugler. Fundamental Limits to Collective Concentration Sensing in Cell Populations. *Physical Review Letters*, 118(7):078101, 2017.

[35] Sean Fancher, Michael Vennettilli, Nicholas Hilgert, and Andrew Mugler. Precision of Flow Sensing by Self-Communicating Cells. *Physical Review Letters*, 124(16):168101, 2020.

[36] K. Fehlhaber and G. Kruger. The study of Salmonella enteritidis growth kinetics using rapid automated bacterial impedance technique. *Journal of Applied Microbiology*, 84(6):945–949, 1998.

[37] Mark E. Fleury, Kendrick C. Boardman, and Melody A. Swartz. Autologous morphogen gradients by subtle interstitial flow and matrix interactions. *Biophysical Journal*, 91(1):113–121, 2006.

[38] Robert Foreman and Roy Wollman. Mammalian gene expression variability is explained by underlying cell state. *Molecular Systems Biology*, 16(2):e9146, 2020.

[39] R. F. Fox. Gaussian Stochastic-Processes in Physics. *Physics Reports-Review Section of Physics Letters*, 48(3):179–283, 1978.

[40] Theodore Frankel. *The Geometry of Physics: An Introduction*. Cambridge University Press, 2011.

[41] Nir Friedman, Long Cai, and X. Sunney Xie. Linking stochastic dynamics to population distribution: An analytical framework of gene expression. *Physical Review Letters*, 97(16):168302, 2006.

[42] Hernan G. Garcia, Heun Jin Lee, James Q. Boedicker, and Rob Phillips. Comparison and Calibration of Different Reporters for Quantitative Analysis of Gene Expression. *Biophysical Journal*, 101(3):535–544, 2011.

[43] Crispin Gardiner. *Stochastic Methods: A Handbook for the Natural and Social Sciences*. Springer Berlin Heidelberg, 2009.

[44] D. T. Gillespie. Exact Stochastic Simulation of Coupled Chemical-Reactions. *Journal of Physical Chemistry*, 81(25):2340–2361, 1977.

[45] Nigel Goldenfeld. *Lectures On Phase Transitions And The Renormalization Group*. CRC Press, 2018.

[46] P. Grassberger. Monte-Carlo Simulations for Schlogls 2nd Model. *Physics Letters A*, 84(9):459–461, 1981.

[47] P. Grassberger. On Phase-Transitions in Schlogl 2nd Model. *Zeitschrift Fur Physik B-Condensed Matter*, 47(4):365–374, 1982.

[48] Thomas Gregor, David W. Tank, Eric F. Wieschaus, and William Bialek. Probing the limits to positional information. *Cell*, 130(1):153–164, 2007.

[49] C. L. E. Helm, M. E. Fleury, A. H. Zisch, F. Boschetti, and M. A. Swartz. Synergy between interstitial flow and VEGF directs capillary morphogenesis in vitro through a gradient amplification mechanism. *Proceedings of the National Academy of Sciences of the United States of America*, 102(44):15779–15784, 2005.

[50] Maarten P. Heyn and Wolfgang O. Weischet. Circular dichroism and fluorescence studies on the binding of ligands to the α subunit of tryptophan synthase. *Biochemistry*, 14(13):2962–2968, 1975.

[51] Peter V. Hornbeck, Bin Zhang, Beth Murray, Jon M. Kornhauser, Vaughan Latham, and Elzbieta Skrzypek. PhosphoSitePlus, 2014: mutations, PTMs and recalibrations. *Nucleic Acids Research*, 43(D1):D512–D520, 2015.

[52] W. Horsthemke and R. Lefever. *Noise-Induced Transitions: Theory and Applications in Physics, Chemistry, and Biology*. Springer, 1984.

[53] Bo Hu, Wen Chen, Wouter-Jan Rappel, and Herbert Levine. Physical Limits on Cellular Sensing of Spatial Gradients. *Physical Review Letters*, 105(4):048104, 2010.

[54] A. J. Hudspeth, Frank Juelicher, and Pascal Martin. A Critique of the Critical Cochlea: Hopf-a Bifurcation-Is Better Than None. *Journal of Neurophysiology*, 104(3):1219–1229, 2010.

[55] R. Hurme, K. D. Berndt, E. Namork, and M. Rhen. DNA binding exerted by a bacterial gene regulator with an extensive coiled-coil domain. *Journal of Biological Chemistry*, 271(21):12626–12631, 1996.

[56] R. Hurme, K. D. Berndt, S. J. Normark, and M. Rhen. A proteinaceous gene regulatory thermometer in Salmonella. *Cell*, 90(1):55–64, 1997.

[57] Lili Jiang, Qi Ouyang, and Yuhai Tu. A Mechanism for Precision-Sensing via a Gradient-Sensing Pathway: A Model of Escherichia coli Thermotaxis. *Biophysical Journal*, 97(1):74–82, 2009.

[58] Kazunari Kaizu, Wiet de Ronde, Joris Paijmans, Koichi Takahashi, Filipe Tostevin, and Pieter Rein ten Wolde. The Berg-Purcell Limit Revisited. *Biophysical Journal*, 106(4):976–985, 2014.

[59] N. G. Van Kampen. *Stochastic Processes in Physics and Chemistry*. Elsevier, 2011.

[60] Fima C. Klebaner. *Introduction to Stochastic Calculus with Applications*. Imperial College Press, 2012.

[61] Birgit Klinkert and Franz Narberhaus. Microbial thermosensors. *Cellular and Molecular Life Sciences*, 66(16):2661–2676, 2009.

[62] P. Koski, H. Saarilahti, S. Sukupolvi, S. Taira, P. Riikonen, K. Osterlund, R. Hurme, and M. Rhen. A New Alpha-Helical Coiled Coil Protein Encoded by the Salmonella-Typhimurium Virulence Plasmid. *Journal of Biological Chemistry*, 267(17):12258–12265, 1992.

[63] Dmitry Krotov, Julien O. Dubuis, Thomas Gregor, and William Bialek. Morphogenesis at criticality. *Proceedings of the National Academy of Sciences of the United States of America*, 111(10):3683–3688, 2014.

[64] Alex H. Lang, Charles K. Fisher, Thierry Mora, and Pankaj Mehta. Thermodynamics of Statistical Inference by Cells. *Physical Review Letters*, 113(14):148103, 2014.

[65] Joseph W. Larkin, Xiaoling Zhai, Kaito Kikuchi, Samuel E. Redford, Arthur Prindle, Jintao Liu, Sacha Greenfield, Aleksandra M. Walczak, Jordi Garcia-Ojalvo, Andrew Mugler, and Gürol M. Süel. Signal Percolation within a Bacterial Community. *Cell Systems*, 7(2):137–145.e3, 2018.

[66] S. Lee, S. M. Jilani, G. V. Nikolova, D. Carpizo, and M. L. Iruela-Arispe. Processing of VEGF-A by matrix metalloproteinases regulates bioavailability and vascular patterning in tumors. *Journal of Cell Biology*, 169(4):681–691, 2005.

[67] Francisco J. P. Lopes, Fernando M. C. Vieira, David M. Holloway, Paulo M. Bisch, and Alexander V. Spirov. Spatial Bistability Generates hunchback Expression Sharpness in the Drosophila Embryo. *Plos Computational Biology*, 4(9):e1000184, 2008.

[68] D. B. Lowrie, V. R. Aber, and M. E. W.YR 1979 Carrol. Division and Death Rates of Salmonella typhimurium Inside Macrophages: Use of Penicillin as a Probe. *Microbiology*, 110(2):409–419, 1979.

[69] K. Maeda, Y. Imae, Ji Shioi, and F. Oosawa. Effect of Temperature on Motility and Chemotaxis of Escherichia-Coli. *Journal of Bacteriology*, 127(3):1039–1046, 1976.

[70] Pierre Mandin and Jorgen Johansson. Feeling the heat at the millennium: Thermosensors playing with fire. *Molecular Microbiology*, 113(3):588–592, 2020.

[71] J. S. McCarty and G. C. Walker. Dnak as a Thermometer - Threonine-199 Is Site of Autophosphorylation and Is Critical for Atpase Activity. *Proceedings of the National Academy of Sciences of the United States of America*, 88(21):9513–9517, 1991.

[72] Matthijs Meijers, Sosuke Ito, and Pieter Rein ten Wolde. Behavior of information flow near criticality. *Physical Review E*, 103(1):L010102, 2021.

[73] Leenoy Meshulam, Jeffrey L. Gauthier, Carlos D. Brody, David W. Tank, and William Bialek. Coarse Graining, Fixed Points, and Scaling in a Large Population of Neurons. *Physical Review Letters*, 123(17):178103, 2019.

[74] Jeffrey H. Miller and Jeffrey B. Miller. *Experiments in Molecular Genetics*. Cold Spring Harbor Laboratory, 1972.

[75] Ron Milo and Rob Phillips. *Cell Biology by the Numbers*. Garland Science, 2016.

[76] Thierry Mora. Physical Limit to Concentration Sensing Amid Spurious Ligands. *Physical Review Letters*, 115(3):038102, 2015.

[77] Thierry Mora and William Bialek. Are Biological Systems Poised at Criticality? *Journal of Statistical Physics*, 144(2):268–302, 2011.

[78] Thierry Mora and Ilya Nemenman. Physical Limit to Concentration Sensing in a Changing Environment. *Physical Review Letters*, 123(19):198101, 2019.

[79] Thierry Mora and Ned S. Wingreen. Limits of Sensing Temporal Concentration Changes by Single Cells. *Physical Review Letters*, 104(24):248101, 2010.

[80] Mia C. Morrell, Audrey J. Sederberg, and Ilya Nemenman. Latent Dynamical Variables Produce Signatures of Spatiotemporal Criticality in Large Biological Systems. *Physical Review Letters*, 126(11):118302, 2021.

[81] Andrew Mugler, Andre Levchenko, and Ilya Nemenman. Limits to the precision of gradient sensing with spatial communication and temporal integration. *Proceedings of the National Academy of Sciences of the United States of America*, 113(6):E689–E695, 2016.

[82] Andrew Mugler, Aleksandra M. Walczak, and Chris H. Wiggins. Spectral solutions to stochastic models of gene expression with bursts and regulation. *Physical Review E*, 80(4):041921, 2009.

[83] T. Munakata and M. Kamiyabu. Stochastic resonance in the FitzHugh-Nagumo model from a dynamic mutual information point of view. *European Physical Journal B*, 53(2):239–243, 2006.

[84] Jennifer M. Munson, Ravi V. Bellamkonda, and Melody A. Swartz. Interstitial Flow in a 3D Microenvironment Increases Glioma Invasion by a CXCR4-Dependent Mechanism. *Cancer Research*, 73(5):1536–1546, 2013.

[85] Miguel A. Muñoz. Colloquium: Criticality and dynamical scaling in living systems. *Reviews of Modern Physics*, 90(3):031001, 2018.

[86] S. D. Nathanson. Insights into the mechanisms of lymph node metastasis. *Cancer*, 98(2):413–423, 2003.

[87] Vudtiwat Ngampruetikorn, David J. Schwab, and Greg J. Stephens. Energy consumption and cooperation for optimal sensing. *Nature Communications*, 11(1):975, 2020.

[88] V. O'Brien. Eggs and other deformed spheroids in stokes flow. *APL Technical Digest*, 4:11–16, 1965.

[89] D. D. Patel, W. Koopmann, T. Imai, L. P. Whichard, O. Yoshie, and M. S. Krangel. Chemokines have diverse abilities to form solid phase gradients. *Clinical Immunology*, 99(1):43–52, 2001.

[90] Anja Paulick, Vladimir Jakovljevic, SiMing Zhang, Michael Erickstad, Alex Groisman, Yigal Meir, William Ryu, Ned S. Wingreen, and Victor Sourjik. Mechanism of bidirectional thermotaxis in Escherichia coli. *Elife*, 6:e26607, 2017.

[91] Goran Peskir and Albert Shiryaev. *Optimal Stopping and Free-Boundary Problems*. Springer Verlag Ny, 2006.

[92] Dan I. Piraner, Mohamad H. Abedi, Brittany A. Moser, Audrey Lee-Gosselin, and Mikhail G. Shapiro. Tunable thermal bioswitches for in vivo control of microbial therapeutics. *Nature Chemical Biology*, 13(1):75–80, 2017.

[93] Dan I. Piraner, Yan Wu, and Mikhail G. Shapiro. Modular Thermal Control of Protein Dimerization. *Acs Synthetic Biology*, 8(10):2256–2262, 2019.

[94] William J. Polacheck, Joseph L. Charest, and Roger D. Kamm. Interstitial flow influences direction of tumor cell migration through competing mechanisms. *Proceedings of the National Academy of Sciences of the United States of America*, 108(27):11115–11120, 2011.

[95] Arjun Raj and Alexander van Oudenaarden. Nature, Nurture, or Chance: Stochastic Gene Expression and Its Consequences. *Cell*, 135(2):216–226, 2008.

[96] Edward Roob, Nicola Trendel, Pieter Rein ten Wolde, and Andrew Mugler. Cooperative Clustering Digitizes Biochemical Signaling and Enhances its Fidelity. *Biophysical Journal*, 110(7):1661–1669, 2016.

[97] A. Sahni, M. Guo, S. K. Sahni, and C. W. Francis. Interleukin-1 beta but not IL-1 alpha at binds to fibrinogen and fibrin and has enhanced activity in the bound form. *Blood*, 104(2):409–414, 2004.

[98] A. Sahni, T. Odrljin, and C. W. Francis. Binding of basic fibroblast growth factor to fibrinogen and fibrin. *Journal of Biological Chemistry*, 273(13):7554–7559, 1998.

[99] F. Schlogl. Chemical Reaction Models for Nonequilibrium Phase-Transitions. *Zeitschrift Fur Physik*, 253(2):147–161, 1972.

[100] Wolfgang Schumann. Thermosensors in eubacteria: role and evolution. *Journal of Biosciences*, 32(3):549–557, 2007.

[101] P. Servant, C. Grandvalet, and P. Mazodier. The RheA repressor is the thermosensor of the HSP18 heat shock response in Streptomyces albus. *Proceedings of the National Academy of Sciences of the United States of America*, 97(7):3538–3543, 2000.

[102] Vahid Shahrezaei, Julien F. Ollivier, and Peter S. Swain. Colored extrinsic fluctuations and stochastic gene expression. *Molecular Systems Biology*, 4:196, 2008.

[103] Claude E. Shannon. A Mathematical Theory of Communication. *Bell System Technical Journal*, 27(3):379–423, 1948.

[104] Adrian C. Shieh, Hallie A. Rozansky, Boris Hinz, and Melody A. Swartz. Tumor Cell Invasion Is Promoted by Interstitial Flow-Induced Matrix Priming by Stromal Fibroblasts. *Cancer Research*, 71(3):790–800, 2011.

[105] Jacqueline D. Shields, Mark E. Fleury, Carolyn Yong, Alice A. Tomei, Gwendalyn J. Randolph, and Melody A. Swartz. Autologous chemotaxis as a mechanism of tumor cell homing to lymphatics via interstitial flow and autocrine CCR7 signaling. *Cancer Cell*, 11(6):526–538, 2007.

[106] Eric D. Siggia and Massimo Vergassola. Decisions on the fly in cellular sensory systems. *Proceedings of the National Academy of Sciences of the United States of America*, 110(39):E3704–E3712, 2013.

[107] Monica Skoge, Yigal Meir, and Ned S. Wingreen. Dynamics of Cooperativity in Chemical Sensing among Cell-Surface Receptors. *Physical Review Letters*, 107(17):178101, 2011.

[108] J. Smit, Y. Kamio, and H. Nikaido. Outer Membrane of Salmonella-Typhimurium - Chemical-Analysis and Freeze-Fracture Studies with Lipopolysaccharide Mutants. *Journal of Bacteriology*, 124(2):942–958, 1975.

[109] Alexander J. Stewart and Joshua B. Plotkin. Why Transcription Factor Binding Sites Are Ten Nucleotides Long. *Genetics*, 192(3):973–+, 2012.

[110] Ruedi Stoop and Florian Gomez. Auditory Power-Law Activation Avalanches Exhibit a Fundamental Computational Ground State. *Physical Review Letters*, 117(3):038102, 2016.

[111] Steven H. Strogatz. *Nonlinear Dynamics and Chaos: With Applications to Physics, Biology, Chemistry, and Engineering*. Avalon Publishing, 2014.

[112] Filipe Tostevin and Pieter Rein ten Wolde. Mutual Information between Input and Output Trajectories of Biochemical Networks. *Physical Review Letters*, 102(21):218101, 2009.

[113] J. Treisman and C. Desplan. The Products of the Drosophila Gap Genes Hunchback and Kruppel Bind to the Hunchback Promoters. *Nature*, 341(6240):335–337, 1989.

[114] Julien Varennes, Sean Fancher, Bumsoo Han, and Andrew Mugler. Emergent versus Individual-Based Multicellular Chemotaxis. *Physical Review Letters*, 119(18):188101, 2017.

[115] Michael Vennettilli, Amir Erez, and Andrew Mugler. Multicellular sensing at a feedback-induced critical point. *Physical Review E*, 102(5):052411, 2020.

[116] Michael Vennettilli, Soutick Saha, Ushasi Roy, and Andrew Mugler. Precision of protein thermometry. *arXiv:2012.02918v2 [physics]*, 2020.

[117] Jahn O. Waldeland and Steinar Evje. A multiphase model for exploring tumor cell migration driven by autologous chemotaxis. *Chemical Engineering Science*, 191:268–287, 2018.

[118] Kai Wang, Wouter-Jan Rappel, Rex Kerr, and Herbert Levine. Quantifying noise levels of intercellular signals. *Physical Review E*, 75(6):061905, 2007.

[119] Joshua W. Williams, Xiaohui Cui, Andre Levchenko, and Ann M. Stevens. Robust and sensitive control of a quorum-sensing circuit by two interlocked feedback loops. *Molecular Systems Biology*, 4:234, 2008.

[120] X. Sunney Xie, Paul J. Choi, Gene-Wei Li, Nam Ki Lee, and Giuseppe Lia. Single-molecule approach to molecular biology in living bacterial cells. *Annual Review of Biophysics*, 37:417–444, 2008.

[121] Yunxin Zhang, Hao Ge, and Hong Qian. van't Hoff-Arrhenius Analysis of Mesoscopic and Macroscopic Dynamics of Simple Biochemical Systems: Stochastic vs. Nonlinear Bistabilities. *arXiv:1011.2554 [physics]*, 2010.